Eddy Current Detection of Fatigue Cracks in Drill Pipes

Matthew Robert Molteno

Dissertation presented in partial fulfilment of the requirements for the degree of Master of Science in the Department of Mechanical Engineering, University of Cape Town

March 2012

PLAGIARISM DECLARATION

I hereby

1. grant the University free license to reproduce the above thesis in whole or in part, for the purpose of research;

2. declare that:

   (a) the above thesis is my own unaided work, both in conception and execution, and that apart from the normal guidance of my supervisor, I have received no assistance apart from that stated below;

   (b) except as stated below, neither the substance nor any part of the thesis has been submitted in the past, is being, or will be submitted for a degree at this or any other University.

   (c) I am now presenting the thesis for examination for the Degree of MSc.

Word count: 40568

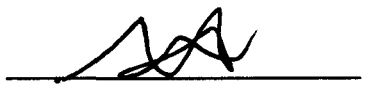

Matthew Robert Molteno

09/03/2012

Date

ABSTRACT

The Vertical Marine Mining technique is a lucrative method used by De Beers to recover bottom lying diamonds from the seabed, mainly off the coast of Namibia. The method employs a 200m length pipe-drilling structure rotated from the surface and acting as a conduit through which the disturbed sediment is transported to the surface for processing. However, cyclic operating stresses combined with corrosion have tended to cause circumferential fatigue cracks to develop on the outside surface of the drill pipe and propagate inwards. As no early warning system exists, these cracks propagate undetected until failure occurs. High operational costs and losses associated with down time, provide a strong motivation for a system to detect fatigue cracking prior to failure, especially given that fatigue crack growth rate and fatigue lifetimes can be estimated using Fracture Mechanics principles. Therefore what is required is an early warning of fatigue crack initiation with non-destructive testing (NDT).

The eddy current method is an ideal NDT technique as it does not require contact with the test surface and is highly sensitive to fatigue cracks. However, this method is generally only sensitive to surface and near surface defects. This proves to be a major limitation - the external drill pipe surface is obstructed by flanges and fittings such that continuous inspection of the external surface would be impossible. Therefore two specialised eddy current methods to allow the detection of external fatigue cracks from inside the drill pipe were reviewed, namely: Pulsed Eddy Current (PEC) and Remote Field Eddy Current (RFEC). It was found that unlike PEC, RFEC is highly sensitive to external circumferential planar defects in ferrous pipes. This, above all, highlighted the suitability of RFEC for drill pipe inspection.

An RFEC probe and pull-rig were built and - as true fatigue cracks are difficult to generate - tested on representative 0.3mm width circumferential saw-cuts machined into 81mm internal diameter, 4mm wall thickness ferrous pipe.

In a pilot study to emulate fatigue cracking, saw-cuts were incrementally 'grown' from the outside of the test pipe inwards. Initially, the probe achieved detection at close to 50% wall thickness (2mm depth). However, significant component of the signal was associated with microstructural variations in the pipe material. As this was shown to be highly repeatable, 'background' signal subtraction could be implemented by pre-recording

RFEC signals from defect free pipe (the true background signal). This improved defect detectability from depths of 50% to 15% of the wall thickness, i.e. the smallest defect detectable was a depth of 0.6mm.

From the viewpoint of drill pipe inspection, it was important to test the accuracy with which subsequent crack propagation could be monitored. This required calibration of the RFEC probe. As calibration requires monotonic parameters, it was firstly shown that defect signals were monotonic functions both of inter and intra defect depth and of a highly repeatable shape. Defect depth data was fitted to a polynomial calibration function that was able to monitor defect depth to within 5% wall thickness. As a step-like increase in defect signals was noted from through thickness defects, closer monitoring is expected to be achievable after penetration. This is relevant as drill pipes are known to remain intact for at least two weeks after cracks have fully penetrated the wall thickness.

RFEC literature showed that low volume defects tend to offer poor detectability. This suggests that fatigue cracks (which are close to zero width) should be difficult to detect. As zero-width defects cannot be machined, circumferential fatigue cracks were simulated to test this premise. The defect width - represented by the axial separation of two rectangular external metal bars - could then be adjusted and, more importantly, brought to "zero" (i.e. a fatigue crack). The results showed that circumferentially oriented, zero-width, planar defect signals were 100% separable from background signals. These results were validated by comparison of simulated defect signals with embedded defect signals.

Final Fracture Mechanics evaluation based on these results estimated that a version of the current system scaled to inspect drill pipes would be capable of detecting actual fatigue cracks from between three and seven weeks prior to fast fracture of the drill string. Therefore the probe built in this project showed great potential for detecting and monitoring fatigue cracks.

ACKNOWLEDGMENTS

The author would like to express his sincere appreciation to his supervisors: Professor R.B. Tait, Associate Professor A.J. Wilkinson and Dr T.H. Becker at the University of Cape Town for their continual guidance and assistance with this project. For each individually:

- Professor Robert Tait, a special thanks for orchestrating the project and his unerring support and excellent advice throughout its development;
- Associate Professor Andrew Wilkinson, sincere gratitude for his close attention to the electrical aspects of the project and his comprehensive approach to the electrical implementation and instrumentation;
- Dr Thorsten Becker, sincere appreciation for his dedication, availability and support, particularly for his assistance in co-ordinating the electrical and mechanical aspects of this research.

In addition, the author would like to thank the people involved for facilitating this MSc at the University of Cape Town. Special acknowledgement to: Professor J. Gryzagoridis and Armscor for financial support during the project which is gratefully acknowledged, Professor Rob Knutson for the use of the UCT materials engineering laboratory, Glen Newins for manufacturing the various pipe fittings and probe structure, Chris Wozniak for providing various heavy current circuit components, and Tracy Booysen for her technical assistance with data acquisition.

The author would also like to express sincere appreciation to close friends, too numerous to mention, for their support and understanding during this research; in particular, Craig Knowles for the support, humour, and somewhat turbulent introduction to caffeine.

Finally, I would like to express my sincere gratitude for the encouragement and support of my parents, Jane and Martin, to whom I wish to dedicate this work.

TABLE OF CONTENTS

Page

PLAGIARISM DECLARATION i
ABSTRACT iii
ACKNOWLEDGMENTS v
TABLE OF CONTENTS vii
LIST OF FIGURES xi
LIST OF TABLES xiv
LIST OF ABBREVIATIONS AND SYMBOLS xv

CHAPTER 1 INTRODUCTION 1

1.1 Background on Diamond Mining 1
1.2 Non-Destructive Testing (NDT) and the Applicability of Fracture Mechanics 4
1.3 Thesis Objectives 6
1.4 Thesis Layout 7

CHAPTER 2 BACKGROUND ON EDDY CURRENT NDT 9

2.1 Conventional Eddy Current Testing 9
2.2 Defect Detection Parameters 14
2.3 Magnetic Limitations of Conventional Eddy Current Methods 16
2.4 Existing Deep Penetrating Methods 18
2.4.1 Isolation of the Eddy Current Detector 18
2.4.2 Pulsed Eddy Current Method 19
2.4.3 Remote Field Eddy Current Method 21
2.4.4 Comparison of RFEC and PEC Techniques 22
2.5 Fracture Mechanics: a Logical Extension of NDT 24
2.6 Summary 28

CHAPTER 3 REMOTE FIELD EDDY CURRENT METHOD 31

3.1 The RFEC Effect in Ferromagnetic Pipe 31
3.2 Practical Aspects of RFEC Inspection 34
3.2.1 Setup of a RFEC Probe 34
3.2.2 Drill Pipe Geometry Considerations 35
3.2.3 Speed Limitations 37
3.2.4 Signal Interpretation 39

3.2.5 Discussion 40
3.3 Defect Detectability 41
3.3.1 Evidence of Circumferential Fatigue Crack Detectability 43
3.3.2 Discussion of the Detectability of Fatigue Cracks with RFEC 44
3.4 Summary 45

CHAPTER 4 DESIGN OF THE RFEC TESTING RIG 47

4.1 Introduction 47
4.1.1 Overview 47
4.1.2 Test Pipe Assumptions 47
4.2 Design of the RFEC probe 48
4.3 Data Acquisition System 51
4.4 Calibration and Optimisation 53
4.4.1 RFEC Probe Calibration 53
4.4.2 Optimisation of Data Acquisition and Post-Processing Systems 54
4.5 Experimental Design 55
4.5.1 Testing Rig 55
4.5.2 Defect Fabrication 57
4.6 Summary 60

CHAPTER 5 DETECTION OF CIRCUMFERENTIALLY ORIENTED SAW-CUTS 63

5.1 Introduction 63
5.2 Pilot Study 63
5.2.1 Methodology 64
5.2.2 Single Scan Results 65
5.2.3 Discussion of Defect Detectability 68
5.3 RFEC Detector-Array Results 71
5.3.1 Methodology 72
5.3.2 Detector-Array Strip Charts 74
5.3.3 Discussion of Detector-Array Results 77
5.4 RFEC Probe Calibration and Signal Interpretation 78
5.4.1 Calibration Methodology 79
5.4.2 Discussion of Calibrated Results 81
5.5 Summary 83

CHAPTER 6 FATIGUE CRACK SIMULATION **85**

6.1 Introduction 85

6.2 Zero-width Defect Simulation 86

6.2.1 Background on RFEC Defect Simulation 86

6.2.2 Methodology 87

6.3 Experimental Setup 89

6.4 Simulated Fatigue Crack Results 91

6.4.1 Field Perturbation Measurements of Simulated Fatigue Cracks 91

6.4.2 Validation of Results 92

6.5 Summary 94

CHAPTER 7 DISCUSSION **97**

7.1 Practical Implications of RFEC in Marine Drill Pipes 98

7.1.1 Drill pipe RFEC probe design 98

7.1.2 Cost of Operations and Probe Speed 101

7.2 Zero-Width Defect Simulation 102

7.3 Fracture Mechanics Evaluation 104

7.3.1 Determination of Fracture Mechanics Parameters 105

7.3.2 Fatigue Life Prediction 107

7.4 Project Summary 111

CHAPTER 8 CONCLUSIONS AND FUTURE WORK **115**

8.1 Summary of Achievements 115

8.2 Future Work 117

8.2.1 Future Research 117

8.2.2 RFEC Drill Pipe Implementation 118

REFERENCES **121**

Appendix A: Testing Ferromagnetic Materials with RFEC **129**

Appendix B: Email Correspondence **135**

Appendix C: Circuit Diagrams **139**

Appendix D: Matlab Code **145**

Appendix E: Strip Chart Analysis **149**

Appendix F: Graph of Predicted Slit Profiles **155**

LIST OF FIGURES

Page

Figure 1.1 – The Vertical Marine Mining method, modified from Ref. [6] 2

Figure 1.2 – Drill pipe bending due to irregular seabed (left) and ocean currents (centre) causing tensile and compressive stresses (+/-),Failure by fatigue, discussed below, is shown (right). 3

Figure 1.3 – Pipe views showing fatigue crack orientation (left) and propagation (centre) which ultimately leads to drill pipe fracture and failure of the drill string (right) 3

Figure 2.1 – The operation principle of an eddy current sensor (Wenxuan [20]) 11

Figure 2.2 – The Skin Effect (GE Inspection Technologies [24]) 13

Figure 2.3 – Eddy current crack interaction, showing eddy current flow in (a) un-cracked and (b) cracked conductive materials. 14

Figure 2.4 – Detector deviation from the reference signal in response to defects (GE Inspection Technologies [24]) 14

Figure 2.5 – Defect orientation effects on eddy current response (from Ref. [11]) Contours represent current density (J) 15

Figure 2.6 – The effects of increased excitation field strength and lowering excitation frequency on field penetration, signal amplitude (left) is relative to surface eddy current density (Mook [14]) 16

Figure 2.7 – Showing time (t) and distance (d) isolation, contours represent the sphere of influence of surface, near-surface and deep penetrating field trajectories (1–3) 19

Figure 2.8 – A typical PEC signal transient envelope (left) showing exponentially increasing time slices (right), modified from Tian *et al.* [42]. 21

Figure 2.9 – Typical RFECT probe layout showing the indirect energy flow path (from Ref. [50]) ... 22

Figure 2.10 – Fracture toughness input parameters (modified from Ref. [59]) 25

Figure 2.11 – Crack growth rate as a function of its stress intensity factor range (Broek [61]) 27

Figure 2.12 – Fatigue damage striations (modified from Ref. [61]) 27

Figure 3.1 – Schematic of Remote Field Eddy Current testing (Atherton *et al.* [70]) 32

Figure 3.2 – Schematic showing eddy current and magnetic field dominated regions 33

Figure 3.3 – Remote field eddy current signal magnitude and phase (from Ref. [77]) 35

Figure 3.4 – Fill-factor (A1/A2) and lift-off effects 36

Figure 3.5 – 1981mm diameter cement-lined steel pipeline with detector section of RFT tool (from Russell NDE Systems Inc. [65]) 36

Figure 3.6 – RFEC effects in flanged pipe 37

Figure 3.7 – Schematic representation of the trade-offs between the detrimental effects of low and high frequency. Note that frequency is proportional to the maximum scanning speed possible and therefore, in general, probe speed is closely associated with frequency 38

Figure 3.8 – Internal-external pit sensitivity (Schmidt [83]) 39

Figure 3.9 – Multiple RFEC traces off a circumferential weld (Schmidt [83]) Exciter signals appearing downstream from detector signals, in its current position the probe signal is due to interaction at the exciter coil. 40

Figure 3.10 – Internal scale (A) and inner lining (B) in cast iron water pipe, both successfully tested by RFEC (Russelltech NDE [65]) 40

Figure 3.11 – Single detector trace of simulated external flaws in steel pipe (modified from Schmidt [83]) 42

Figure 3.12 – Thermal, circumferentially oriented, fatigue cracking (Russelltech [85]) 43

Figure 3.13 – Simulated phase perturbation induced by an interior slit defects as a function of slit width (Atherton [72]) 44

Figure 3.14 – Map of magnetic poynting vector directions (a) and corresponding field amplitudes (log(Wb/m)) in the vicinity of an 80% deep 6.7% wide far side slit (b) by Atherton and Czura [50] 44

Figure 4.1 – RFEC probe showing the exciter coil, the axially aligned detector coil and nylon probe structure (Teitsma [76]) 48

Figure 4.2 – The RFEC probe layout 49

Figure 4.3 – Electrical schematic of the RFEC probe 50

Figure 4.4 – Data acquisition schematic 51

Figure 4.5 – Representation of reference and detector signals in the frequency domain 52

Figure 4.6 – Field strength from pullout tests 53

Figure 4.7 – Sampling and processing time allocations 54

Figure 4.8 – RFEC testing rig overview 55

Figure 4.9 – Push-rod guide (nylon bushing) shown in position for testing 56

Figure 4.10 – Fatigue crack shapes 58

Figure 4.11 – Hack-saw blade (a) and diamond blade (b) 58

Figure 4.12 – Cut-off wheel schematic 59

Figure 4.13 – Cut-off wheel clamped to the work-station (left) with the blade, blade supports and bolt (depth control) shown (right) 59

Figure 4.14 – Final RFEC testing setup 61

Figure 5.1 – Amplitude results from RFEC testing of the full pipe length as crack depth increases ... 65

Figure 5.2 – Phase results from RFEC testing of the full pipe length as crack depth increases 67

Figure 5.3 – Superimposed amplitude and phase signals 69

Figure 5.4 – Background noise subtracted amplitude component of the signal from the defect region 71

Figure 5.5 – Pipe cross-section showing the 5 circumferential detector scanning positions to generate array data. Top dead centre (TDC) is at 0 degrees (0mm) and corresponds to the maximum depth part of the slit profile 72

Figure 5.6 – Array inspection results from 2mm deep straight fronted and thumbnail shaped cuts 74

Figure 5.7 – Simulated-array results; the amplitude signal component 75

Figure 5.8 – Simulated-array results; the phase signal component 76

Figure 5.9 – 2mm depth strip chart showing straight fronted and thumbnail shaped defect signals 78

Figure 5.10 – Peak-to-peak method showing a single scan of straight fronted and thumbnail shaped defect signals 79

Figure 5.11 – Examples of defect inspection results showing a=1mm and 2mm results 80

Figure 5.12 – Peak-to-peak amplitude signal vs. defect depth calibration curve 81

Figure 5.13 – RFEC defect signal calibration accuracy 82

Figure 6.1 – Extraneous metal and pipe showing constant cross-section 87

Figure 6.2 – Schematic of the defect simulation method 88

Figure 6.3 – Pullout tests to validate the probe design for pipe geometries shown in Table 6.1 90

Figure 6.4 – Signal levels showing amplitude and phase separately 91

Figure 6.5 – Natural log of amplitude vs. normalised defect width for simulated (sim) test results superimposed on embedded (emb) test results. 93

Figure 6.6 – Phase vs. normalised defect width 94

Figure 7.1 – Similarities between early defect signals and background signals 100

Figure 7.2 – Multiple axial detector stages used to permit increased probe speed without loss of signal quality 102

Figure 7.3 – Zero-width defect (a) and 'no defect' (b) cases 103

Figure 7.4 – The effect of defect length ($2c$) and depth (a) on the mode 1 stress intensity factor 106

Figure 7.5 – Real time axial, bending and torsional stress data measured on the upper (Pod 1) and lower (Pod 2) positions on the drill string (Press and Tait [7]) 108

Figure 8.1 – RFEC prototype with shielding (Robinson [107]) 119

LIST OF TABLES

Table 6.1 – Table of properties including actual and predicted phase results 91

Table 7.1 – Amplitude and phase perturbations of fatigue cracks compared to background signal ... 103

Table 7.2 – Defect depth measurement errors 107

Table 7.3 – Fatigue life prediction parameters 109

Table 7.4 – Significant RFEC measurement errors 110

Table 7.5 – Summary of fatigue life estimates 111

LIST OF ABBREVIATIONS AND SYMBOLS

Abbreviations

RFEC	Remote Field Eddy Current
PEC	Pulsed Eddy Current
FEA	Finite Element Analysis
CMRR	Common Mode Rejection Ratio
TDC	Top Dead Centre
ID	Internal Diameter
OD	Outer Diameter
RMS	Root-Mean-Square
RPM	Revolutions Per Minute

Electrical Symbols

δ_{std}	Standard depth of penetration (m)
σ	Conductivity or $1/\rho$ (mhos)
f	Frequency (Hz)
μ	Magnetic permeability (H/m)
J	Electric current density (A/m^2)
Js	Surface electric current density
θ	Direct coupling phase lag (current source reference)
B	Magnetic field density (T - Tesla)
B_s	Surface magnetic field density
Φ	Magnetic flux (Wb, $T \cdot m^2$)
ω	Angular frequency (rad/s)
I_m	Maximum current (A)
I_{enc}	Current enclosing curve C
H	Magnetic H-field (A/m)
dl	Differential element of curve C

E	Electric field (V/m)
$A_{1,2}$	Amplitude of detector or reference signals
$\varphi_{1,2}$	Phase of the exciter or the detector

Mechanical Symbols

σ	Stress (Pa)
σ_r	Remote stress
a	Nominal crack depth
$a_{i,crit}$	Initial or final (critical) crack depths
da	Fatigue crack advance due to a single loading cycle
N_f	Number of loading cycles until failure
dN	Incremental loading cycle
C	Compliance relationship
K	Stress intensity factor ($MPa.m^{1/2}$)
K_I	Mode I stress intensity
K_{Ic}	Fracture toughness or critical stress intensity (Mode I)
m	Chevalier's correction constant
Y	Geometry correction factor
t	Batch processing/demodulation time (s)
dz	Axial spatial resolution (mm)
V_{max}	Maximum inspection speed (mm/s)
B	Wall thickness

CHAPTER 1 INTRODUCTION

1.1 Background on Diamond Mining

Since early 1958, marine diamond mining off the coast of Namibia has been a lucrative operation due to Namibian reserves being some of the richest in the world. To date Namibian un-mined diamonds are estimated at 100 million carats securing operations for a number of years to come [1].

This abundance spurred the development of various methods to improve access to the diamond-rich sediment of the sea bed[1]. The Vertical Marine Mining technique is a particularly successful technique first developed by De Beers in the 1980s. This technique has recently become a major player among the various Namibian mining operations, increasing its yield by 60% in the last decade [2]. Indeed De Beers has reported that, over the last few years, marine mined diamonds have exceeded those produced by land-based mines. These reports claim that marine mining independently produced 0.6 million carats in 2009, and one million carats in 2010, results which more than double those achieved by Namibia's land-based operations [3]. This trend, partially realised by the relative maturity of land based mining, has been maintained to this day with marine mined diamonds currently accounting for 64% of Namdeb's total diamond production and 90% of its forecasted diamond resources. This provides strong evidence that marine mining will play an increasingly dominant role in De Beers diamond production in the future [4].

The Vertical Marine Mining technique involves the lowering of a pipe–drilling structure called the drill string, to the ocean floor through the hull of the mining vessel (Figure 1.1). The drill string is comprised of a series of steel pipe sections and, attached to the bottom, an inverted cone shaped drill head. The drill string is assembled sequentially from the ship's deck. That is, the drill head is lowered through a moon pool in the hull of the mining vessel to the sea bed by the pipe sections as they are successively bolted to the drill string from the surface. The drill pipe currently in use is 500mm diameter, with a 15mm wall thickness, and each individual pipe section is flanged at both ends for bolting to adjacent pipe sections. The drill string typically accesses depths of 150±50m and takes approximately 12 hours to deploy [5].

[1] Early methods involved sediment retrieval using human divers but were restricted to depths less than 35m.

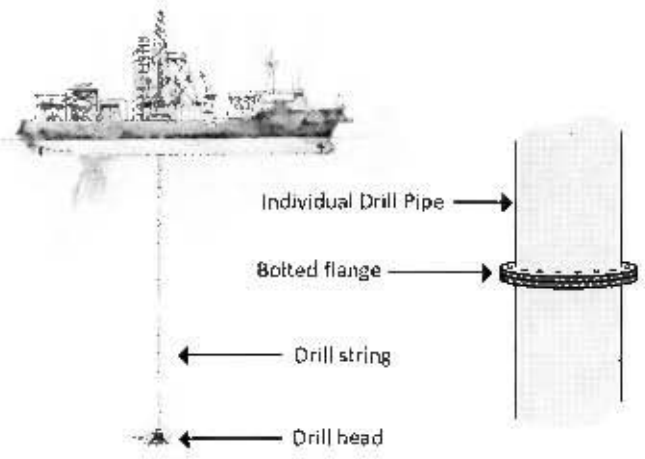

Figure 1.1 – The Vertical Marine Mining method, modified from Ref. [6]
Note: drill string and drill head assembly (left), inset showing an enlarged bolted flange connection (right), (not to scale).

The sediment of the sea bed is loosed and made waterborne by the drill head which is rotated from the surface by onboard motors at approximately 6 rpm. Thus the drill string performs two functions: transmitting torque to the drill head and transporting the loose diamond bearing sediment to the surface. The latter is facilitated by air hoses which run down the sides of the drill pipe and inject air into the drill head. The resulting pressure difference entrains water, sand and sea bed diamonds to be airlifted up the drill string to the ships surface where it is processed immediately by an onboard sorting plant. This method has remained fundamentally unchanged since its development, though its success has brought about the use of increasingly larger diameter drill pipes for higher throughput and thicker pipe walls to improve the service life of each pipe segment [5].

It is important to note that the schematic above (Figure 1.1) does not show the dynamic effects of the mining operation, these effects are better represented in Figure 1.2. In reality, ocean currents, rolling of the vessel and sea bed morphologies[2] result in significant deflections in the pipe. These deflections and rotation of the drill pipe during operation result in cyclic compressive and tensile stresses. In addition, the drill head, which is 7m diameter and weighs approximately 65 tons, introduces stress fluctuations due to 'stick-slipping' in the slurry of the seabed [7].

[2] Sea floor irregularities force an incline on the drill head and a bend in the drill string, see Figure 1.2.

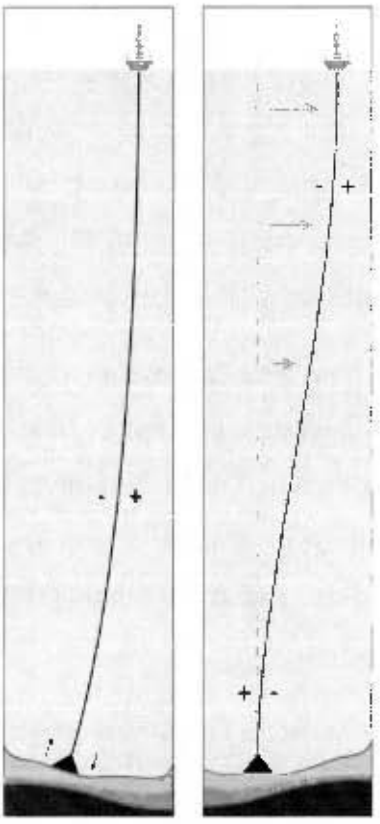

Figure 1.2 – Drill pipe bending due to irregular seabed (left) and ocean currents (right) causing tensile and compressive stresses (+/-).

Combinations of corrosion and the cyclic operating stresses described above have been found to cause fatigue cracking in the drill pipe. These cracks tend to be circumferentially oriented, 'thumb-nail' shaped and initiate on the outside wall of the drill pipe and propagate inwards. Continued drill operation and the associated cyclic stresses then cause the fatigue cracks to propagate inwards from the outside wall (Figure 1.3).

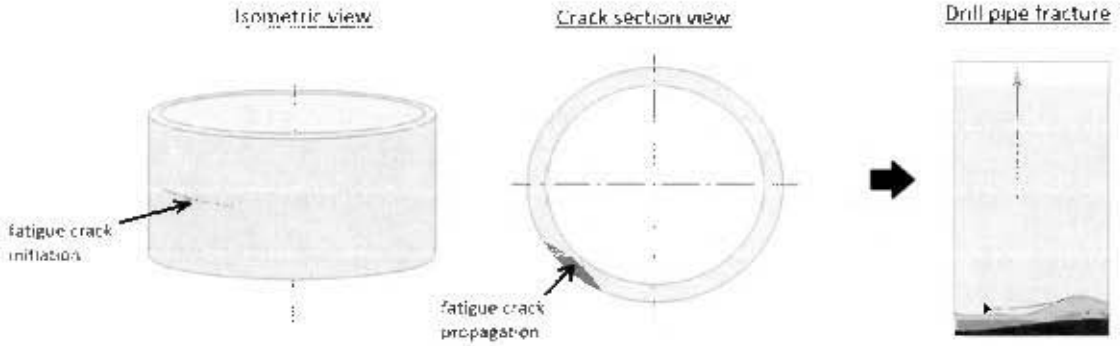

Figure 1.3 – Pipe views showing fatigue crack orientation (left) and propagation (centre) which ultimately leads to drill pipe fracture and failure of the drill string (right)

impractical[6]. In these cases detection from the pipes outer surface is not viable due to pipelines often being buried, submerged or obstructed by supports [9]. Therefore substantial NDT research has emerged from this industry, most of which is directed at broadening the range of defects detectable by a single method to save costs. Here, the opposite is required, the evaluation of existing NDT methods for those best suited to the detection of a single type of defect. Circumferential fatigue cracks, usually atomically sharp and narrow, are detectable by few NDT methods which in many cases rely on appreciable defect volume for reliable readings [10]. In addition, many methods require specific surface conditions or preparation, requirements which are generally not possible in submerged applications [10].

Eddy current testing, a branch of Electromagnetic NDT, is an effective method for the inspection of defects in conductive materials [11]. The method is highly sensitive to fatigue cracks, requires no preparation or direct contact with the surface of the target and provides instantaneous results [12]. These features make eddy current testing ideal for marine applications, particularly as it is also relatively unaffected by the medium through which it operates (water, air etc) [11]. However, the method is also generally limited to the detection of surface and near-surface defects. As drill pipe fatigue cracks must be detectable on the external surface from the inside (i.e. through the full wall thickness), this is a key research objective in this project. Fortunately, many researchers have recognised the limited depth of penetration as a salient limitation of the eddy current method (particularly for the gas and oil transmission industry [13]) giving rise to various innovative methods to improve the depth of penetration [14]. Therefore the research objective of this project is the review of existing NDT methods for fatigue crack measurement.

Generally, any flaw measurement results must be linked to the structural integrity of the overall structure; therefore there is a secondary need to understand what size defects justify intervention. It would be absurd to address all defects as critical while many defects may never propagate, and most that do propagate under fatigue conditions remain stable for a significant portion of the pipes service life [15]. Fortunately, quantitative answers to these questions are possible with the help of Fracture Mechanics.

[6] The Enbridge pipeline is one such example exceeding 5000 kilometres between Canada and the United States.

Due to the lack of availability of drill pipe or actual fatigue cracks for testing in this project, a prototype probe is designed and tested on representative pipes and defects. Therefore the final objective is to account for the differences between the prototype and the drill pipe systems, particularly toward the final implementation of a drill pipe inspection system.

1.4 Thesis Layout

It was considered appropriate to include a brief section explaining the philosophy and layout of this thesis. The thesis layout corresponds closely to the order in which the objectives are listed above.

As the eddy current method is already identified as a key technology in this project, it is firstly appropriate to review the fundamental principles of eddy current testing (Chapter 2). These principles highlight the fundamental depth limitation of eddy current testing; therefore a logical 'next step' was to review principles for deep penetrating eddy current methods. This theory is used to review two methods considered applicable to this project. Therefore a significant outcome of this chapter is a motivation for the method most applicable to this project. From this point in the document onwards, only the chosen method is studied. Therefore the following chapter, Chapter 3, elaborates on the chosen method; this includes the fundamental principles of the method, practical considerations relevant to its implementation in drill pipes, and relevant limitations. Thus far, Chapters 2 and 3 address objective (1).

The building of the NDT system was carried out in Chapter 4, and the capabilities of the system are tested in Chapters 5 and 6. It should be noted that development of the NDT system continues somewhat from Chapter 4 into Chapter 5. This was because no existing NDT system was available to provide a benchmark of results. However, the main aim of Chapter 5 is to determine the detectability of circumferential defects as a function of depth.

As alluded to in the objectives above, the inspection of true fatigue cracks in actual De Beers drill pipe was not possible, furthermore, although appreciably narrow slits could be manufactured, these were still wider than actual fatigue cracks. Therefore it was considered an important follow-on section from Chapter 5 to simulate true fatigue cracks

CHAPTER 2 BACKGROUND ON EDDY CURRENT NDT

This chapter provides general information on current electromagnetic technologies used for the detection and sizing of fatigue cracks. This includes the identification of a suitable technology for inspection of the outer surface of marine drill pipes from the inside. The theory of conventional eddy current testing is reviewed which focuses primarily on the depth limitations outlined in Chapter 1. This is necessary before the subsequent discussion and evaluation of methods which circumvent these limitations contained in this chapter.

Sections that follow examine current deep penetrating eddy current methods for ferrous pipeline inspection. Note that these methods are only outlined in this chapter; more detailed analysis of the method chosen for this thesis is presented separately in Chapter 3.

As this chapter covers various eddy current inspection methods, and as such methods are generally only the first stage of a broader structural integrity assessment program; this chapter also includes the fundamental Fracture Mechanics principles required for the analysis of fatigue cracks in terms of 'risk of fracture'. The intention of this final section is to show the usefulness of certain crack geometry data, which lends itself to a simplified interpretation of the requirements from the NDT system tested in this thesis.

2.1 Conventional Eddy Current Testing

Eddy current testing was first devised by David E Hughes in 1879 as a method for sorting coins using the coils of the early telephone [17]. Hughes observed that the impedance properties of a coil were altered when brought close to materials with different electrical properties (conductivity and permeability). Thus eddy current testing was first proposed as a method for sorting materials by their electromagnetic properties. Though his method is crude by modern day standards, it remains fundamentally unchanged in the diverse applications found today [18].

$$\oint_C \vec{E} \cdot \overrightarrow{dl} = \frac{d\mu H_1}{dt} \tag{2.3}$$

in which μ is the material magnetic permeability and E is the induced electric field. The electric field drives circulating 'eddy' currents (I_2) in the conductive target material. I_2 creates a secondary field H_2 again due to amperes law (2.1) which partially couples with the exciter coil. The resultant field is a vector sum of the primary and secondary H-fields. The inductive characteristics of the material introduce a phase lag to the penetrating field as it diffuses below the material surface [19]. Therefore the resultant field induces a lagged voltage by amount θ between H_1 and the resultant field as a result of Faradays law

$$v(t) = -N\frac{\partial \Phi}{\partial t} = V_m \sin(\omega t + \theta) \tag{2.4}$$

where N is the number of coil turns, and Φ is the magnetic flux 'threading' each single turn.

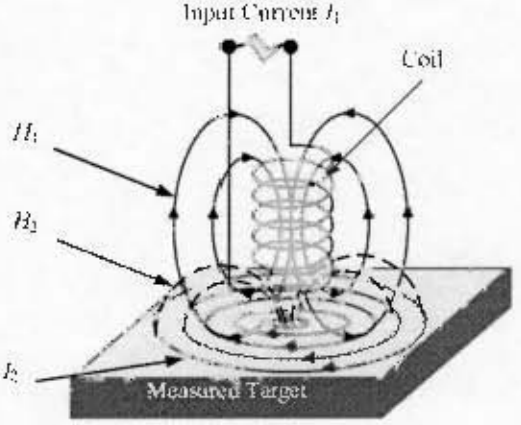

Figure 2.1 – The operation principle of an eddy current sensor (Wenxuan [20])

Lenz's law describes that H_2 is induced in opposition to H_1. This results in a nulling effect to all fields penetrating conductive materials. As a result the eddy current density is strongest at the surface and the field energy is dissipated by resistive heating of the electrical current flow. These effects prevent deep penetration such that electromagnetic waves tend to be strongest near the surface of the target conductive material; this phenomenon is called the 'skin effect' [20].

While a more thorough explanation may be obtained by the study of Maxwell's equations [21], eddy current concepts traditionally assume plane wave propagation into a conducting half-space to describe the skin effect. This is modelled mathematically by the solution of the elliptical diffusion equations derived by Lord [22], giving rise to the skin depth equations for electrical and magnetic field densities at depth d below the material surface (Equation 2.5). Hence the attenuation of the electric current density (J) in terms of its surface value (J_s) is described as

$$J = J_s e^{-d\sqrt{\pi f \mu \sigma}} \sin\left(\omega t - d\sqrt{\pi f \mu \sigma}\right) \tag{2.5}$$

Similarly the associated alternating magnetic field density B can be represented as [23]

$$B = B_s e^{-d\sqrt{\pi f \mu \sigma}} \sin\left(\omega t - d\sqrt{\pi f \mu \sigma}\right) \tag{2.6}$$

Where: σ - Conductivity (mhos), or $1/\rho$ where

ρ - Resistivity (Ω·m)

f - Frequency (Hz)

J - Electric current density (A/m^2)

J_s - Surface electric current density

B - Magnetic field density (T - Tesla)

B_s - Surface magnetic field density

Ceteris paribus, Equations 2.4 and 2.5 show that amplitude is attenuated exponentially and phase retardation is a linear function of depth.

It is mathematically convenient to define a standard depth of penetration (δ_{std}) as the depth to which the surface current density has decayed 36.8% (or 1/e) of the surface current density and lags the surface phase by 1 radian (Figure 2.2).

This is given as

$$\delta_{std} = \frac{1}{\sqrt{\pi\sigma\mu f}} \tag{2.7}$$

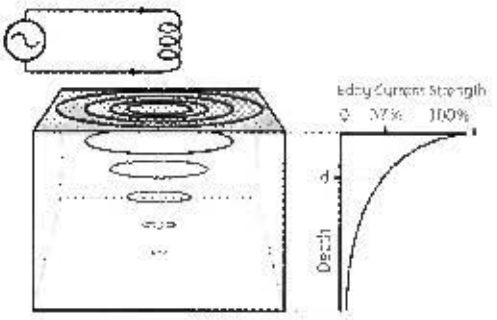

Figure 2.2 – The Skin Effect (GE Inspection Technologies [24])

Equation 2.7 is a useful qualitative tool to describe the factors affecting subsurface detection[9]. In particular, the skin depth equation highlights the frequency dependence of eddy current methods. By lowering the excitation frequency, greater depth of penetration is achieved.

It is also shown that depth of penetration is limited by the electromagnetic properties of the test material (conductivity and permeability). These parameters are also defect indicators; in other words, defects are only observable by eddy current methods if the nature of the defect influences these properties. However, permeability and conductivity variations are inherent in materials. Therefore a key aspect of eddy current methods is identifying defects from other material inhomogeneities [25]. Although conductivity and permeability are defect indicators, modelling of these field interactions requires more sophisticated simulations. Eddy current defect interactions are explained in the following section. It should be noted that these are generalized; technique specific interactions are discussed in Chapter 3.

[9] The assumptions used to derive equation 5 make precise calculations inaccurate, for accurate quantitative studies, finite element simulations are used to simulate field distributions.

2.2 Defect Detection Parameters

To summarize, when the eddy current detector coil is brought close to a continuous conductive surface, the secondary field (II_2) forms in opposition to the primary field (H_1) (Figure 2.3), thereby reducing the coils overall impedance. The presence of a crack tends to interrupt or distort the eddy currents (I_2) and the formation of the secondary field (II_2).

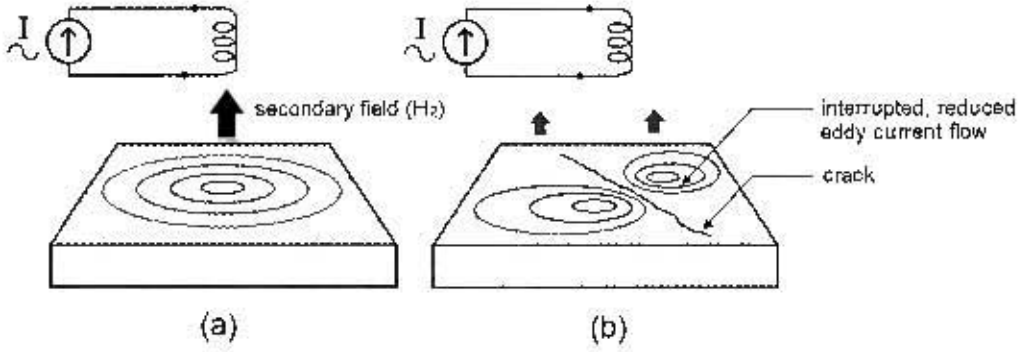

Figure 2.3 – Eddy current crack interaction, showing eddy current flow in (a) un-cracked and (b) cracked conductive materials.

This results in a net increase in the field threading the cross-sectional area of the detector coil (Equation 2.4) such that the coil impedance increases. This results in an increase in the voltage amplitude and a decrease in phase lag relative to the phase of the driving current (assuming that the coil is driven by a constant amplitude current source) as shown in Figure 2.4.

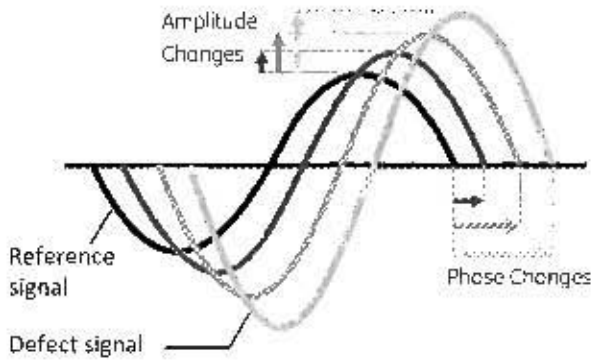

Figure 2.4 – Detector deviation from the reference signal in response to defects (GE Inspection Technologies [24])

The phase lag and amplitude attenuation are defined relative to a reference signal (from the driving current). The extraction of amplitude and phase data from the detector and reference signals is a process called demodulation. This terminology extends to the test material which is said to modulate the source signal (the reference) by affecting its amplitude and phase according to its capacity to support eddy current flow.

Eddy current methods are highly sensitive to fatigue cracks. This is because fatigue cracks present an electrical discontinuity blocking the even distribution of eddy currents as can be seen in Figure 2.3. This is the reason that eddy current methods are highly sensitive to planar cracks with relative immunity to low defect volumes. Note that defects must interrupt the eddy current flow to be detected, therefore planar flaws oriented parallel to the eddy current flow will not necessarily be detected (Figure 2.5).

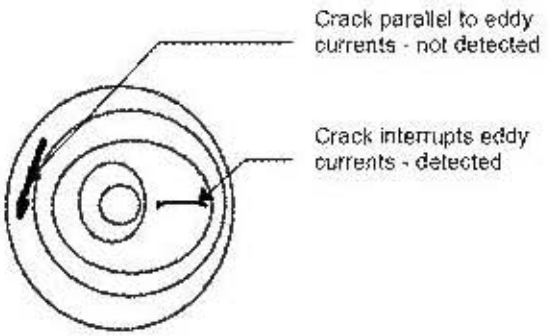

Figure 2.5 – Defect orientation effects on eddy current response (from Ref. [11])
Contours represent current density (J)

In general, the linear response of the signal phase as a function of depth (shown in Equations 2.5 and 2.6) enables its use as a defect depth transducing parameter[10]. Amplitude is generally more complex to interpret, and, due to its exponential nature, is typically represented on a log scale [26].

The previous explanation has only described conductivity related defect indications. Magnetic field indications occur such that serious considerations arise from subsurface inspection of ferromagnetic materials using conventional eddy current testing.

[10] The 'd' shown in Equations 2.5 and 2.6 refers to the depth below the surface of the conductive medium, this does not relate directly to the measurement taken externally. This is more complicated than described in this document.

2.3 Magnetic Limitations of Conventional Eddy Current Methods

Fatigue cracks are arguably the most pervasive and yet most difficult to detect defects by most other NDT methods [27]. As a result of eddy current sensitivity to fatigue cracks, subsurface detection using eddy current testing is often desirable. Certain applications for subsurface inspection by conventional eddy current testing have emerged despite the inherent depth limitations. This has seen considerable development of deep penetration eddy current surface probes for aerospace industries, particularly for the inspection of multilayered aluminium aircraft panelling [6, 7].

In general, subsurface defect sensitivity is improved by using wide area coils, low frequency activation, and high amplitude excitation as shown in Figure 2.6 [14].

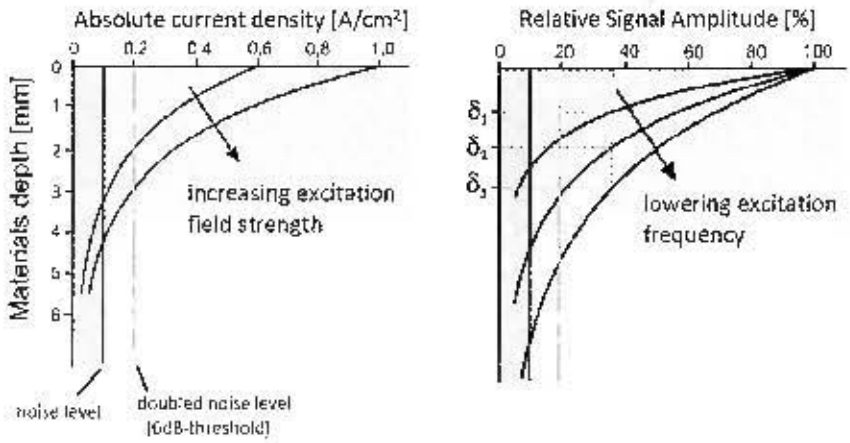

Figure 2.6 – The effects of increased excitation field strength and lowering excitation frequency on field penetration, signal amplitude (left) is relative to surface eddy current density (Mook [14]).

However, these types of probes tend to be prone to poor lateral resolution as a result of the large area coils required, and reduced sensitivity from the use of low frequencies[11]. As a result, these methods rely on high gain, low noise amplification to improve sensitivity [30]. These methods also tend to require high amplitude fields to increase the strength of subsurface fields. This is often limited by problems associated with coil heating [14]. Despite these limitations, low frequency eddy current instruments achieve

[11] Low frequencies reduce the overall coil impedance such that the received signal is of very low voltage.

reasonable results provided that the target material is nonmagnetic (i.e. not ferromagnetic) [6, 7]. However, the conventional methods for optimizing depth of penetration described above are not sufficient for the inspection of high permeability materials, as magnetic flux tends to spread laterally away from the area of interest [31]. Previous studies have found that low frequency eddy current programs for the inline inspection of outer defects in ferrous pipelines are unable to inspect reliably from the inside [31].

Magnetic permeability is dependent on the size and polarity of granular magnetic domains throughout the material, the distribution of which is often inconsistent as it is highly dependent on the materials alloying and manufacturing processes. This often results in major permeability variations compared to conductivity, which is relatively homogenous in these cases [32]. Furthermore, the indications from permeability related defects (pitting and large area material loss) tend to be greater than those brought about by obstruction of eddy currents (fatigue cracks) [33]. These effects cause a high occurrence of false flaw indications in ferrous materials, making permeability a generally undesirable material property for successful electromagnetic NDT [33].

Therefore it is common practice to saturate ferromagnetic materials magnetically during testing [18]. Full magnetic saturation of a magnetic material effectively transforms it into a non-magnetic material from an electromagnetic perspective. This is achieved by applying a strong DC magnetic field to the test material, which aligns the polarities of the magnetic domains. While saturation assisted eddy current methods often use permanent magnets, many implementations achieve this simply by superimposing a DC field over the harmonic activation signal in the probe coil [14]. Applying saturation to the test area tends to reduce the effects of permeability variation and improve the depth of field penetration by driving the relative permeability of the material to unity (i.e. that of free-space) [14]. However, previous studies have shown that in general it is found that full saturation is seldom reached experimentally, particularly in ferromagnetic pipes[12] [31,34].

Recently, the traditional use of saturation and low frequencies has been surpassed by methods which employ special probe geometries [35]. These methods typically operate with a heavy wound exciter coil and a dedicated detector coil (two separate coils) [36]. This makes it possible isolate deep penetrating field trajectories and the separate

[12] These investigations found that saturation assisted eddy current testing were approximately 50% as effective as predicted, defined by standard depth of penetration (mm) with the conclusion that full saturation is seldom achieved experimentally.

optimisation of the exciter and the detector [37]. As the signal is now sent from the exciter to an isolated detector by "reflection" through the test material, this configuration is called reflection mode[13]. The following section refers to reflection mode to discuss the innovative deep penetrating methods alluded to in Chapter 1.

2.4 Existing Deep Penetrating Methods

Two methods are identified as contenders for further research in this thesis; the Remote Field Eddy Current (RFEC) method, and the Pulsed Eddy Current (PEC) method. These methods share the ability to isolate deep penetrating fields from the dominating surface electric and magnetic fields which otherwise tend to blind subsurface detection. Before these two methods are reviewed, the philosophy of detector isolation is discussed to introduce these methods. This philosophy is referenced later in the chapter as it is useful in understanding the limitations of each method.

2.4.1 Isolation of the Eddy Current Detector

Deep penetrating strategies fundamentally rely on the generation and detection of deep field trajectories [14]. Early methods achieved this using the multi-frequency eddy current technique to sample material at different depths. This operated by scanning the test material with multiple frequencies either in rapid succession (asynchronous) or mixed signal (synchronous) modes. In the post-processing of this data, it is possible to improve the quality of deep data corresponding to low frequency excitation by subtraction of high frequency surface data [38]. However, these methods are limited as the coupling path is based on direct coupling[14] with the material surface [14]. Indirect coupling is possible by isolating the detector coil from the exciters immediate field[15] (Figure 2.7). Two methods highly effective at achieving this are described below and refer to Figure 2.7.

- The most common method distances the detector from the exciter such that it becomes incident with deeper field trajectories ($d_0 - d_3$) [14]. This offers high defect resolution as the magnetic field is permitted to diffuse over greater

[13] Other names include 'driver-pickup' and 'send-receive' mode.
[14] Although direct coupling is not explicitly defined in this section, it describes in general the intense magnetic field found in the vicinity of the field generating coil generally responsible for the increased sensitivity to surface defects.
[15] Note that for this to be possible, the eddy current instrument must operate in reflection mode. That is with a separate exciter and detector to generate and detect the magnetic fields respectively.

distances and therefore is more evenly distributed through the material thickness [35]. In this way the detector is isolated from the exciters direct field and instead tends to couple with the indirect or 'remote' field. A significant advantage of this method is that it enables the manipulation of the coupling path by the location of the detector with respect to the exciter [35]. Methods which use distance isolation are ubiquitously called Remote Field Eddy Current (RFEC) methods.

- A second effective method isolates the exciter and the detector in time rather than in space [39]. This is done by activating the exciter coil for a brief period after which it is quiet while the transient field, still diffusing through the material, is recorded ($t_1 - t_3$). For this reason, these methods are called transient or Pulsed Eddy Current (PEC) methods. The time dependence of the transient field is what allows surface data to be distinguishable from subsurface data [40]. A major advantage of this method is that isolation of the detector in time prevents direct coupling from the exciter regardless of its position with respect to the exciter. This allows flexible placement of the detector making more compact probe designs possible [39]. More detailed descriptions of both Pulsed Eddy Current and Remote Field Eddy Current methods are given in the following sections.

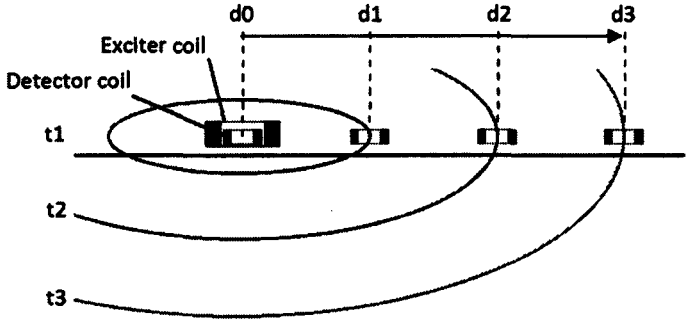

Figure 2.7 – Showing time (t) and distance (d) isolation, contours represent the sphere of influence of surface, near-surface and deep penetrating field trajectories (1–3)

2.4.2 Pulsed Eddy Current Method

It was previously mentioned that it is possible to improve depth of penetration by increasing the amplitude and lowering the frequency of the exciter current, but that these parameters are always subject to coil heating and power limitations. To alleviate these effects and thereby improve penetration, early methods made use of short periods of high amplitude excitation followed by a cooling interval to allow heat to dissipate from the

coil. However, these methods were still fundamentally limited by the skin effect[16] [14]. Multi-frequency methods achieved better performance by pulsing a series of discrete frequencies in quick succession allowing the analysis of data with different depth sensitivities [39]. This was the first step towards evaluating different material depths via post-processing of data.

Pulsed Eddy Currents (PEC) achieves the advantages of both of these methods by simply activating the exciter coil with a pulse train [41]. The use of short pulses enables the use of high amplitude pulses while maintaining relatively low power consumption. A Fourier transform of a single short pulse contains a continuum of frequencies (continuous frequency spectrum) and therefore enables PEC datasets to capture depth related data over a wide band frequency range[17] [41]. Therefore instead of sampling discrete frequencies, PEC is able to capture a continuous frequency spectrum in a single pulse. As a result, PEC methods are generally capable of higher inspection velocities than low-frequency and multi-frequency methods [39].

Once the pulse is emitted from the exciter, the transient field is measured as it propagates into the test material. This pulse is attenuated and phase lagged by eddy current principles as it propagates below the material surface, therefore all field measurements made after the initial pulse capture time-depth data pairs [42]. For this reason the transient signal is usually processed in the time domain instead of the frequency domain commonly used in other eddy current methods, and therefore amplitude and phase demodulation is not needed. As the signal is separated in time between field pulsing and field detection, both tasks may be performed by a single coil[18]. This simplifies probe design and allows PEC probes to be relatively compact [43].

The measured transient has the characteristic peaking envelope shown in Figure 2.8. Until recently, time-to-peak methods were used as the primary defect detection parameter; though this method is still useful as a fast surrogate, superior methods tend to make use of more sophisticated post-processing [43].

[16] These improvements are exponentially decreasingly effective as described by the skin depth equation.
[17] Sampling of the continuous spectrum is a distinct feature of PEC, multi-frequency methods sample only discrete frequencies.
[18] Though field sensors as these are best for low frequency measurement [29].

These methods make use of the time-slice interpretation of data by dividing the signal envelope into exponentially increasing time intervals (Figure 2.8), where each interval is regarded as a variable in multidimensional space.

Effective methods for reducing the dimensionality of this space (while preserving data quality) are available, notably those using Principle Component Analysis[19] (PCA) [43]. PCA is a mathematical procedure widely used in signal processing and small signal identification in sparse or largely redundant data-sets [44–47].

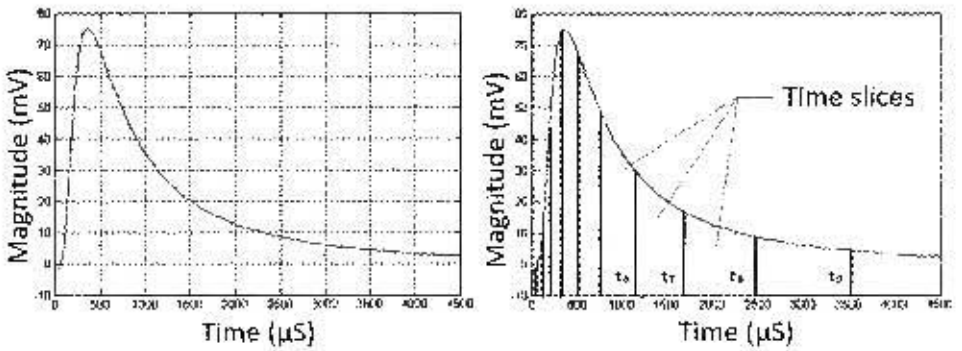

Figure 2.8 – A typical PEC signal transient envelope (left) showing exponentially increasing time slices (right), modified from Tian *et al.* [42].

The post-processing of PEC signals with PCA been shown to significantly improve overall reliability of PEC. These contributions have led to many new applications for this method, especially with the advent of digital technology and its wide availability [43].

2.4.3 Remote Field Eddy Current Method

This section describes technologies which make use of distance isolation from the exciter coil. Although the remote field isolation of the detector from the exciter near field does have flat geometry applications [35], the Remote Field Eddy Current (RFEC) method is generally used as a tube inspection technology. In this geometry the method is known to be able to inspect ferromagnetic and non-ferromagnetic tubes with approximately equal sensitivity to interior and exterior defects with additional evidence that ferrous tubes tend to be particularly sensitive to external defects [48].

[19] This is a statistical method used in signal processing to reduce the size of large datasets while preserving maximum variance. This is achieved by linear transformation of the data into a lower dimensionality subspace of orthogonal eigenvectors.

The method resembles a conventional eddy current probe configured to operate in reflection (send-receive) mode. The principle difference being that the exciter coil is co-axial with the pipe and separated from the detector by several pipe diameters. This configuration enables the detector coil to couple with the exciter coil via the indirect energy flow path shown in Figure 2.9. This field is called the remote field and has a characteristic twice through-wall penetration (once at the exciter and once at the detector). The first wall penetration of the field at the exciter and the distance results in a homogenous field outside the pipe. The second transition back into the pipe at the detector is thus entirely through the pipe wall which results in equal sensitivity to internal and external defects, in seeming defiance of the skin effect [49].

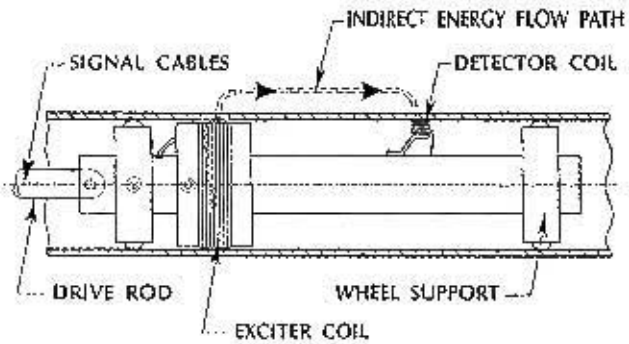

Figure 2.9 – Typical RFECT probe layout showing the indirect energy flow path (from Ref. [50])

Other important advantages include linear relationships between wall thickness and signal phase lag, and relative immunity to mechanical lift-off of RFEC probes [49].

2.4.4 Comparison of RFEC and PEC Techniques

The RFEC and PEC techniques are distinguished by two main features, that is, the activation waveform, and the method for isolating the detector from the exciter. Therefore comparison centres on these two features.

The remote field method is activated by a sinusoidal harmonic which has been shown in previous studies to achieve higher detectability of subsurface defects in ferrous materials than wide band PEC excitation [37,39,40,51]. However, PEC produces a localised penetrating field, which, due to its predominantly radial magnetic field component, is able

to detect radially propagating defects of any orientation with equal sensitivity. The main limitation of PEC is that it is still fundamentally near-sided in the sense that subsurface data is only achieved by post-processing [14]. Contrasting to this, remote field testing is equally sensitive to defects at all depths in the pipe-wall thickness but certain orientations are more detectable than others. For example, RFEC is more sensitive to circumferentially oriented slits than axially oriented slits in ferrous pipe wall. In this project, the cracks are known to be of circumferential orientation and propagate from the outside, radially inwards; therefore the sensitivity to all orientations that PEC offers is *not* considered advantageous.

When inspecting ferromagnetic materials with RFEC, the field strength in the remote field zone tends to be significantly stronger on the outer surface than the inner surface (due to the skin effect as discussed further in Chapter 3) [48]. This causes the principal component of the incident remote field to diffuse radially on the pipe interior and enables detector arrays to achieve excellent lateral resolution [52]. To achieve comparable resolution, PEC coils must be arranged in compact arrays. However, PEC fields tend to spread out laterally from the exciter coil when testing ferromagnetic material and since each PEC probe produces its own field, unwanted coupling must be prevented by ensuring that adjacent coils are never simultaneously activated. This tends to result in a form of signal contamination known as cross-talk [53].

Furthermore, the RFEC method is particularly suited to diamond drill pipe applications as these probes are relatively immune to variations in distance between the exciter coil and the pipe surface. This lift-off is likely in this case as the internal diameters of the drill pipes are known to vary due to the wearing down of the pipe wall by the transported debris [5].

Another notable application specific advantage is that, due to the coaxial alignment of the RFEC exciter coil with the tube, the axial magnetic field propagating through ferromagnetic material is highly sensitive to circumferentially oriented defects [44]. However, it was theorized by Atherton [54] that the detectability of circumferential defects in high permeability pipes is likely only to be possible so long as the defects present a measurable volume. If this were true, it would specifically preclude circumferential fatigue cracks being detectable by RFEC. Correspondence with Atherton indicated that even zero-width defects may give measurable indications and requires

further testing (discussed further in section 3.3) [55]. These concerns are discussed further in Chapter 3 with the provisory that limited plastic deformation reportedly occurs in and around the fatigue cracked material of the drill pipe making it unlikely that defect volume will remain in fatigue crack proportions for the full fatigue life of the defect [5].

This evidence and the promise of detectability with equal sensitivity throughout the pipe wall motivates for the use of the RFEC method for further research. However, if the low detectability of fatigue cracks, great probe length, low probe speed or high power consumption become major constraints at a later stage, it is possible that PEC should be reconsidered. In particular, recent research has shown that these probe length and power consumption can be dramatically reduced by combining pulsed excitation with the remote field geometry – a new method called Pulsed Remote Field Eddy Current (PRFEC) [39,41,56,57]. However, as the primary aim is the improvement of the detectability of fatigue cracks and as there is no evidence that PRFEC contributes to this [40], only narrow band harmonics are studied further in this thesis, that is to say conventional RFEC.

The following section is necessary as NDT systems are generally used as only the first stage of overall structural integrity analysis programs. That is that practical use for crack data can only be gained by post inspection analysis of crack growth rate (requiring data from previous inspections) and risk of failure.

2.5 Fracture Mechanics: a Logical Extension of NDT

While NDT detects the existence of flaws, NDE (Non-Destructive Evaluation) is the management of the existing flaws post detection [58]. Such evaluations are often directed towards learning the maintenance requirements for the system for continued safe operation. In terms of De Beers drill pipe NDT, it is required to know the safe interval between inspections within which fast fracture is not likely to occur.

The field of Fracture Mechanics is an extension of conventional mechanics intended for the evaluation of structures containing flaws. These flaws have in the past resulted in catastrophic brittle failures occurring in ductile materials. Thus, it has become a widespread approach to predict fracture using Fracture Mechanics, particularly in cases involving fatigue [27]. This section focuses on the fitness-for-service assessment of structures by means of providing a working understanding of the Fracture Mechanics

principles involved. This is essential for describing the crack geometry and spatial resolution requirements for later testing using RFEC. Note that the Fracture Mechanics parameters used to describe crack geometry in this project are a and $2c$, as shown in Figure 2.10.

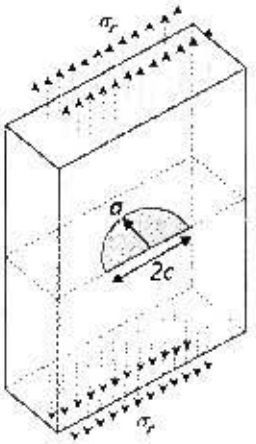

Figure 2.10 – Fracture toughness input parameters (modified from Ref. [59])
Defect depth (a), length ($2c$) and the remote stress σ_r (applied perpendicular to the crack plane) are shown

Linear elastic Fracture Mechanics introduces a term called the stress intensity factor (K). This is used to describe the ability of a material with an existing crack to resist crack growth. For a homogenous material[20] this is expressed as

$$K = Y\sigma_r\sqrt{\pi a} \tag{2.7}$$

where σ_r is a remote stress applied perpendicular to the crack plane, a is the crack depth, and Y is a dimensionless correction factor[21] to account for crack geometry. Note that Y is largely dependent on the crack aspect ratio ($a/2c$), depth, and wall thickness (a/B) [27]. Equation 2.7 was derived by Griffith who noticed that the term $\sigma\sqrt{a}$ tends to reach a particular material dependent value for a range of flaws of the same shape, beyond which fracture predictably occurred [27]. This made it possible to introduce a material property called fracture toughness (K_{Ic}), as the stress intensity at which fracture takes place[22]. Therefore, if a is known, it is possible to determine a safe nominal stress level within

[20] This assumes a two dimensional applied stress/strain field at the crack tip.
[21] The convention is that Y is set to unity for a crack in an infinite sheet.
[22] This is analogous to the ultimate tensile strength defined by classical mechanics.

which a crack will not propagate [27]. This makes it possible to determine the critical flaw size given a small set of characteristics of the crack region, that is: total effective stress, the crack depth, crack length ($2c$) and the critical stress intensity factor or fracture toughness. Therefore, under regular inspections, it is possible to calculate the critical crack depth (a_{crit}) and avoid brittle catastrophic failure of the drill pipe.

Although stable cracks may not present immediate risk, these cracks may propagate under cyclic loading. Thus, over time, stable cracks may grow until instability is reached. Note that NDT inspection only determines the depth of existing cracks at the moment of inspection while Fracture Mechanics (so far) only allows the calculation of critical crack depth. The time spent in propagation between these two limits is of great value for crack monitoring purposes as it allows the possibility of scheduled inspections. Further development of the above theory enables the characterization of fatigue crack growth rate [60]. This theory (described below) facilitates predictions of time-to-failure. This information is useful as part of damage monitoring systems in order to determine reasonable inspection intervals [5].

Figure 2.11 shows fatigue crack growth rate as a function of the stress intensity factor range experienced by a fatigue crack during cyclic loading. The initial and final stages of crack growth (regions I and III) are largely determined by mean stress, material microstructure and environmental conditions making fatigue crack growth rate prediction complicated in these regions [15]. However, a significant portion of the fatigue crack life is spent in the stable growth (region II). This region is described by the Paris equation

$$\frac{da}{dN} = C\Delta K^m \tag{2.8}$$

where the term on the left hand side is the crack growth rate [60]. This is described by the differential crack growth depth (da) per loading cycle (dN) where the range of the stress intensity factor (ΔK) is derived from the maximum and minimum cyclic stresses substituted into Equation 2.7.

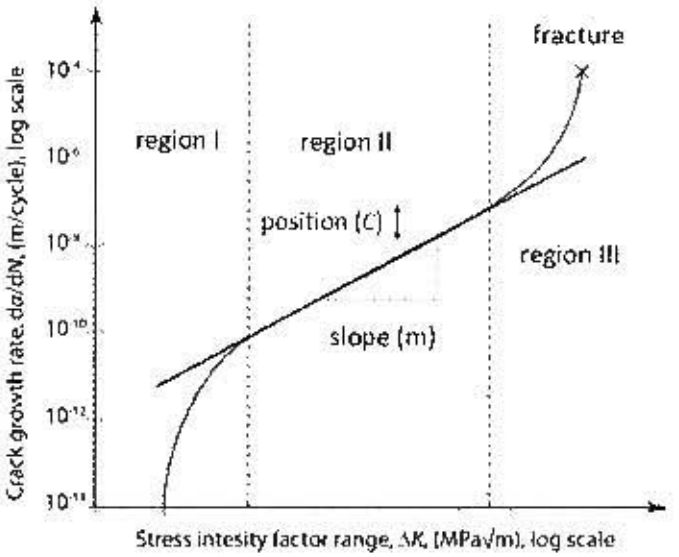

Figure 2.11 Crack growth rate as a function of the stress intensity factor range (Broek [61])

Physically, region II propagation is constrained by the plastic blunting of the crack tip. This process leaves striation marks on a fatigue fracture surface where each striation represents the advance of the fatigue crack due to a single loading cycle by a small distance (da), typically 0.001 to 1 micron. The striation distance is dependent on the stress range ($\Delta\sigma$) as illustrated in Figure 2.12 [61].

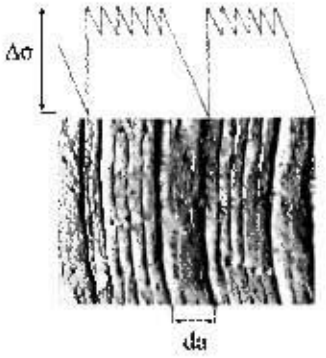

Figure 2.12 -- Fatigue damage striations (modified from Ref. [61])

The exponential nature of Equation 2.8 may be represented linearly on a log-log graph such that two new parameters m and C may be interpreted as the slope and position of the linear region represented in Figure 2.11.

The remaining fatigue life in terms of load cycles can be found by substituting the stress intensity factor into the Paris equation (Equations 2.9 and 2.10) which gives

$$\frac{da}{dN} = C(\Delta\sigma_r Y(a)\sqrt{\pi a})^m \tag{2.9}$$

The number of cycles to failure (N_f) may be obtained by the separation of variables

$$N_f = \int_0^{N_f} dN = \int_{a_i}^{a_{crit}} \frac{da}{C(\Delta\sigma Y\sqrt{\pi a})^m} \tag{2.10}$$

where N_f is the number of loading cycles until failure, a_i is the initial crack depth and a_{crit} is the critical crack depth at failure described by Equation 2.1 [60].

The primary requirement from this thesis is the initial crack depth (a_i). This is because accurate data of the drill pipe loading conditions is already available from previous studies by CRS [7]. Other crack parameters such as *2c* and the aspect ratio are of secondary importance for the generation of the geometrical correction factor (elaborated in the final discussion – Section 7.3.5).

Therefore, if the initial flaw size is known (Equation 2.7) together with the material properties required for solution of the Paris equation (Equation 2.8), one can confidently determine the fatigue lifetime to failure.

2.6 Summary

This chapter has presented three major topics: the introduction of fundamental eddy current testing theory and its limitations, deep penetrating methods and, flaw analysis using Fracture Mechanics. These topics are summarized below in this order.

The eddy current theory given in this chapter introduced the skin depth equations to aid the understanding of the limitations of electromagnetic methods. The key points were:

- Eddy current material testing in general operates by inductive coupling (or mutual inductance) of an inductive coil brought close to a conductive material.
- The characteristic sensitivity of eddy current methods to planar defects is due to the obstruction of circulating eddy currents and the resulting distortion of the secondary magnetic field coupling with the detector.

- Optimisation of eddy current methods for the subsurface inspection of ferromagnetic materials is limited by the skin effect, such that saturation and low frequency methods are not sufficient for the reliable inspection of subsurface defects.

The second major topic was the review of deep penetrating eddy current methods. The problems associated with permeability were shown to be circumvented by the isolation of the detector from the immediate, directly coupling field of a separate (dedicated) exciter coil. This was achieved by distancing it either physically (referred to above as space isolation) or by recording transient field data over time (referred to in this thesis as space isolation and time isolation respectively).

- Space isolation allows remote field coupling between the exciter and the detector. The remotely detected field tends to achieve more even distribution of field lines within the test material, and allows the manipulation of the coupling path. These methods are called Remote Field Eddy Current (RFEC) methods.
- Pulsed Eddy Current (PEC) methods employ time isolation. This allows the time separation of deep and surface electromagnetic fields by measuring the decay of a pulsed magnetic field as it propagates below the material surface.

The RFEC method was found to be better suited to drill pipe inspection, mainly because it is equally sensitive to defects on the inside and outside surfaces of ferrous tubulars. The limitations were briefly discussed but were deemed within reasonable bounds of this project's aims. The final section on Fracture Mechanics explained the procedure for evaluating risk of fracture and the fatigue life of a structure containing fatigue cracks under cyclic loading. This section highlighted that the primary requirement of this project is to develop a system to accurately measure drill pipe fatigue crack depth.

This chapter has provided a general background of the state of eddy current methods with respect to this project's application. It also highlighted the major limitations of the eddy current method and provided justification for further development of the RFEC method. As this chapter provides only a superficial review of RFEC, a detailed review of the RFEC method is covered in the next chapter.

CHAPTER 3 REMOTE FIELD EDDY CURRENT METHOD

This chapter follows on from the previous chapter by investigating the RFEC method in more detail. Although initially a theoretical understanding of RFEC is given, the focus is to understand the practical implications of using the RFEC method for De Beers drill pipe inspection. It emerges that RFEC is possibly not ideally suited for the detection of low volume defects such as fatigue cracks; therefore the final section examines previous studies to determine the likelihood of fatigue crack detection by RFEC inspection.

The RFEC method was first patented by MacLean as a wall thickness measuring tool in 1946 [62], and later pioneered by Schmidt [63] with major contributions by Atherton [48]. The commercial use of RFEC dates back to the 1960's for the inspection of oil and gas wells [64]. Equal sensitivity to internal and external defects in ferromagnetic pipes and the general robustness of RFEC tools have led to an increasing number of industrial applications in recent years [65]. Currently RFEC is widely used for the inspection of heat exchangers and pressure tubes for corrosion and wear [66]. Although the remote field effect can test targets of various geometries, it is important to regard RFEC pipe geometry as distinct. This is because the pipe symmetry achieves isolation between the exciter and the detector (space isolation - Section 2.3) in a unique and highly effective manner[23], as explained in the next section.

3.1 The RFEC Effect in Ferromagnetic Pipe

Although RFEC testing is possible in non-ferromagnetic pipe, drill pipes used by De Beers are ferromagnetic. Therefore non-ferromagnetic RFEC will not be covered in this chapter. For more details, see the work of Lord [22] and Haugland [67].

The RFEC effect is achieved by aligning a solenoidal (exciter) coil coaxially and internally to the test pipe and distantly locating the detector near the inner pipe wall, as shown in Figure 3.1 [67]. In this configuration, two distinct coupling paths are formed, known as the direct and indirect coupling paths, shown in Figure 3.1. Detection of magnetic field directly from the exciter (i.e. via the direct coupling path) is undesirable as

[23] For this reason, RFEC is often thought to be exclusively a pipe inspection technique

this field does not permeate the pipe wall but propagates predominantly axially through the pipe interior [68]. Fortunately, axially travelling magnetic fields internal to the pipe tend to induce circumferential eddy current hoops in the pipe wall (Equation 2.3). This causes the rapid attenuation of the direct field due to energy dissipation by electrical resistive heating. This effectively prevents any line-of-sight coupling between the exciter and detector [68]. The result is that the signal present at the detector is primarily due to the field transmitted by an indirect energy flow path [69]. Transmission through this path is commonly described in the three stages shown in Figure 3.1:

(1) The magnetic field generated by the exciter coil diffuses radially through the pipe wall from the exciter to the outside wall of the pipe while being attenuated and phase lagged by eddy current principles.

(2) Once this field reaches the outer wall, it is able to propagate with relatively little attenuation or phase lag axially away from the source[24].

(3) The field diffuses back into the pipe interior while again being phase shifted and attenuated [69].

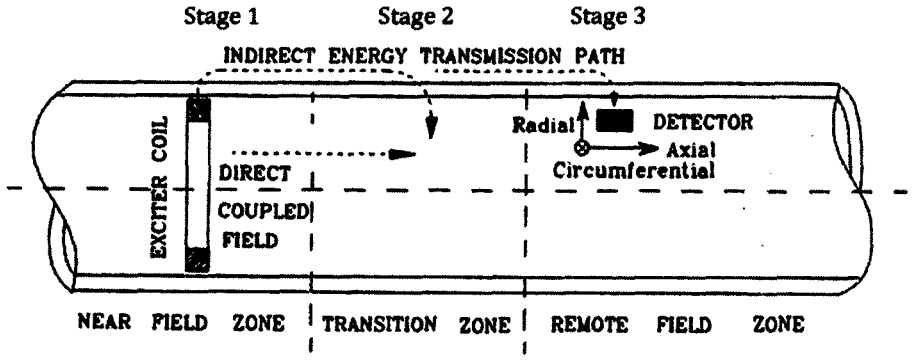

Figure 3.1 – Schematic of Remote Field Eddy Current testing (Atherton *et al.* [70])

The remote field zone of ferromagnetic tubes has considerably stronger field strengths outside the pipe than inside [48]. This causes the field to diffuse back into the pipe interior as if an encircling external exciter coil were activated above the detector in the

[24] This behaviour is similar to that of a TE_{01} waveguide well below its cut-off frequency [67].

remote field zone (Figure 3.2) – a result described by Atherton as the phantom exciter[25] effect [72]. This effect enables the inspection of the outer surface of drill pipes by an external 'phantom' exciter (Figure 3.2 – Stage 3).

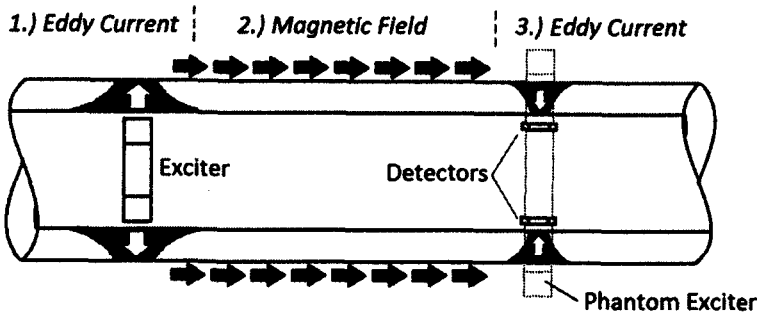

Figure 3.2 – Schematic showing eddy current and magnetic field dominated regions
Numbering corresponds to the remote field diffusion stages described above, arrows indicate magnetic field direction and shaded areas of the wall thickness indicate eddy current density (this figure was produced from descriptions by Atherton [52,72,73]).

Skin depth equations give high accuracy[26] in RFEC despite the plane wave assumptions of their formulation (Section 2.1). Derivation of phase and amplitude equations describing the remote field simply accounts for two through-wall transmissions: once at the exciter and once at the detector (eddy current dominated regions, Figure 3.2 – Stage 1 & 3) [74]. This gives the difference in phase between the exciter (φ_1) and the detector (φ_2) expressed in radians as

$$\varphi_2 - \varphi_1 = 2t\sqrt{\pi f \mu \sigma} \tag{3.1}$$

where t is the pipe wall thickness and σ is the electrical conductivity. Similarly, the amplitude, expressed as the ratio of the field amplitudes at the exciter (A_1) and the detector (A_2), is given as [23]

$$\frac{A_2}{A_1} = e^{-2t\sqrt{\pi f \mu \sigma}} \tag{3.2}$$

[25] This gives rise to an alternate method first developed by Mergelas and Atherton in 1993 for a computationally efficient means for testing the RFEC method (both experimentally and by computer simulation). Finite element simulations by Makar *et al.* show that the phantom exciter arrangement gives electromagnetic field distributions identical to the full remote field configuration [71].
[26] These errors tend to be small in RFEC testing provided that the pipe wall is thicker than 1 standard depth of penetration.

Note that change in phase is linearly proportional to wall thickness (Equation 3.1) while the corresponding change in amplitude is exponential (Equation 3.2).

Numerous practical implications arise from the use of the indirect coupling path for defect detection, particularly as this path contains distinct eddy current and magnetic field dominated regions (Figure 3.2) [75]. These implications are discussed in the next section.

3.2 Practical Aspects of RFEC Inspection

This section reviews the procedure for the setup of an RFEC probe and highlights certain considerations which are relevant to the drill pipe application. These considerations stem from abrasion of the pipe wall by the transported slurry, and the flanged interface between pipe sections. Other practical aspects include probe speed limitations and RFEC signal interpretation.

3.2.1 Setup of a RFEC Probe

Prior to inspection by RFEC, it is important to determine the axial distance at which the direct field has sufficiently attenuated that the remote field can be detected – the remote field zone [76]. This may be calculated with FEM simulations or determined experimentally with pullout tests [76]. Pullout tests entail locating the exciter and the detector in the test pipe and recording the detector signal while axially displacing the detector from the stationary exciter. Typical graphs of these results show the amplitude and phase of the detector signal (Figure 3.3) [77]. Notice that the near and remote field appear as a piecewise linear intersection when viewed on a log scale[27]. This marks the transition from the direct to the remote field dominated regions, a region called the transition zone. The remote field is also easily identified by the step-like change in the phase from the upper plateau of the near field to the lower plateau of the remote field.

The relatively constant phase characteristic of the near and remote field zones is useful to calibrate RFEC instruments (Equation 3.1) [74]. However, calibration using skin depth equations requires knowledge of the materials' electromagnetic properties. In particular, the magnetic permeability is needed and seldom available due to high permeability

[27] Sometimes a sharp 'dip' is observed at this intersection. This occurs when the near and remote field amplitudes are of equal amplitude and opposite phase causing the field components to cancel [48].

variations. As a result, magnetic permeability often requires direct measurement from the pipe material [76].

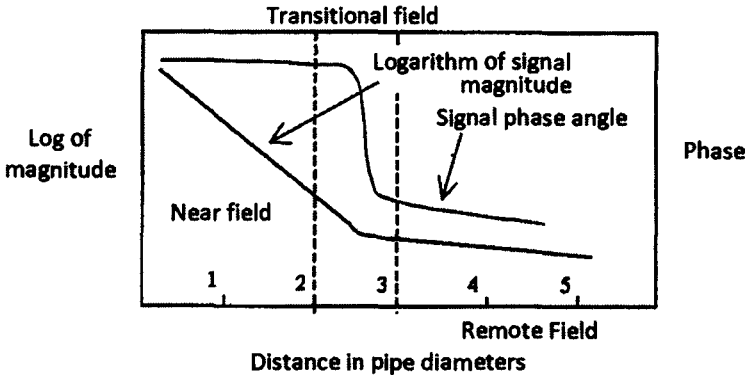

Figure 3.3 – Remote field eddy current signal magnitude and phase (from Ref. [77])

As the transition zone is typically found between 2 and 3 pipe diameters from the exciter coil (Figure 3.3), RFEC tools are generally longer than 2 pipe diameters [44]. Although it is impossible to eliminate all traces of the direct field, little improvement is gained at greater distances [78]. These geometry implications are discussed further in the next section.

3.2.2 Drill Pipe Geometry Considerations

As previously mentioned, the walls of the De Beers marine drill pipes are gradually abraded from the inside by the transported sediment from the seabed. As a result, although the pipe OD remains constant throughout the service life of each pipe section, significant differences in wall thickness (and minor differences in the effective[28] diameter) exist between old and new pipe sections[29].

NDT probe design requires understanding of the tolerances for mechanical movement with respect to the target material. For this purpose, the terms probe lift-off and wobble are defined. Lift-off is used in NDT to describe variations in the distance between the sensor and the test surface (Figure 3.4) [44]. Wobble describes all non-axial movement of

[28] In this case 'effective' is taken to mean the average of the pipe OD and the ID values.
[29] Worn pipes are located away from high stress areas of the drill string on reassembly to improve the operational lifespan of individual pipe sections.

the probe (resulting in lift-off). RFEC is largely immune to lift-off both at the exciter and the detector[30] unlike magnetic flux leakage and conventional eddy current methods which generally require compensating sensor support systems to ensure a constant lift-off distance [65]. Furthermore, the probe fill-factor - defined as the ratio between the exciter coil and pipe bore areas (Figure 3.4) - may be as low as 70% [44]. Therefore wall thickness variations are unlikely to significantly affect inspection results.

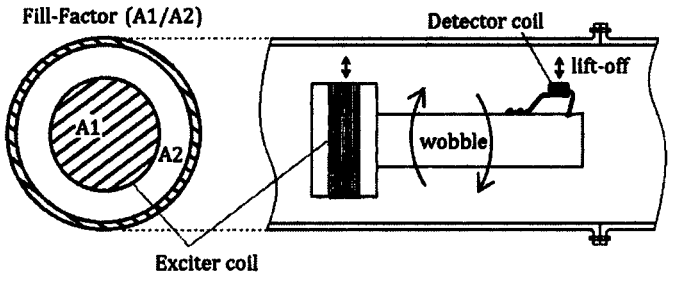

Figure 3.4 – Fill-factor (A1/A2) and lift-off effects

The drill pipe diameter is significantly larger than is typically tested by RFEC. However, large diameter RFEC tools are commercially available[31] and have been shown to be capable of testing pipes with diameters of up to 2m (Figure 3.5) [65].

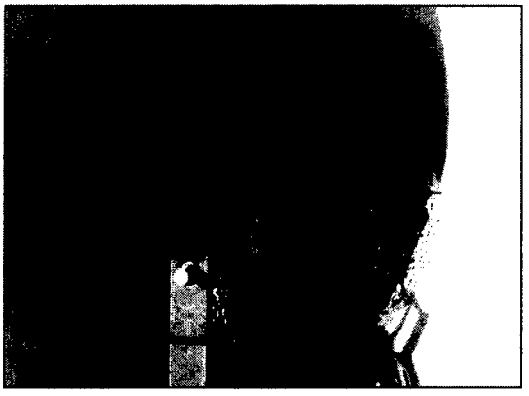

Figure 3.5 – 1981mm diameter cement-lined steel pipeline with detector section of RFT tool (from Russell NDE Systems Inc. [65])

[30] Lift-off measurements of up to 38mm lift-off from a deep water-well casing tools from inspections by Russell NDT, Canada [65], are reported.

[31] Non-commercial methods developed by Atherton are able to test diameters of approximately 3.6m [79].

the probe (resulting in lift-off). RFEC is largely immune to lift-off both at the exciter and the detector[30] unlike magnetic flux leakage and conventional eddy current methods which generally require compensating sensor support systems to ensure a constant lift-off distance [65]. Furthermore, the probe fill-factor - defined as the ratio between the exciter coil and pipe bore areas (Figure 3.4) - may be as low as 70% [44]. Therefore wall thickness variations are unlikely to significantly affect inspection results.

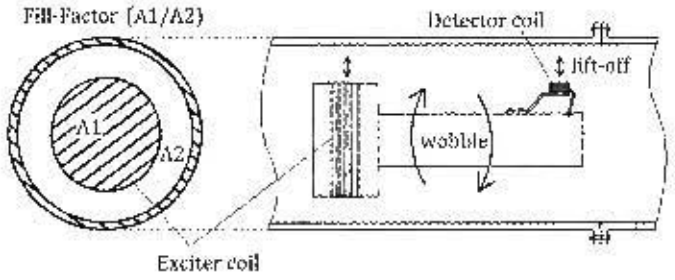

Figure 3.4 – Fill-factor (A1/A2) and lift-off effects

The drill pipe diameter is significantly larger than is typically tested by RFEC. However, large diameter RFEC tools are commercially available[31] and have been shown to be capable of testing pipes with diameters of up to 2m (Figure 3.5) [65].

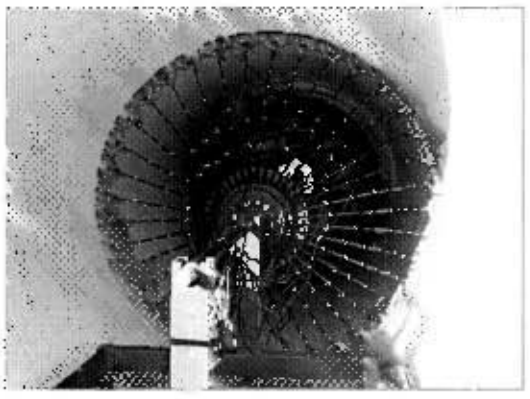

Figure 3.5 1981mm diameter cement-lined steel pipeline with detector section of RFT tool (from Russell NDE Systems Inc. [65])

[30] Lift-off measurements of up to 38mm lift-off from a deep water-well casing tools from inspections by Russell NDT, Canada [65], are reported.

[31] Non-commercial methods developed by Atherton are able to test diameters of approximately 3.6m [79].

Although the RFEC method is robust to continuous thinning, the method is strongly affected by external metal contiguous with the pipe wall. These effects are likely to occur at the flanged interface between drill pipe sections as explained below[32].

The gradual attenuation of the remote field, which enables detection at the detector, is dependent on thin walled pipe proportions [81]. External contiguous metal such as a flange is effectively seen by the remote field as a momentary drastic increase in wall thickness allowing circulating eddy currents to attenuate the remote field [80]. For this reason drill pipe flanges significantly attenuate the external energy flow path between the exciter and the detector. Due to limitations in detector sensitivity, this often results in a 'dead-zone' in which flaw detection is not possible (Figure 3.6 - a) [80]. The double detector configuration (Figure 3.6 - b) achieves inspection of the entire pipe section, provided the overall probe length is less than that of a single pipe section (10m) [44].

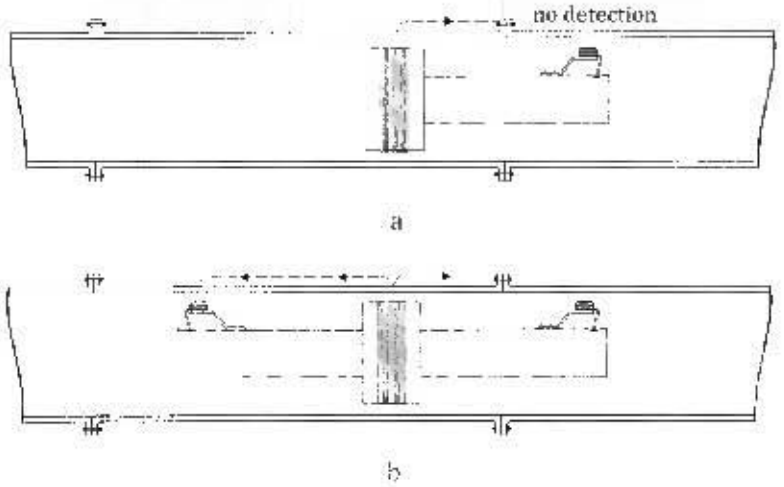

Figure 3.6 – RFEC effects in flanged pipe
Hatched regions show areas blind to conventional RFEC configurations (a), the double detector configuration achieves full pipe detection – a possible solution (b)

3.2.3 Speed Limitations

High running costs of the mining operation places a time constraint of approximately 5 hours to inspect the drill pipe [5]. This is important because low velocities are needed to

[32] This problem also occurs frequently with the RFEC inspection of heat exchanger tubes with support plates [80].

ensure signal quality[33]. Each observation (data point on an RFEC trace) is generated by the amplitude and phase characteristics of the detected signal relative to a reference signal. This process (demodulation) usually requires several cycles of the detector signal to be effective [44]. Therefore the time per demodulation (time constant) must be increased at low frequencies to ensure that sufficient cycles are included for each amplitude and phase measurement. This is the case with RFEC as low frequencies are required to improve the strength of the remote field for detection. Consequently higher RFEC probe speeds are permissible by increasing the frequency of the exciter current [34]. However, there is a limit to the amount that frequency may be increased as this also exponentially decreases the remote field amplitude as a result of the skin effect (Equation 3.2). Therefore for a particular probe-pipe combination an optimal frequency exists, as illustrated in Figure 3.7.

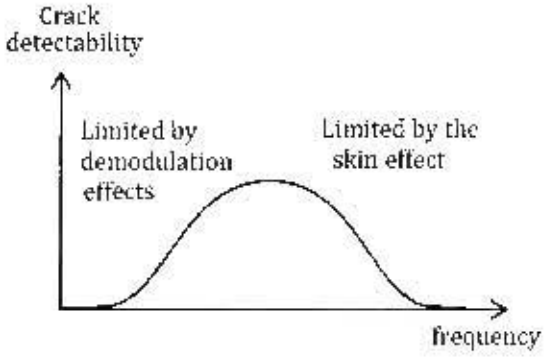

Figure 3.7 – Schematic representation of the trade-offs between the detrimental effects of low and high frequency. Note that frequency is proportional to the maximum scanning speed possible and therefore, in general, probe speed is closely associated with frequency.

Due to the strong association of drive frequency with permissible probe speed, conventional eddy current methods to alleviate the skin effects are often applied to RFEC probes, particularly methods involving saturation [23,34,80,84]. These results are discussed in Appendix A-1: Magnetic Saturation for RFEC Inspection and in the final discussion, Section 7.1.2.

[33] Low velocities are also required to allow remnant magnetic fields to disperse; these tend to produce spurious signals [82].

3.2.4 Signal Interpretation

Although RFEC defect signals are easily characterised on a voltage polar plot display, inline inspections generally make use of strip charts to illustrate test results. Strip charts typically have two axes: the detected signal and the axial displacement of the detector. As the detector signal is deconstructed in terms of amplitude and phase, two plots are produced for each inspection result (trace). This study makes uses strip charts to represent RFEC amplitude and phase signals similar to see Figures 3.8 and 3.9)[34].

As defects are detectable anywhere in the indirect transmission of the remote magnetic field, special systems are often required to identify the true location of a defect [75]. Schmidt demonstrated that defect signatures from internal and external defects of the same physical dimensions tend to give similar amplitude and phase indications (Figure 3.8) [82].

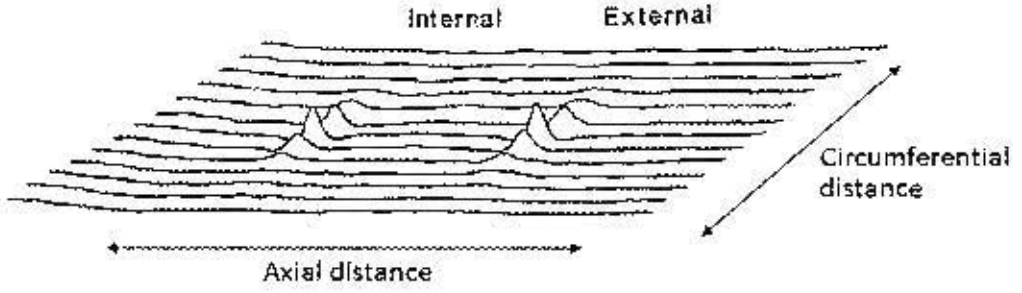

Figure 3.8 - Internal-external pit sensitivity (Schmidt [82])
Results are from two equal (50% penetration), 9.5mm depth, ball milled holes, 76mm diameter steel pipe, 7.6mm wall thickness, at an exciter frequency of 40Hz.

Although small differences between internal and external defects were observed by Atherton[35], these are generally regarded as hard to distinguish [82]. This is highly relevant in the drill pipe application as fatigue cracks are known to propagate from the outside and must be distinguishable from the extensive corrosive and abrasive pitting on the internal surface side [5]. The axial location of the defect is often also ambiguous as

[34] Although the polar plot requires minimal processing and is useful for characterising defect responses (discussed by Atherton [70]).

[35] External defect indications are described by Atherton to exhibit amplitude attenuation and width expansion due to spreading of the field lines from the external pipe surface through the pipe wall [52].

certain defects generate responses both at the exciter and the detector [75]. Figure 3.9 shows strip chart phase recordings for detector displacement. Notice that a single inhomogeneity (in this case a weld) creates two defect indications from a single pass: once at the detector and once at the exciter.

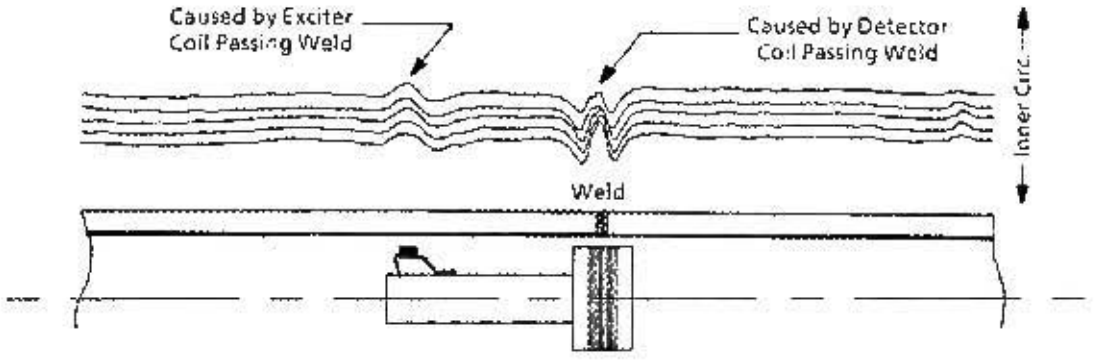

Figure 3.9 – Multiple RFEC traces off a circumferential weld (Schmidt [82])
Exciter signals appearing downstream from detector signals, in its current position the probe signal is due to interaction at the exciter coil.

3.2.5 Discussion

The above evidence covers a variety of RFEC effects relating to various drill pipe morphologies. Due to the high lift-off and low fill-factors achievable by RFEC, these probes may be built smaller than the pipe internal diameter and with "suspension", allowing the inspection of pipes with minor constrictions, large radius elbows, and pipes with scale and inner linings (Figure 3.10) [76]. This evidence strongly suggests that the RFEC method can tolerate drill pipe diameter variations caused by wall thinning and axial misalignment between the probe and the pipe.

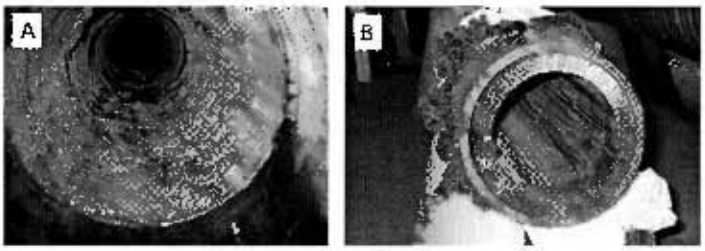

Figure 3.10 – Internal scale (A) and inner lining (B) in cast iron water pipe, both successfully tested by RFEC (Russelltech NDE [65])

However, as previously mentioned, high operational costs limit the amount of downtime permitted for inspections. A possible solution would be to insert the RFEC probe with the flow of sediment. Although the method is already shown to be tolerant to mechanical interferences (possibly due to the stream of sediment), this approach is likely to be limited by the relative motion of the pipe wall to the detector caused by drill pipe rotation and the probe's inspection speed. This is considered outside the scope of this study. However, as speed variations are shown to affect the quality of the data, it is considered important that probe speed remain sufficiently slow and constant to ensure this quality is uniform for the generation of results in this thesis. Thus a constant speed pull-rig is required.

The difficulty in differentiating between internal and external defects is highly relevant as the relatively sparse distribution of external fatigue cracks must be clearly distinguishable from internal scores and pitting. Existing RFEC tools solve this problem by also inspecting the inside surface with conventional eddy current detection and using this data in post processing to eliminate internal defect data [52]. This approach may prove to be redundant as pipe history is likely to be available due the repeated testing required to monitor fatigue crack progress (Section 2.5). The identification of 'non-progressing' defects may be possible by comparison of defect data with inspection history. Therefore before final testing can take place, and after the RFEC probe is built, a pilot study is required to test the usefulness of RFEC inspection history.

Thus far, a theoretical and practical background is given on RFEC inspection. However, little work has been done on the detectability of circumferential fatigue cracks using RFEC inspection. Therefore the sensitivity of RFEC inspection systems to fatigue defects is examined in the next section.

3.3 Defect Detectability

As discussed above, fatigue cracks are likely to be difficult to differentiate from the mechanical damage present on the inside surface of the drill pipe. Apart from the difficulty when distinguishing external fatigue cracks from internal pitting, RFEC also typically achieves significantly reduced sensitivity to low volume defects [82].

Figure 3.11 - a shows that as defect volume decreases, so does the RFEC signal. This suggests that tight fatigue cracks are likely to be undetectable by RFEC methods. However, the figure also shows results for axially and circumferentially aligned slits which are also low volume (0.25mm width; Figure 3.11 – b). This shows a an important phenomenon of RFEC inspection in ferromagnetic pipes, that is that circumferentially oriented defects give significantly stronger defect signals than axially oriented defects of the same volume (Figure 3.11 – b). This is generally attributed to strong interaction of the axial magnetic field with the relatively large perpendicular area of a circumferentially oriented flaw in a ferromagnetic pipe [48].

The question therefore arises: if RFEC defect sensitivity diminishes as defect volume becomes small (Figure 3.11 - a), is the improved sensitivity to circumferential slits (Figure 3.11 – b) sufficient to ensure the reliable detection of drill pipe fatigue cracks?

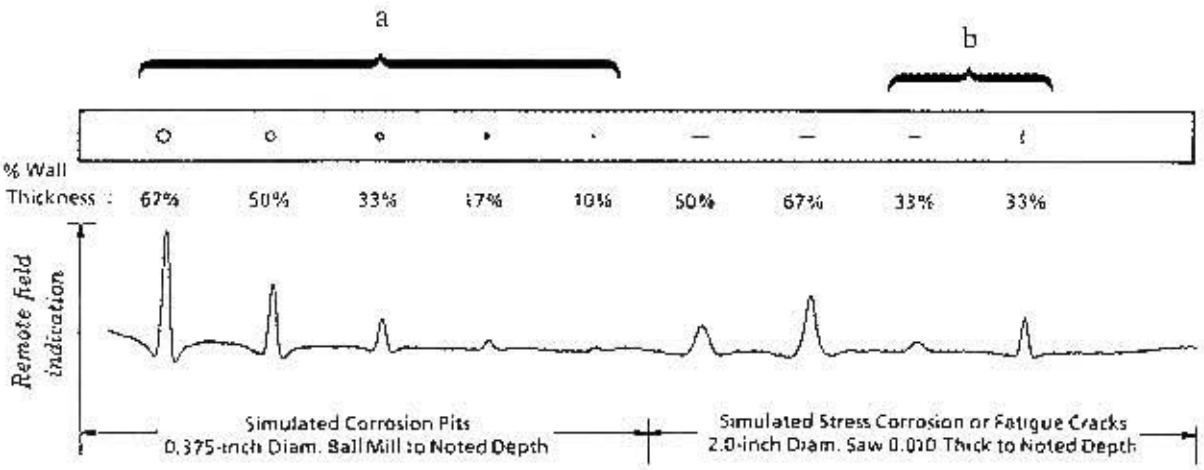

Figure 3.11 – Single detector trace of simulated external flaws in steel pipe (modified from Schmidt [82])
Note that circumferential and axial slit widths are equal to the diameter of the smallest ball milled hole, data omitted for clarity can be viewed on the original figure in [82].

To answer this question, theories and case studies were examined. The improved sensitivity to circumferential defects is explained by Atherton with the missing magnetization model [54,81]. This describes the magnetic field interaction as similar to the magnetic reluctance produced by an air-gap in a high permeability magnetic circuit [81] (for a further explanation of the anomalous source models, see Appendix A-2). These studies use finite element simulations of circumferential slits in ferromagnetic

material to show that the magnetic field perturbations (and therefore defect detectability) become vanishingly small as defect width tends to zero [54,81]. This suggests that circumferentially oriented fatigue cracks are not easily detected using the RFEC method.

3.3.1 Evidence of Circumferential Fatigue Crack Detectability

Despite these predictions, results from commercial inspections performed by Russelltech NDE find that circumferential thermal fatigue cracks are detectable with standard RFEC tools (Figure 3.12) [84]. For correspondence see Appendix B - 1.

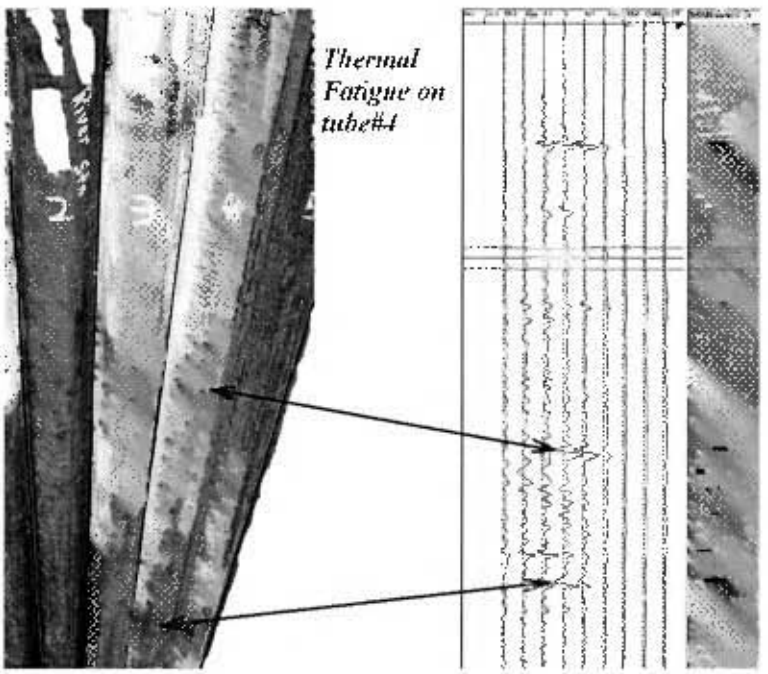

Figure 3.12 – Thermal, circumferentially oriented, fatigue cracking (Russelltech [84])
Scan was taken using an external RFEC (E-PIT) probe on tube #4. The probe array contains 9 detector coils positioned across the flame side of the tube; these signals are shown on the right. The vertical axis of the strip charts represents distance and the horizontal axis represents amplitude.

Earlier finite element simulations by Atherton found that although field perturbations reduce with defect width and are likely to vanish in the limit; unusually high field perturbations are achieved by even very fine defects in ferromagnetic material (Figure 3.13 – steel), [50,85].

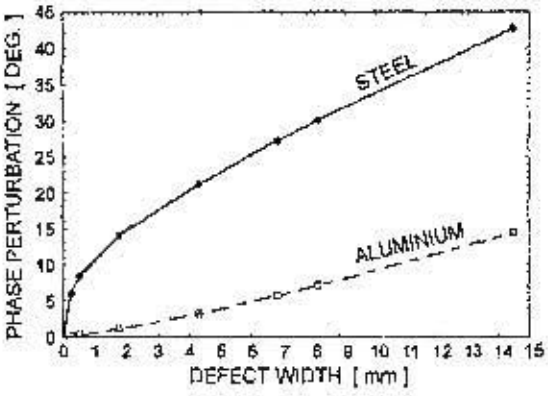

Figure 3.13 – Simulated phase perturbation induced by an interior slit defects as a function of slit width (Atherton [72])

These studies suggest that this is due to 'funnelling' of the magnetic field into the crack opening (Figure 3.14 – a) [50]. These simulations also show that decreasing slit width results in a rapid increase in magnetic field density a small distance below the surface of the emerging crack (Figure 3.14 – b).

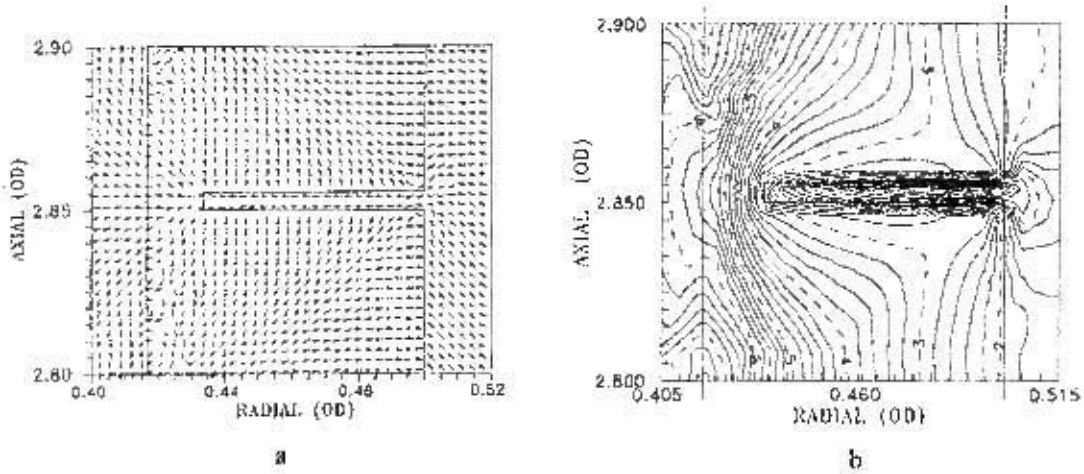

Figure 3.14 – Map of magnetic poynting vector directions (a) and corresponding field amplitudes (log(Wb/in)) in the vicinity of an 80% deep 6.7% wide far side slit (b) by Atherton and Czura [50]

3.3.2 Discussion of the Detectability of Fatigue Cracks with RFEC

The evidence above suggests that, despite predictions from the anomalous magnetic source models, circumferential defects are still detectable. Although anomalous models do not explain this result explicitly, earlier work by Atherton demonstrates that significant magnetic field perturbations are achieved by even very narrow slits. Correspondence with

Atherton indicated that further experimental results were necessary to determine the detectability of circumferential fatigue cracks by RFEC, and that such experiments had not taken place due to difficulty in generating fatigue cracks in pipes (Appendix B - 2) [55].

As narrow defects in ferromagnetic material are able to create large magnetic field perturbations, it is important to note that such perturbations are not necessarily due to missing material, but could also be due to inconsistencies in the materials' electromagnetic properties, particularly magnetic permeability[36] [81]. As permeability variations are known to occur on the fatigue crack faces due to cold working [32,86–88], it is possible that the effective crack width – again defined in terms of permeability rather than missing material – may be larger than expected[37]. This is a possible explanation for the positive test results shown in Figure 3.12. In line with the above reasoning, it is important to recall that small amounts of plastic deformation have been observed in later stage drill pipe fatigue cracks (Section 2.4). As even a slight increase has been shown to exponentially increase the magnetic field interaction, strong defect signals are likely to occur from drill pipe fatigue cracks if plastic crack opening occurs.

3.4 Summary

This chapter follows on from the brief overview of RFEC in the previous chapter with a more detailed examination of the method.

The particular effectiveness of pipe geometry RFEC inspection is explained by the rapid attenuation of the direct coupling field relative to the remote field. Mathematical derivation of amplitude and phase relationships showed that the RFEC inspection emulates inspection of the external pipe surface with classical eddy current methods (a large area 'phantom' exciter) and an internal detector.

Practical aspects of RFEC inspection showed that, although RFEC probes are generally limited to low inspection speeds, the method is tolerant to lift-off of its detectors and the

[36] Note that discontinuities in conductivity are discounted as fatigue cracks are circumferentially oriented, full justification is covered in Appendix A-2.

[37] Certain methods have been developed which monitor the progression of fatigue damage by only measuring the magnetic properties of the material (called hysteresis tracking) [32]. Although these methods are not recommended for local damage monitoring[37], they provide further evidence that fatigue cracks engender permeability variations.

exciter from the inner pipe wall. This is expected to reduce the effects drill pipe diameter variations due to wall thinning.

It was also shown that defect signals often require special interpretation, namely: two indications may appear from a single defect (i.e. detected at the exciter and the detector), and internal and external defects result in similar defect signals. These were discussed, but also identified as secondary to concerns regarding the overall poor response of RFEC methods to low volume defects.

A study of the detectability of low volume defects shows that although detectability does decrease with defect volume, circumferential defects in ferromagnetic material tend result in particularly strong signals. Results from Russelltech NDE show that circumferential fatigue cracks were detectable by conventional RFEC tools. Earlier work by Atherton showed that high field perturbations are possible from even very fine slits. It was therefore speculated that permeability changes due to cold working of the fatigue crack faces - leading to wider effective fatigue crack widths in terms of magnetic permeability - might be cause for these positive results. It was discussed that, due to observed plastic opening in mature drill pipe fatigue cracks, defect width concerns are secondary to the overall detectability of circumferential defects in general.

The next chapter details the design of the RFEC inspection system used to produce results in this thesis, and draws on the practical aspects discussed in this chapter. It is helpful to recall that a pilot study was recommended to determine the usefulness of inspection history for the identification of 'progressing' vs. 'non-progressing' defects (Section 3.2.5), this is performed separately in Chapter 5.

CHAPTER 4 DESIGN OF THE RFEC TESTING RIG

4.1 Introduction

4.1.1 Overview

The previous chapter motivated for the RFEC method as suitable for the inspection of the De Beers drill string. This was mainly due to its equal sensitivity to internal and external defects and high sensitivity to circumferential defects in ferromagnetic pipe [48]. Therefore this chapter details the design and building of the RFEC probe and supporting structure. The supporting structure included a data acquisition system and a pull-rig.

A defect fabrication section was also included. This was because of the special requirements of the defects tested (narrow, thumbnail shaped and accurate depth control to simulate fatigue crack progression). Therefore the requirements of this chapter are:

- An RFEC probe with on-board H-field detection and signal amplification circuitry
- A pull-rig to control the travel and circumferential orientation of the RFEC probe
- Facilities to fabricate narrow, circumferential defects of different shapes
- A test pipe that is representative of the drill pipe.

4.1.2 Test Pipe Assumptions

Prior to the design of an RFEC probe, it is important to examine the specifications of the pipe to be tested. Due to the lack of availability of drill pipe (500mm ID, 15mm wall thickness, 150m length), a scaled down pipe (81mm ID, 4mm wall thickness, 2100mm length) was used for this study. The relevant differences between the drill pipe and the test pipe available in this project and are listed below:

- Electromagnetic properties (different metal)
- Heat treatment
- Diameter, wall thickness and pipe aspect ratio
- The test pipe is not sectioned with flanges and did not contain significant pitting or rust on the interior surface
- Manufacturing processes (and heat treatments) are unknown

It was assumed that the scaled down pipe was sufficiently representative and therefore the errors can be accounted for by calibration in the drill pipe implementation (discussed in Section 7.1). The RFEC probe was designed and built on these assumptions.

4.2 Design of the RFEC probe

As described in the previous chapter, an RFEC probe in its simplest implementation is comprised of an AC-field generating exciter coil and a remote detector coil. This is the configuration required to permit the use of skin depth Equations 3.1 and 3.2 to cross-check the results for amplitude and phase in the remote field zone. Therefore probe designs incorporating structures to alter these field distributions were avoided [74,89,90]. Instead, the emphasis was on producing standard RFEC field distributions similar to the probe designed by Teitsma [76]. Note that Teitsma's probe design substituted nylon for metallic parts between the exciter and the detector (Figure 4.1).

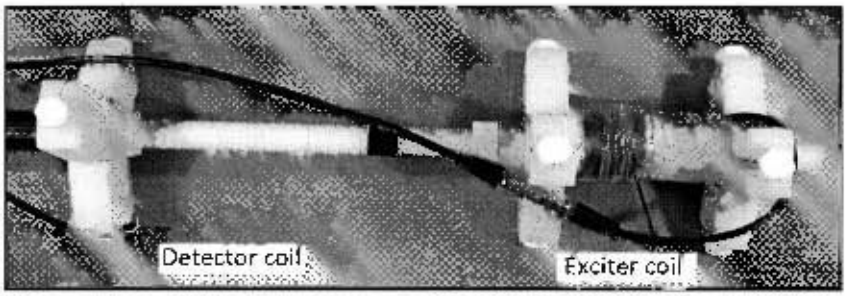

Figure 4.1 RFEC probe showing the exciter coil, the axially aligned detector coil and nylon probe structure (Teitsma [76])

Therefore the probe built for this thesis used inter-fitting PVC pipes for the supporting structure. This was considered an improvement as the higher rigidity achieved by a cylindrical shape is less prone to mechanical vibrations.

The exciter detector distance was required to be variable to determine the location of the remote field zone. Therefore an adjustable tight fitting PVC cuff was used to connect the exciter to the probe. Supports for the probe were constructed from two sets of nylon bolts threaded radially into the PVC pipe wall. These supports could be adjusted to centre the probe in pipe diameters between 75mm and 105mm, and could be set with nylon locknuts. The heads of the bolts were wrapped in low friction (PTFE) cloth to reduce

sliding resistance. The on-board pre-amplifier and electrical connections were fixed to the inside of the PVC probe structure. Figure 4.2 shows a picture of the completed probe.

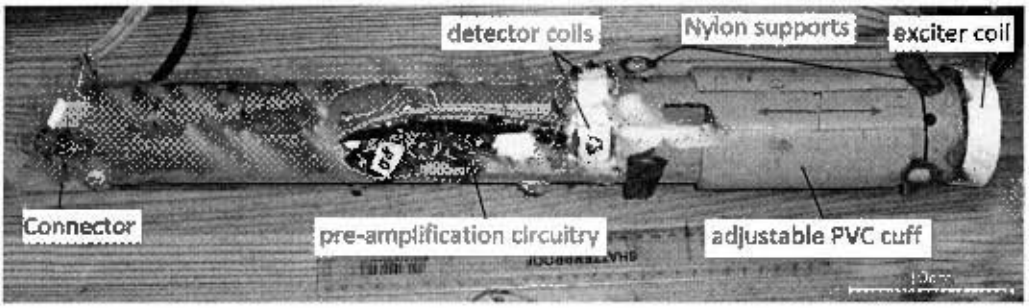

Figure 4.2 – The RFEC probe layout

The following paragraphs detail the design and building of the onboard electrical system to detect the remote II-field and amplify the resulting detector signal (shown schematically in Figure 4.3).

The exciter coil was wound from 1mm thick copper wire (700 turns). Two detector coils were constructed to enable differential mode capabilities, and were wound from 0.35mm copper wire and (900 turns) onto laminated ferrite cores[38] to improve sensitivity (cross-sectional area 25mm^2, 10mm height) [76]. These were balanced with a UNI-T (UT600) hand held impedance meter. To ensure that equal signals were measured at both coils, they were placed equidistant to the exciter coil. All coils were wound on bobbins with a transformer winder and set in epoxy to hold the shape and to protect the wires from abrasive contact with the pipe wall. Note that the detector coils were aligned radially unlike the design by Teitsma[39] (axially aligned – see Figure 4.1). This was to achieve maximum interaction with the predominantly radial incident remote field, as documented by Atherton's measurements of unsaturated ferromagnetic pipe close to the inside pipe wall [52].

The a typical RFEC activation frequency was chosen - 80Hz [44], note that 50Hz was avoided to reduce mains interference. The voltage generated by a loaded detector coil in the remote field zone is generally in the range of 1 to 10uV [44]. Therefore, an AD620

[38] The cores were constructed from e-core transformers.

[39] The aim of Teitsma's probe design was to determine the effects of significant lift-off on defect detectability. It was presumed that the detector in this design was axially aligned to intercept the magnetic field, which becomes gradually more axial close to the centre of the inside of the pipe.

precision amplifier was chosen due to its high common mode rejection ratio (CMRR) of 100dB, low noise of 72n nV/√Hz and gain of 10^4. It is worth mentioning that significant isolation from environmental noise was achieved by mounting the sensitive pre-amplification circuitry within the remote field zone but past the detectors (from the exciter) [44]. Nonetheless, care was taken to avoid large loop areas in the construction of the pre-amplification circuit (design used twisted pairs and compact layout). For the RFEC probe circuit diagram, see Appendix C-1.

The reference signal required for demodulation (Section 2.2) was defined as the voltage measured across a 10Ω resistor placed in series with the exciter coil. This provided measurements of the driving current that is directly proportional to the H-field (Equation 2.2). A Ling (PA 100) oscillator and frequency generator supplied the drive signal and acted as a current source for the exciter coil. Both the reference signal and detector waveforms were displayed in real-time on an Agilent Oscilloscope (DSO1002A) and DC power for the sensitive circuitry was provided by a Kenwood Regulated DC power supply (PW 18-2). To permit probe travel of 3m away from the apparatus bank, 5m shielded cables were required. The parasitic impedance effects were removed with capacitive decoupling of the lines at the supply and the probe, and the supply current was regulated with chokes placed in series with the DC power rails. It was found that for the elimination of environmental noise, it was essential to short the data cable shielding to the pipe wall and ground both. This noise was expected to be due to the large area loop formed by the data cables, interacting with the magnetic fields produced by the AC pull-rig motor. The schematic is shown in Figure 4.3. For the full circuit diagram, see Appendix C-1.

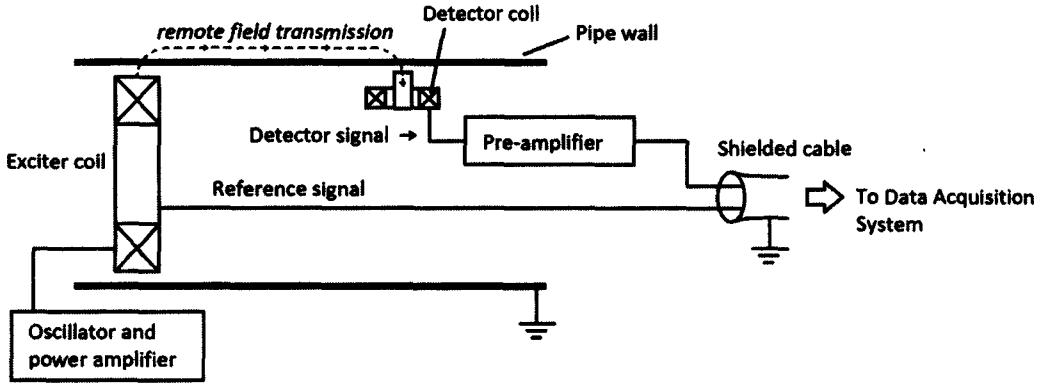

Figure 4.3 – Electrical schematic of the RFEC probe

4.3 Data Acquisition System

Traditionally, eddy current NDT data pre-processed by an analogue demodulation stage. However, demodulation may be implemented effectively and with additional flexibility by software combined with high-speed digital sampling. For latter, a 10kSa/s, 12bit analogue to digital converter (ADC) from National Instruments $_{tm}$ (model: NI-6008) was used. Three data channels were required to record: the reference waveform, the detector waveform and the axial position of the detector (note that the circumferential position of the detector is set manually and therefore does not require an input - both circumferential and axial position systems and mechanisms are discussed in Section 4.5). Sampling three channels divided the sampling rate down to 3333S/s. This was sufficient to fully determine these waveforms as RFEC typically operates at less than 100Hz, a frequency that is well below the Nyquist rate[40] [34]. To prevent aliasing from high frequency content, passive low-pass filters with cut-off frequencies of 160Hz were placed in series with the ADC inputs[41]. The converted digital data was imported to Matlab using an NI Device Monitor (v1.8) via USB. For Matlab code, see Appendix D-1.

The demodulation was carried out in Matlab using the discrete Fast Fourier Transform[42] (FFT) function. This was able to provide a real-time display at less than 50ms per demodulation with 8333 observations[43].

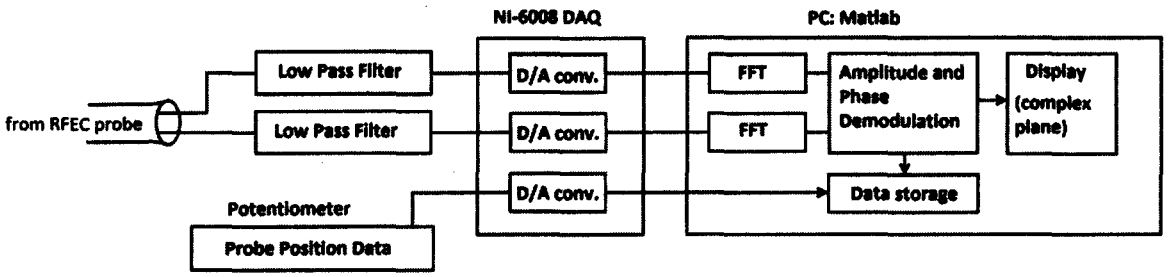

Figure 4.4 – Data acquisition schematic

Typical FFTs of the reference and detector signals are shown in Figure 4.5. The frequency associated with the reference signal peak was extracted and used as a reference to filter and demodulate the detector signal, as explained below.

[40] See the Nyquist–Shannon sampling theorem [91].
[41] Although these are inefficient compared to active filters, the impedance values could be low. Power dissipation across these filters was also low as the input impedance to the ADC was high (144k)
[42] The Fourier transform decomposes a waveform into a sum of its constituent sinusoidal frequencies.
[43] The FFT function operates at a 10th of this speed but the overall process is slowed by the supporting code.

As the Fourier transform returns the complex number representing the signal amplitude and phase, the relative amplitude and phase between detected and reference signals may be attained by complex division of the detector and reference peak values (Figure 4.5). For Matlab code, see Appendix D-2.

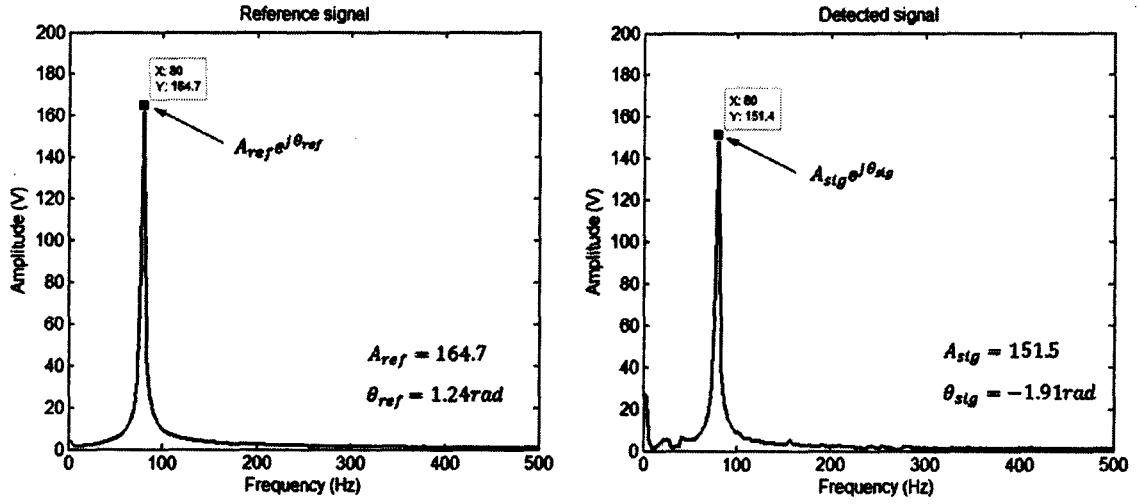

Figure 4.5 – Representation of reference and detector signals in the frequency domain

Note the additional noise present in the detector signal. The demodulation described above filters the noise by targeting only the reference frequency, in this way the system also behaves as a band-pass filter.

Put in Maths, let

$$V_{ref}(\omega_0) = A_{ref}e^{j\theta_{ref}}$$

$$V_{sig}(\omega_0) = A_{sig}e^{j\theta_{sig}}$$

$$\therefore \frac{V_{sig}}{V_{ref}} = \frac{A_{sig}e^{j\theta_{sig}}}{A_{ref}e^{j\theta_{ref}}} = \frac{A_{sig}}{A_{ref}}\, e^{j(\theta_{sig}-\theta_{ref})}$$

$$\left|\frac{V_{sig}}{V_{ref}}\right| = \left|\frac{A_{sig}}{A_{ref}}\right| \left|e^{j(\theta_{sig}-\theta_{ref})}\right| = \frac{A_{sig}}{A_{ref}}$$

The values in the Figure correspond to $-1.69dB$[44] *at a phase lag of* $141.9°$

[44] For details on Fourier Theory, see Hoffman [92].

4.4 Calibration and Optimisation

4.4.1 RFEC Probe Calibration

Before RFEC inspection could take place, it was first necessary to determine the location of the remote field zone, and thus the exciter detector distance. The amplitude and phase of the H-field inside the pipe was measured with the detector as it was axially displaced from the exciter coil, as detailed in Section 3.2.1, and plotted in Figure 4.6. These results closely resembled those shown in the literature (Figure 3.3). Note the transition field zone at approximately 2 pipe diameters (dotted line) as discussed by Haugland [67]. As a compromise between contamination from the near field and weak field strengths in the remote field, an exciter detector distance of 219mm was chosen (2.7 pipe diameters).

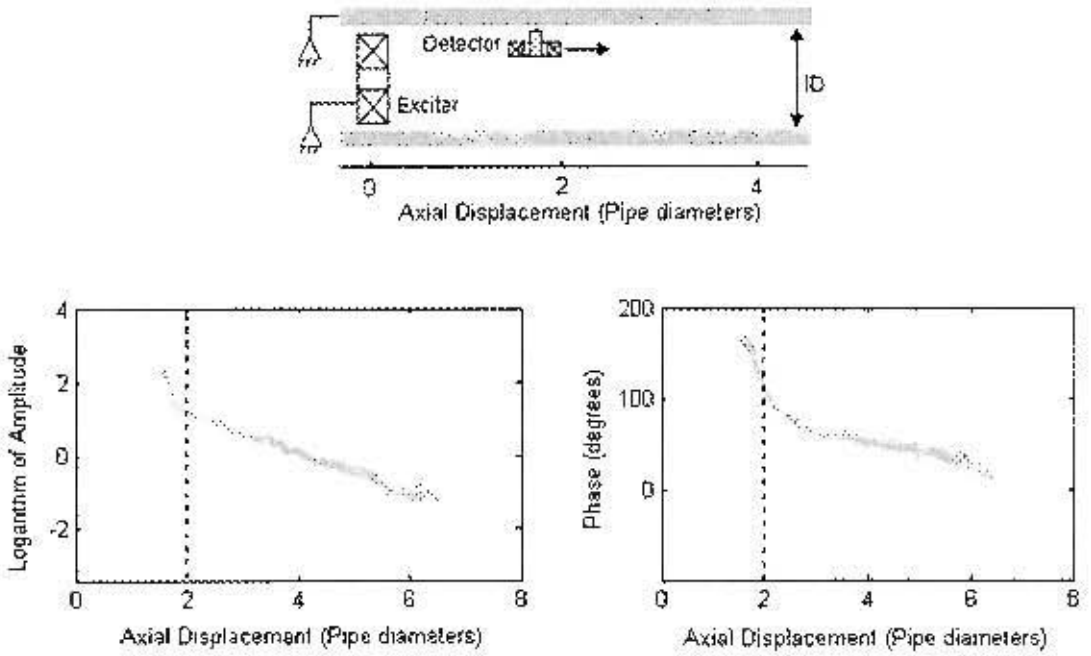

Figure 4.6 – Field strength from pullout tests
The remote field zone (right of the dotted line) for thickness (t) of 4mm pipe corresponds to Figure 3.3. Note that the phase lag occurs at 12° per mm.

4.4.2 Optimisation of Data Acquisition and Post-Processing Systems

Originally, the method developed for this project allowed real-time viewing of the data as outlined at the beginning of this chapter. However, this meant that the ADC was only sampling the waveforms for a small fraction of the total amount of time to extract a single amplitude and phase data point (Figure 4.7). This was caused by Matlab's handshaking, demodulation, and storage processing times. Therefore a significant improvement to the quality of the test results was to run the ADC continuously during testing (foregoing real-time display), and processing the stored waveforms and position data separately after each inspection.

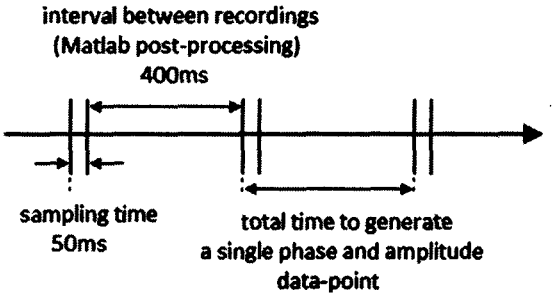

Figure 4.7 – Sampling and processing time allocations
Note that by continuous sampling; 8 times more waveform data could be stored

The DC component of the detector and reference waveforms was removed prior to performing each FFT to reduce the numerical error. The FFT of a truncated sine wave (finite length recording) is a sinc function (sin(x)/x) centred on the frequency ω_0. The main lobe width of this function (known as the frequency resolution) is inversely proportional to the time spent recording and the aim is the extract the peak of the sinc function. Zero-padding in the time domain prior to transforming to the frequency domain results in a more finely sampled Fourier transform. Hence the peak could be more accurately extracted by padding each set of sampled data with zeros (length 10 times the number of samples). Incorporating these modifications, the RFEC system was able to process five amplitude and phase measurements per 4 seconds of data capture (or 1.25 demodulations per second). Note that the processing stage was done offline (to reduce latency discussed above) but could also be implemented in real-time.

The following section describes the supporting structure required to propel the RFEC probe through the test pipe. Note that the demodulation rate defined in the previous

section is instrumental in determining the maximum allowable probe speed. This is calculated in the following section.

4.5 Experimental Design

This section describes the design and implementation of the RFEC probe's test rig. This included a pull-rig to draw the RFEC probe through the test pipe at constant velocity and a position sensing system to determine the detector position. It is a requirement that the defects tested in this thesis are as narrow as possible to be similar to fatigue cracks, for this purpose specialised defect machining equipment was built. These details are covered in the final section (defect fabrication).

4.5.1 Testing Rig

The testing rig was designed to house the test pipe, propel the RFEC probe, and feedback axial position data. As the field external to the pipe is stronger than the internal field in the remote field zone (Section 3.1), it was considered important to ensure no metal parts were close to the test pipe. Therefore, the pipe was supported by wooden blocks, and all the pipe fittings were made of nylon.

The pull-rig was a pulley system operated by a 3-phase induction gear motor as shown in Figure 4.8. Speed control was implemented by powering the induction motor with a Siemens programmable power inverter (MicroMaster 420). These heavy current devices were screened, powered, and controlled by an electrically isolated power box to reduce electrical interference. For the heavy current connection diagram, see Appendix C-2.

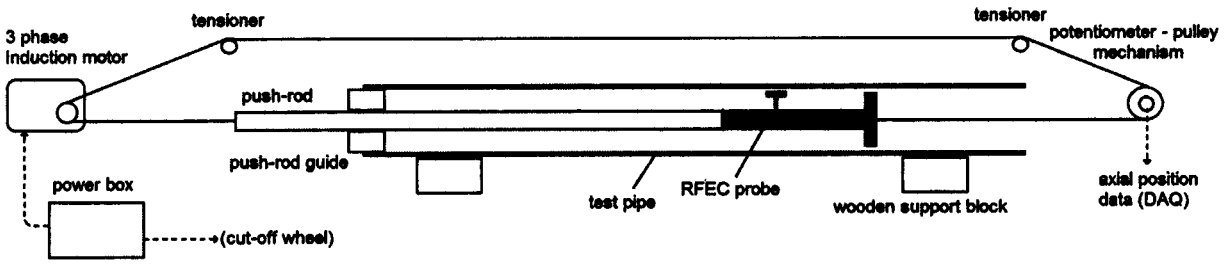

Figure 4.8 – RFEC testing rig overview
Electrical connections are shown by dotted lines

It was required to be able to maintain a constant circumferential position of the probe during inspections. For this purpose a nylon bush was pressed into the drive end of the pipe. A second bush inside the outer bush was able to rotate freely but could be locked with nylon bolts. The inner bushing was a sliding fit to a push-rod (80mm class 6 PVC plastic pipe) which could attach to the detector end of the probe with nylon bolts. The inside of the inner bush had one rectangular key way (5mm by 5mm) cut into it and the PVC pipe had a 5mm by 5mm rectangular PVC strip glued to it axially (i.e. a single toothed spline). The strip was a light slide fit in the keyway.

The probe fitted inside and bolted to the push-rod, and had a rotational position tolerance of less than ±0.6mm on the circumference (<2.9°). Relative to the effective diameter (8mm) of the pickup coil, this tolerance was considered insignificant. This design allowed sliding axial movement of the probe at fixed circumferential positions (Figure 4.9).

Figure 4.9 – Push-rod guide (nylon bushing) shown in position for testing

A multi-turn 10kΩ potentiometer (Spectrol 534) was used to determine the axial position. The wiper was connected to the pulley shaft via a 0.8mm thick aluminium strip. The strip specifications were chosen so that it would yield before the transmitted torque could damage the potentiometer and thereby protect the position sensing system from over-runs. The potentiometer terminals were connected a ±20V DC supply and the wiper signal was

measured directly by the ADC (input impedance 144kΩ). The load life of 900hrs and high repeatability was considered sufficient for the testing of this project.

As mentioned at the start of this chapter, the probe velocity is limited by a wide range of factors; among them, the spatial resolution (dz), the lateral extent of the defect signal, and the size of the detectors sensing area. The maximum scanning speed may be approximated by $V_{max} = dz/t$, where t is the length of time that determines data batch size used for a single demodulation (FFT), see Section 3.2.3. Previous studies found that a spatial resolution of dz = 10.3mm was required to detect axial stress corrosion cracks on the outside of ferromagnetic pipes [93]. A smaller dz value (i.e. a higher resolution) is not likely to significantly improve the signal accuracy as the sensing area of the detector face (being the cross-sectional area of ferrous core) is 8mm across.

A drive frequency of 40Hz (a period of 0.026s) is typical in ferromagnetic pipe and therefore taken to be the lower limit in this study [94]. To achieve accurate amplitude and phase measurements, several periods must be "averaged"[45] in each demodulation. An average of 50 periods (i.e. t = 1.25 seconds per demodulation) was necessary by to reduce the demodulation error to less than 0.5%, using an Agilent oscilloscope (DSO5054A) as a benchmark. Therefore V_{max} = 8.3mm/s (10.3/1.25).

The speed calculation above depends on the extent of the defect signal which in turn depends on the defect dimensions. Thus, this study needs to inspect defects which are similar to fatigue cracks, i.e. narrow and circumferentially oriented.

4.5.2 Defect Fabrication

As discussed in Section 2.5, although the major requirement of this NDT system from a Fracture Mechanics viewpoint is defect depth (a_i), the surface crack length ($2c$) is also useful in order to determine the geometry correction factor (Y). It may be recalled that the ratio $a/2c$ - called the crack aspect ratio - describes the crack shape. As fatigue crack shapes may vary widely depending on loading history (Figure 4.10), the testing of two different defect profiles is included in this study for comparison. These are the straight fronted and thumbnail shaped profiles (Figure 4.10). A third fatigue crack profile may

[45] There are various reasons to average multiple signals, among them, the time required to reach 'steady state', noise reduction, and improvement of frequency domain resolution.

occur called the crescent moon shape. However, this profile was not studied due to difficulty in machining this shape.

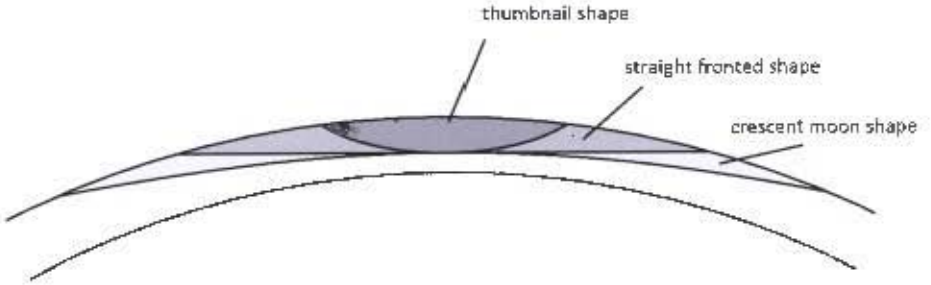

Figure 4.10 - Fatigue crack shapes

To machine the thumbnail shaped and straight fronted defect shapes, two cutting blades were used; a circular diamond blade and a straight edged hack-saw blade (Figure 4.11).

a b

Figure 4.11 – Hack-saw blade (a) and diamond blade (b)
Both blades are width – 0.3mm

Hack-saw cuts could be made manually with the aid of a flexible steel guide to prevent slit widening close to the tapered slit ends. The diamond blade was very delicate, therefore a machine was required to achieve gentle cutting to precise depths.

For this purpose a precision cut-off wheel was built. All moving parts were mounted to a hinged and counterbalanced length of channel (100 x 50 x 8), welded into a v-shape (hinged at the apex as shown in Figure 4.12). This ensured that the metal structure could be lifted away from the test pipe during testing and the blade could return to the same cut precisely.

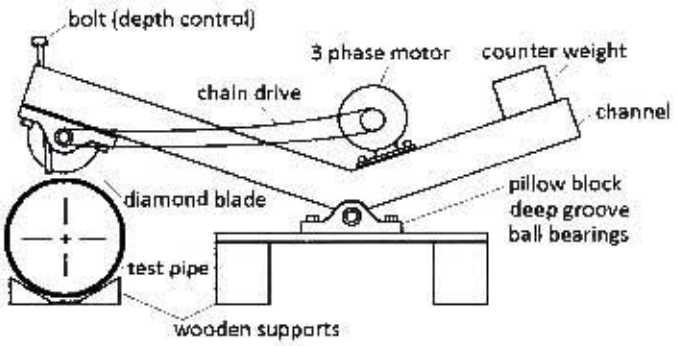

Figure 4.12 – Cut-off wheel schematic

The cutting blade was driven by a 0.2 kW 3 phase motor mounted close to the hinge. The cutting blade was clamped between steel spacers. These were designed to permit only the outer 5mm of the blade to protrude to provide maximum support. These were fastened onto the cutting shaft by a threaded nut and were located by a shoulder. The blade shaft was balanced and mounted on pillow block deep groove ball bearings. The force on the blade and slit depth could be controlled by a fine threaded bolt (pitch 1mm) threaded through the channel above the blade so that the blade position could be accurately positively limited. The blade was cleaned while cutting by a ceramic tile glued to the pipe wall and lubricant was applied regularly. A counter weight was used to control the force on the blade. Damping was required to prevent vibrations[46].

Figure 4.13 – Cut-off wheel clamped to the work-station (left) with the blade, blade supports and bolt (depth control) shown (right)

[46] This was achieved by attaching the blade arm to a plastic sleeve. The sleeve was made adjustable by a hose clip. This allowed it to slide with the trajectory of the cut-off wheel arm located on a vertical shaft provided by a retort stand.

4.6 Summary

This chapter detailed the design of an RFEC probe and supporting structure motivated in Chapter 3. As drill pipe was not available for this project, a scaled-down pipe (81mm ID, 4mm wall thickness) was tested instead. As many of the parameters for the RFEC system are reliant on the pipe geometry, these differences were noted. To accommodate future testing of thicker walled pipe or different wall thicknesses, the guides and supports were designed to be adjustable.

The RFEC probe was designed to ensure conventional RFEC field distributions (and the possibility of the use of skin depth equations for calibration). Thus the structure of the probe was comprised mainly of PVC piping. The main component of the electrical system was the onboard pre-amplification circuitry. The detector signal was amplified by an AD620 instrumentation amplifier, chosen for its high gain, low noise and high CMRR capabilities. However, the low signal at the amplifier inputs was susceptible to contamination with noise; therefore the power supply was decoupled and data cables were shielded. It was essential to "short" the pipe wall to the shielding of the data cables.

The required demodulation of the detector signal with reference to the reference signal was implemented digitally due to the additional flexibility. Analogue waveform and position data was converted to digital data (10kS/s ADC) and imported to Matlab via USB. Demodulation was achieved by computing the Fourier transforms for both the reference and detector signals and subsequently, the complex quotient at the probe drive frequency, to extract the relative magnitude and phase components of the detected signal.

An exciter detector distance of 219mm (2.7 pipe diameters) was chosen after pullout tests confirmed the location of the remote field zone. Significant improvements in data quality were made after observing that the ADC was inactive for the majority of the inspection due to the time spent demodulating the waveforms. Thus the data acquisition process was changed to continuous sampling. The final system could perform five demodulations in 4 seconds (offline).

The probe pull-rig comprised an AC motor driven pulley system, with speed controlled by an inverter, and a multi-turn potentiometer which provided the positional feedback. The maximum probe velocity was estimated at 8.3mm/s, limited by an axial resolution of

10.3mm (based on the demodulations per second result of the previous paragraph). The overall setup is shown in Figure 4.14.

The following chapter presents inspection results produced by the RFEC probe developed above. However, many of the parameters set in this chapter are related to the lateral extent of RFEC defect signals (probe speed, detector size and demodulation time). The values chosen in this chapter are, inherently, estimations as the defect response of this RFEC system was not yet known. Therefore the first section of the following chapter is a pilot study to verify these parameters. Note that this RFEC probe design is specific to the test pipe selected in this chapter. Subsequent testing of thicker walled pipe (Chapter 6) would require higher drive current, lower drive frequencies and further pullout tests to determine the new exciter detector distance.

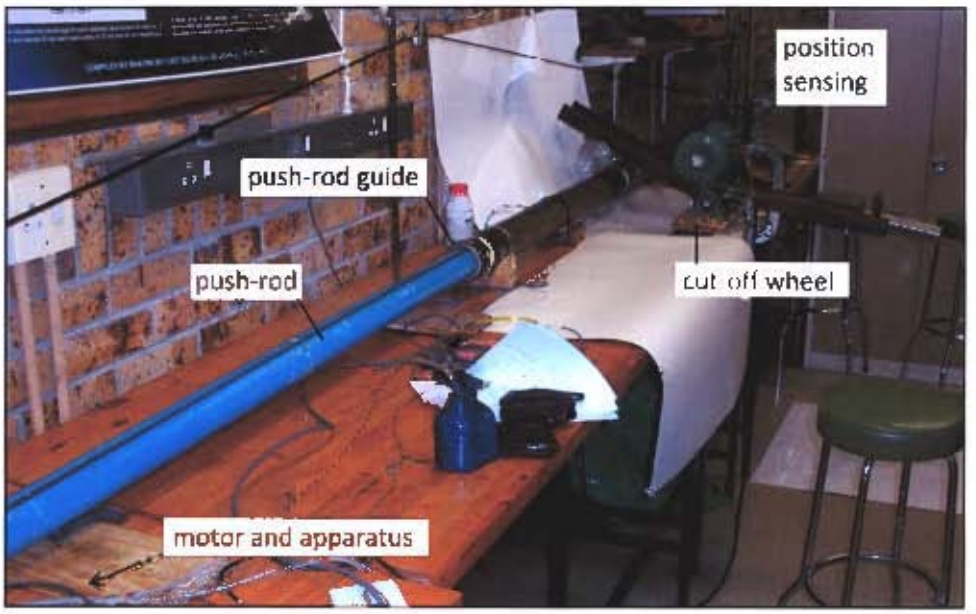

Figure 4.14 – Final RFEC testing setup

CHAPTER 5 DETECTION OF CIRCUMFERENTIALLY ORIENTED SAW-CUTS

5.1 Introduction

This chapter presents inspection results obtained from the RFEC testing rig developed in Chapter 4. As the aim of this NDT system is ultimately the early detection and monitoring of circumferential fatigue cracks, this chapter focuses on establishing these capabilities by detecting a series of saw-cut defects. Note that the assumption is that narrow saw-cut defects are representative of fatigue cracks, and that these effects are explored further in Chapter 6. All the defects in this chapter are machined with the apparatus developed in Section 4.5.2, therefore these have a width of 0.3mm, and can be either straight fronted or thumbnail shaped.

As mentioned in the previous chapter, a pilot study emulating fatigue crack growth with saw-cuts is required. The aim of this study was to:

- Consolidate or define the RFEC probe parameters chosen in Chapter 4,
- The usefulness of RFEC inspection history for identifying 'progressing' and 'non-progressing' defects.
- Identify and address any adverse effects of the RFEC system (Section 3.2),
- Identify the smallest detectable defect in the presence of these effects.

The section following the pilot study presents inspection results from defects inspected at multiple circumferential positions to determine the defect profile. As RFEC signals are not readily amenable to Fracture Mechanics interpretation, the final part of this chapter is dedicated to the calibration of the RFEC defect signals to slit depth.

5.2 Pilot Study

This section presents the results of RFEC inspections of the full length of a 2100mm pipe (ID 81mm, wall thickness 4mm) for a circumferential saw-cut defect of incrementally increasing depth. This section therefore aims to investigate the overall detectability of circumferential defects with the system parameters chosen in Chapter 4. This aim has two

main corollaries: the characterisation of non defect signals originating from the pipe and environmental noise, and concomitantly determining the minimum depth saw-cut detectable with this system.

5.2.1 Methodology

The inspections in this section were conducted with the detector positioned circumferentially to pass directly beneath the centre (maximum depth) part of the defect profile as this position produces the maximum defect signal on a circumferential defect and therefore is most likely to detect the smallest defect [81].

As the RFEC probe had absolute and differential mode capabilities, a brief comparison of these modes was conducted to determine the most useful mode for this pilot study. To test these modes without damaging the test pipe[47], a small metal nut (M5) was placed on the outside of the pipe wall such that the detector in each mode measured the field perturbations of the external metal (Appendix E-1: Absolute and Differential Mode Results). The use of external metal as a surrogate for an embedded defect was tested by Teitsma [76]. The high repeatability achieved by absolute mode and the potential loss of data possible from differential mode[48] motivated for the use of the absolute mode in this pilot study.

A saw-cut defect was located at 1715mm from the 'start' of these inspections, as shown by the vertical dotted line throughout the strip chart results (Figures 5.1 and 5.2). Note that multiple inspections were performed as crack depth was increased. The experimental setup is shown throughout this chapter above each set of strip charts. Note that the final 220mm of the exciter end of the pipe could not be inspected due to the requirement for continuous pipe between the exciter and the detector (Figure 3.6). Black arrows are used as markers to highlight certain results for later discussion. The significance of each marker is listed below:

(a) The background signal measured from defect free pipe

(b) The first discernible detection

(c) The final (through wall thickness defect) signal

[47] This was considered important as the pilot study is primarily to investigate all of the differences between RFEC signals measured from damaged and undamaged pipe material.

[48] Common mode data is eliminated without being stored.

The procedure for each inspection was to:

- Calibrate the reference signal by adjusting the frequency and amplitude of the drive coil voltage at the frequency generator to 80 Hz and 700mV_{pk-pk}.
- Normalise the detector signal to the reference signal ($|V_{sig}| / |V_{ref}| = 1$) by adjusting the gain of the onboard pre-amplifier.
- Complete a single scan.
- Increase the saw-cut defect depth by approximately[49] 0.5mm.
- Defect depths were measured with modified[50] vernier calipers with an accuracy of 0.05mm.

5.2.2 Single Scan Results

The depth of the circumferentially oriented saw-cut is increasing as shown in the title of each strip chart. Note that the amplitude is represented as a dimensionless ratio of the reference coil voltage to the detector voltage.

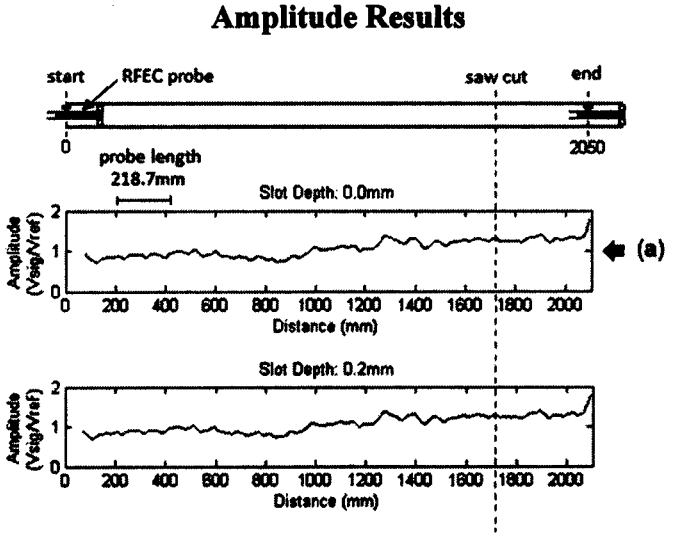

Figure 5.1 – Amplitude results from RFEC testing of the full pipe length as crack depth increases
The markers identify consecutively the background signal (a), the first discernible detection (b) and the through wall thickness inspection results (c).

[49] Constant increments were not strictly adhered to in this pilot study.
[50] A 0.3mm width slip was attached to the end in order to be insertable into the machined slits.

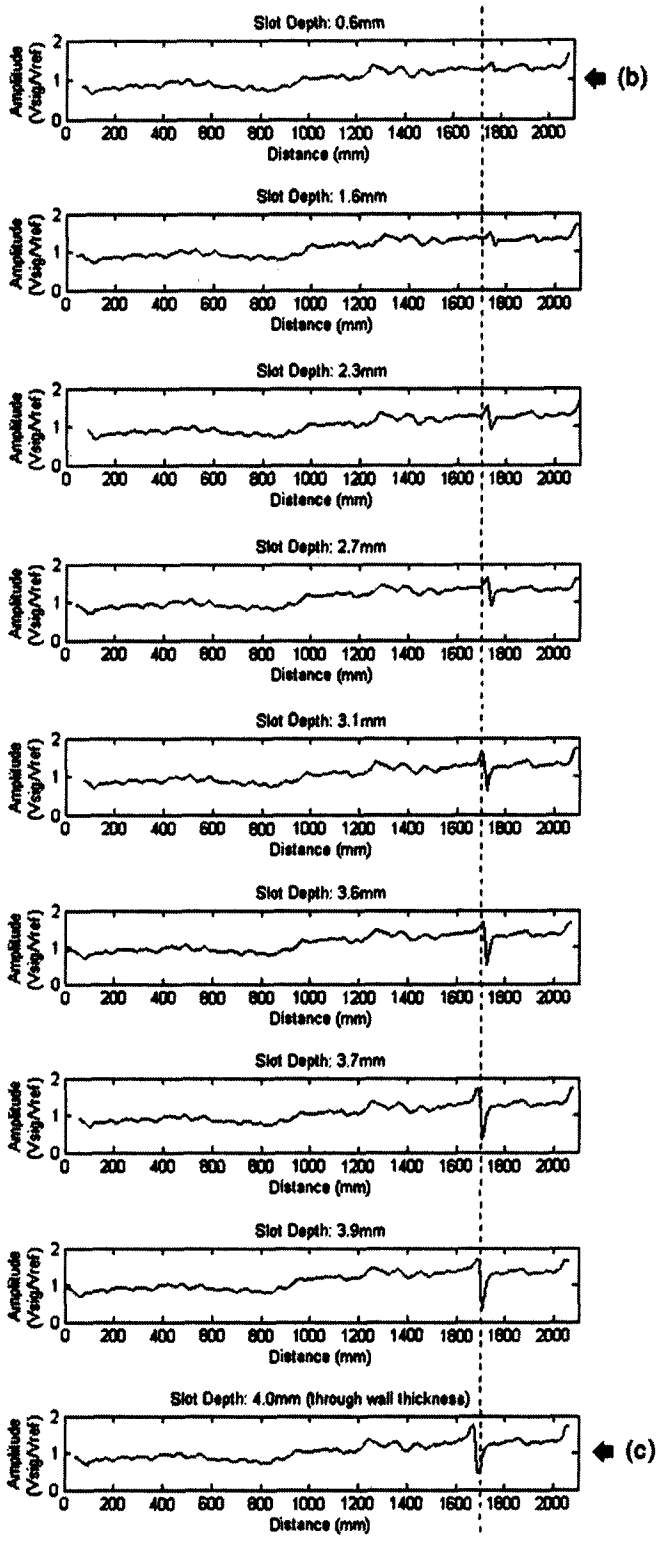

Figure 5.1 – continued

Phase Results

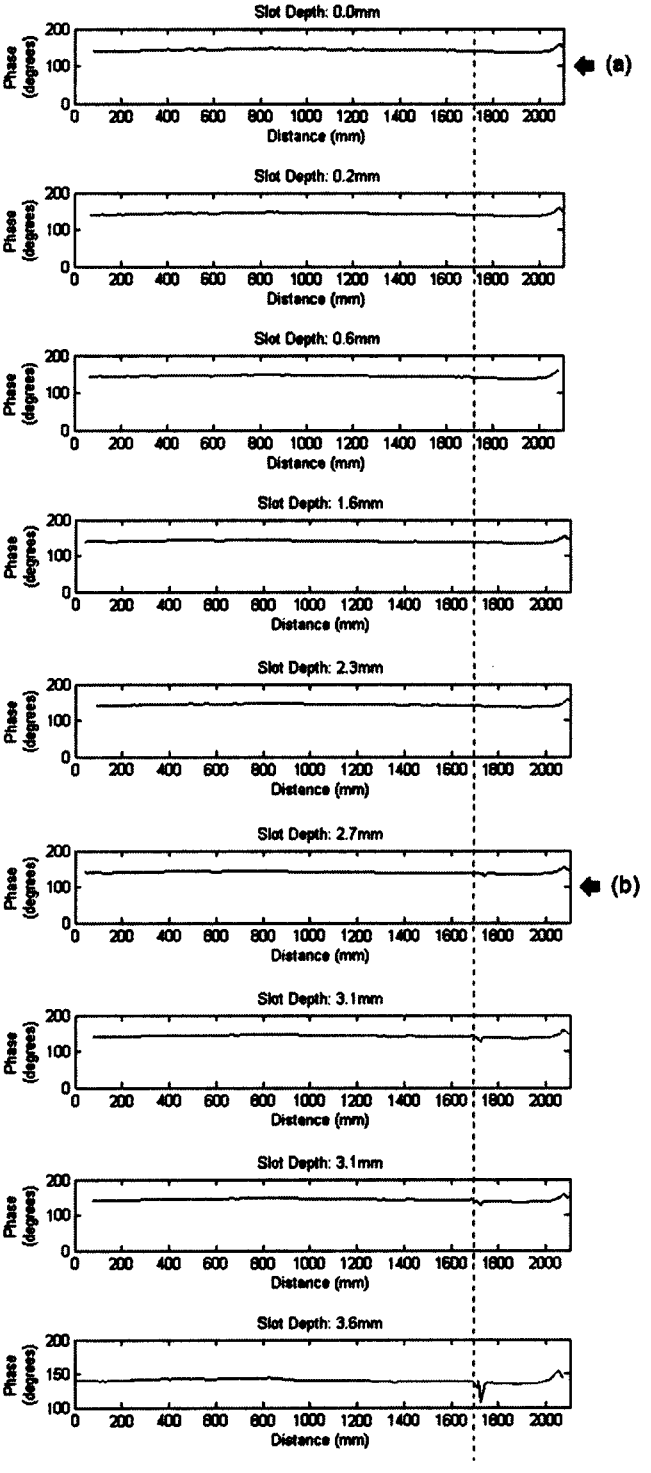

Figure 5.2 – Phase results from RFEC testing of the full pipe length as crack depth increases
The markers identify consecutively the background signal (a), the first discernible detection (b) and the through wall thickness inspection results (c).

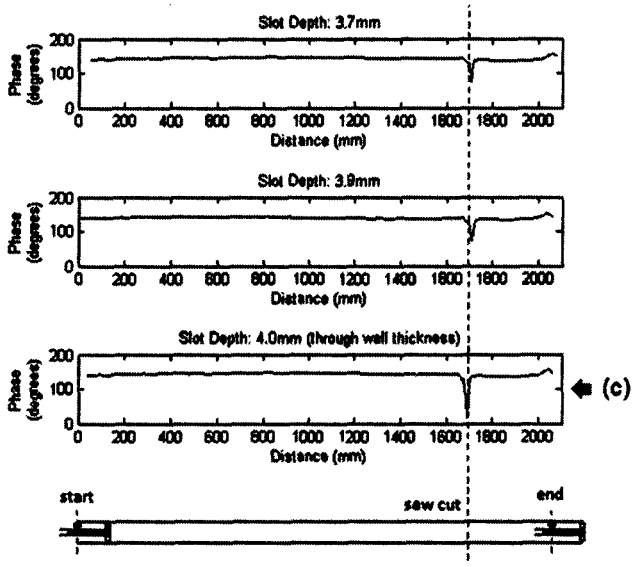

Figure 5.2 – continued

5.2.3 Discussion of Defect Detectability

Note firstly that the first discernible defect indication (b) is different for each of the amplitude and phase sets of strip charts – the saw-cut defect signal appears in the amplitude component at 0.6mm slit depth and in the phase component at 2.7mm slit depth. Therefore the smallest detectable saw-cut defect was 0.6mm depth (Figure 5.1). Similar results by Ivanov showed that, for circumferentially oriented defects, the amplitude component was more sensitive than the phase component (where the phase component was more sensitive to axially oriented defects)[51] [93].

Having identified the defect signal, the following paragraphs discuss the other signals and adverse effects found in these results. Note that the axial location of the defect signal does not at first appear at the exact true defect location, but progresses toward this location as slit depth increases (dotted line in Figure 5.1). It is conceivable that the field alterations created by small defects is so small that the field direction is remaining relatively co-axial with the pipe for longer before it penetrates the pipe wall (radially) and is therefore sensed further down the pipe. In addition, 'end' effects appeared in the final 50mm of each strip chart as an 'upturning' in both the amplitude and phase strip charts. This effect

[51] It is possibly relevant that this work by Ivanov used a different exciter configuration which generated a magnetic field rotating about the pipe axis, similar to the rotor of an AC motor. The aim was to generalize the sensitivity of the RFEC method to all defect orientations.

is not likely to occur in drill pipe RFEC implementations due to the screening effect that the flanges will have on the remote field (Section 3.2.2). However, it was necessary to avoid the final 270mm of the test pipe for further testing (50mm added to the 220mm exciter detector distance).

The most prominent feature of the amplitude data is the significant background signal. The high repeatability of this signal suggests that it is a characteristic of the pipe wall rather than the probe or the defect. These fluctuations are likely to be caused by permeability inhomogeneities originating from impurities in the pipe material or uneven heat treatment during forming [76]. This high repeatability can be seen by superimposing the signals identified by markers (a), (b) and (c) in Figures 5.1 and 5.2 (plotted in Figure 5.3). Note that without the background signal, the first detection (a = 0.6mm in the amplitude component) is easily mistakable for background signal. Also note that although the phase component appears relatively free of background noise, it is less important as detection by this signal component only occurs at a = 2.7mm.

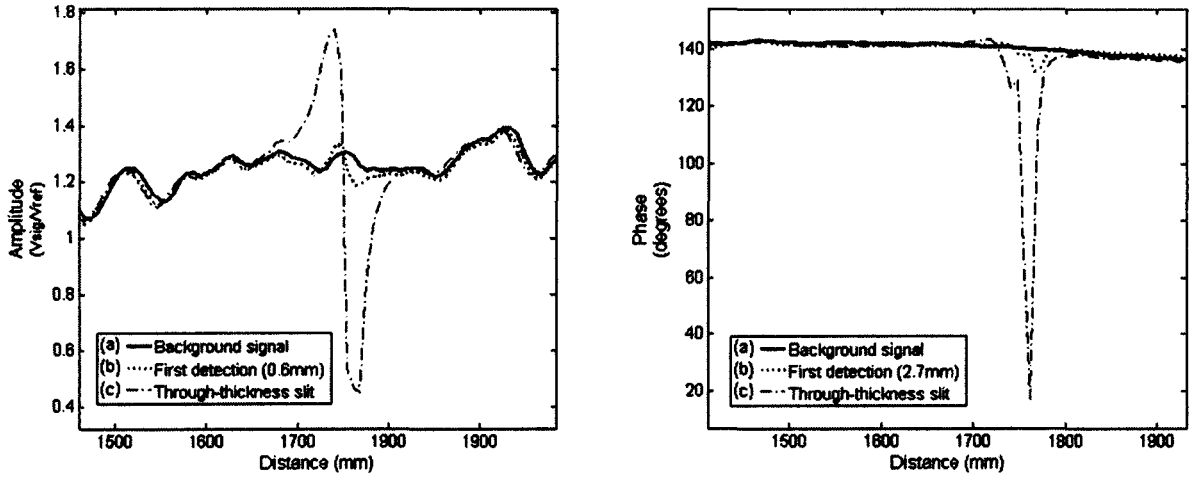

Figure 5.3 – Superimposed amplitude and phase signals
Signals represented correspond to the markers in Figures 5.1 and 5.2

The high repeatability of the amplitude component of the background signal and early detection with this component suggests that these results might be significantly improved by implementing background signal subtraction. Note that this requires regression of the background signal for the purposes of interpolation and time alignment of the stored background signal with the new inspection data. However, regression by conventional

least-squares based analysis was computationally intensive and did not achieve accurate fitting due to the highly irregular shape of the background signal[52]. Better speed and fitting-accuracy[53] was possible with a generalised regression neural network (GRNN), this method interpolates new data points on the background signal as a linear weighted sum of Gaussian basis functions (for more details see Specht [95]). Superior performance was attributed to the low computational requirements and, that the smoothness of the regression could be adjusted by setting the width of the Gaussian functions. Optimal performance was achieved by setting this width to the approximate width of the crests and valleys of the background signal, that is 4mm (for GRNN Matlab code - see Appendix D-3).

However, the quality of the background subtracted signal was found to be highly vulnerable to slight axial misalignments in the amplitude-position data. A recurring displacement error dependant on scanning direction was observed due to hysteresis in the pull-rig and position sensing systems (±6mm). This was caused by differences in the transmission length of the pulley chord between the forward and reverse scanning directions (Figure 4.4). It was also noticed that over a large number of scans, the position data tended to creep from its calibrated value at approximately 1mm per meter due to slippage at the drive pulley. To correct for these errors, the data was realigned digitally using cross-correlation with the background signal before background signal subtraction was performed (Appendix D-4).

The amplitude results of Figure 5.3 are background subtracted and using the system described above, and the results plotted below (Figure 5.4). Note that the defect signal now measures only the field perturbation generated by the defect. The remaining systematic noise was limitation of the sensitivity of the hardware and therefore could not be eliminated.

By observing the isolated defect signal, it is now possible to validate the probe speed estimated in Section 4.5.1. Note that the axial extent of even the smallest detectable defect signal is approximately 200 times greater than the axial extent (width) of the defect (defect width: 0.3mm, Defect signal width: 80mm – taken from Figure 5.4). This meant that the resolution of 10.3mm set in Section 4.5.1 resulted in 7 data points over the

[52] Very high order polynomial basis functions are required to fit the irregular shape of the background signal, the process was found to be computationally intensive and ill-conditioned.
[53] Mean-square error computed via bootstrap sampling.

smallest defect signal envelope. As this provided sufficient representation of the smallest defect signal, the estimated speed of 8.3mm/s was considered valid for further testing.

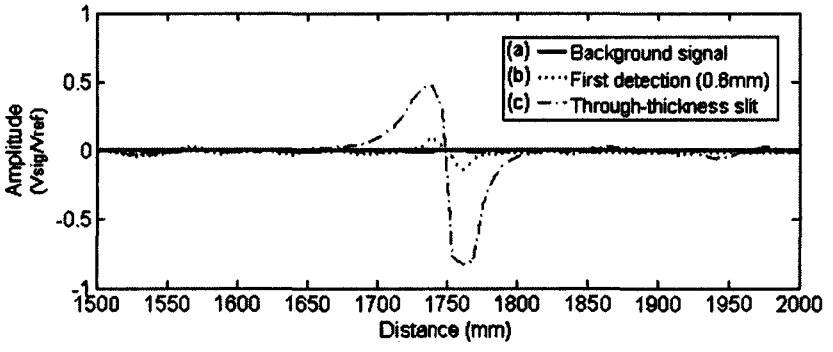

Figure 5.4 – Background noise subtracted amplitude component of the signal from the defect region

The pilot study has provided an account of the RFEC system responses including certain adverse effects. These findings validated the preliminary result for the smallest detectable circumferential saw-cut (a = 0.6mm) and the probe speed. The new post-processing stage allows defect signals to be studied in relative[54] isolation from the background signal, making it possible to study RFEC defect signals in more detail. However, in reality the defect signal resolution of an RFEC tool is limited by the spacing of the detectors in a circumferential detector-array. These effects are investigated in the next section.

5.3 RFEC Detector-Array Results

The previous section showed that defect signals may be studied by previously recording the pipe background signal from the defect free pipe. Thus it was possible to identify 'progressing' and 'non-progressing' defects and validate the measurement for the smallest defect depth detectable with this RFEC system. Hence the first Fracture Mechanics requirement, a_i, has been examined. As circumferential data is captured in detector array data, the aim of this section is primarily to investigate the second Fracture Mechanics parameter - defect length ($2c$). Note that defect length may vary as a function of defect depth or defect shape. It may be recalled that the latter is described in Fracture Mechanics as the defect aspect ratio - $a/2c$. To aid in the understanding of how RFEC defect signals

[54] As only the repeatable content is subtractable, the systematic noise remains.

respond to aspect ratio, two slit shapes are studied: the straight fronted and the thumbnail shaped slit defects.

5.3.1 Methodology

The prototype RFEC probe built for this project records data from a single detector while in practice RFEC probes generally carry multiple detectors arranged in a circumferential array. However, it is commonplace for RFEC researchers to simulate detector-array data by scanning different circumferential positions consecutively with a single detector [76,82]. This has the advantage that all signals are produced by a detector of the same impedance properties and gain settings.

For consistency, 5 discrete circumferential detector positions are defined below and used consistently hereafter to aid in the representation of array data. As the circumferential detector spacing of an RFEC detector array is only limited in practice by the width of the detector [96], the detector positions were separated by 10mm arc lengths (or 14.15 degree angular increments) to accommodate the 8mm wide detector face (Figure 5.5). Note that the top dead centre position (TDC) is a 'zero' position from which the other detector positions are defined. For further consistency, all of the defects in this study are always centred on the TDC circumferential position; hence the TDC position always corresponds to the maximum depth part of the slit profile (comparable to pilot study inspection results).

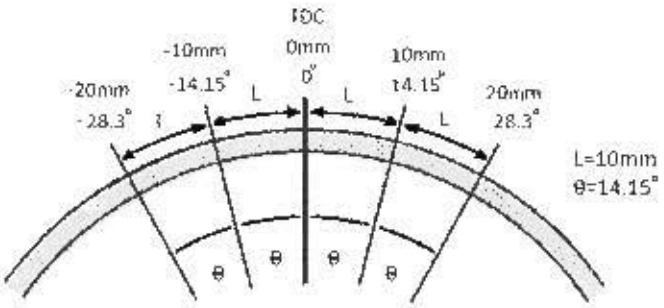

Figure 5.5 – Pipe cross-section showing the 5 circumferential detector scanning positions to generate array data. Top dead centre (TDC) is at 0 degrees (0mm) and corresponds to the maximum depth part of the slit profile

The thumbnail and circumferential defects were machined at the same circumferential position (TDC) and axially separated by 250 mm. This distance was intentionally set larger than the exciter-detector distance (220mm) to ensure the independent study of both defects (Section 3.2).

Prior to testing and defect machining, background signals from the defect free pipe were recorded to enable background signal subtraction. Subsequently, the procedure for testing was as follows:

- Calibration of the frequency and amplitude of the drive coil to 80 Hz, 700m$V_{pk\text{-}pk}$.
- Circumferentially oriented straight fronted and thumbnail shaped slits were machined in 1mm increments; each slit was centered on the TDC position and axially spaced as shown in Figure 5.6 - (a), therefore simulated array defect signals were recorded at depths: 1mm, 2mm, 3mm and 4mm.
- Defect depths were measured with the modified vernier calipers (as with the pilot study) with an assumed accuracy of 0.05mm.
- A single inspection was performed at each predefined circumferential detector position (see Figure 5.5).
- The axial positional errors were digitally corrected (realigned by cross-correlation with the background signal – the reference) the background signal was subtracted.

Figure 5.6 shows the test setup (a), the circumferential signal variation (b), and the background subtracted signals (c). Results shown are from the 2mm deep thumbnail shaped and straight fronted defects (in series) following the above procedure.

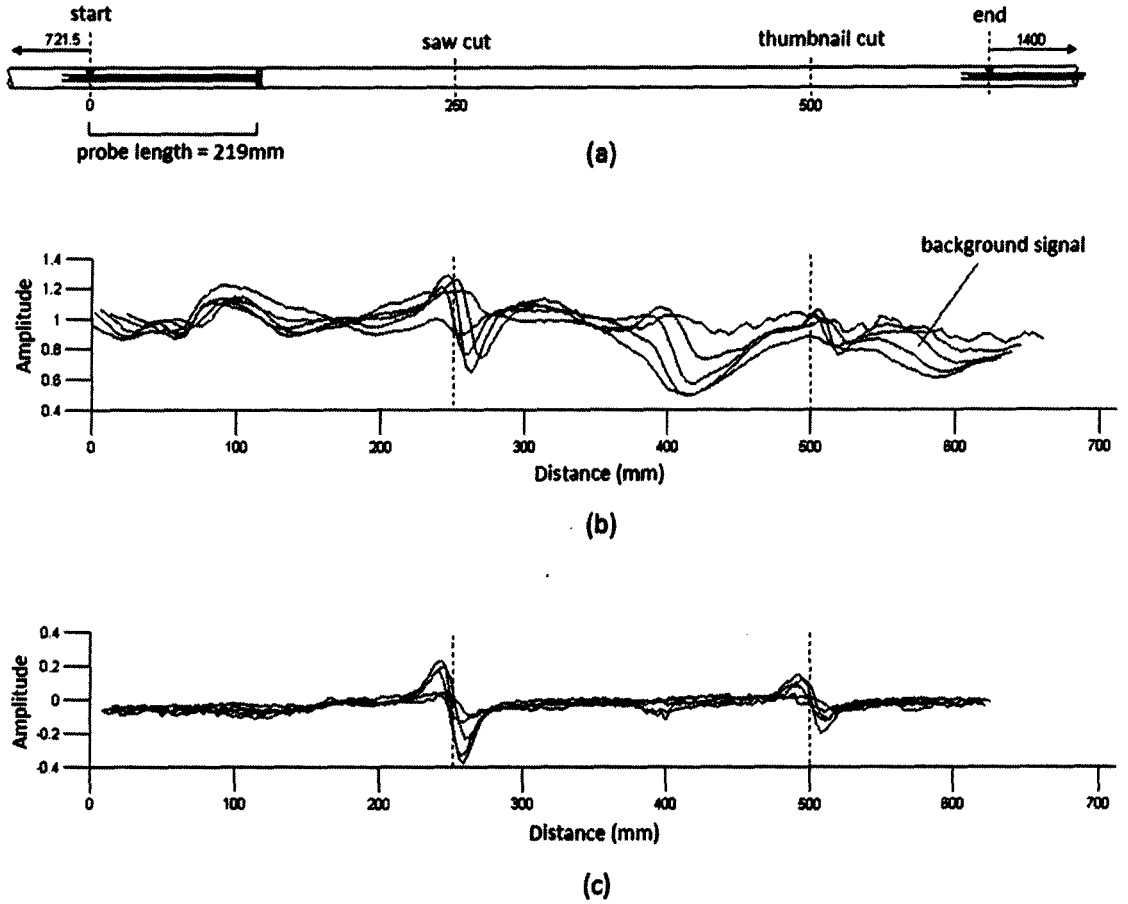

Figure 5.6 – Array inspection results from 2mm deep straight fronted and thumbnail shaped cuts
A schematic with details of the test setup for this section is shown schematically (a); note the difference between unprocessed data (b) and centred-background subtracted data (c). Note that the end-on view of the processed data in (c) shows a close to zero mean and localized defect signals.

5.3.2 Detector-Array Strip Charts

The background subtracted results from circumferential straight fronted and thumbnail shaped defects are shown in the array strip charts below (Figure 5.7 and 5.8). Again, schematics are shown above each set of strip charts to show the test setup. Note that the vertical axes show both the circumferential spacing of the detectors as defined in Figure 5.5 (left vertical axis) and the measured quantity (right vertical axis).

Again, a black arrow is used to indicate the first discernable detection in each of the amplitude and phase results. To enable comparison between the two defect shapes shown in each strip chart, the 'first discernable detection' was defined in these results as the first strip chart showing discernable defect signals of both defect shapes (this was dependant on the thumbnail shaped defect as these typically produced weaker defect signals).

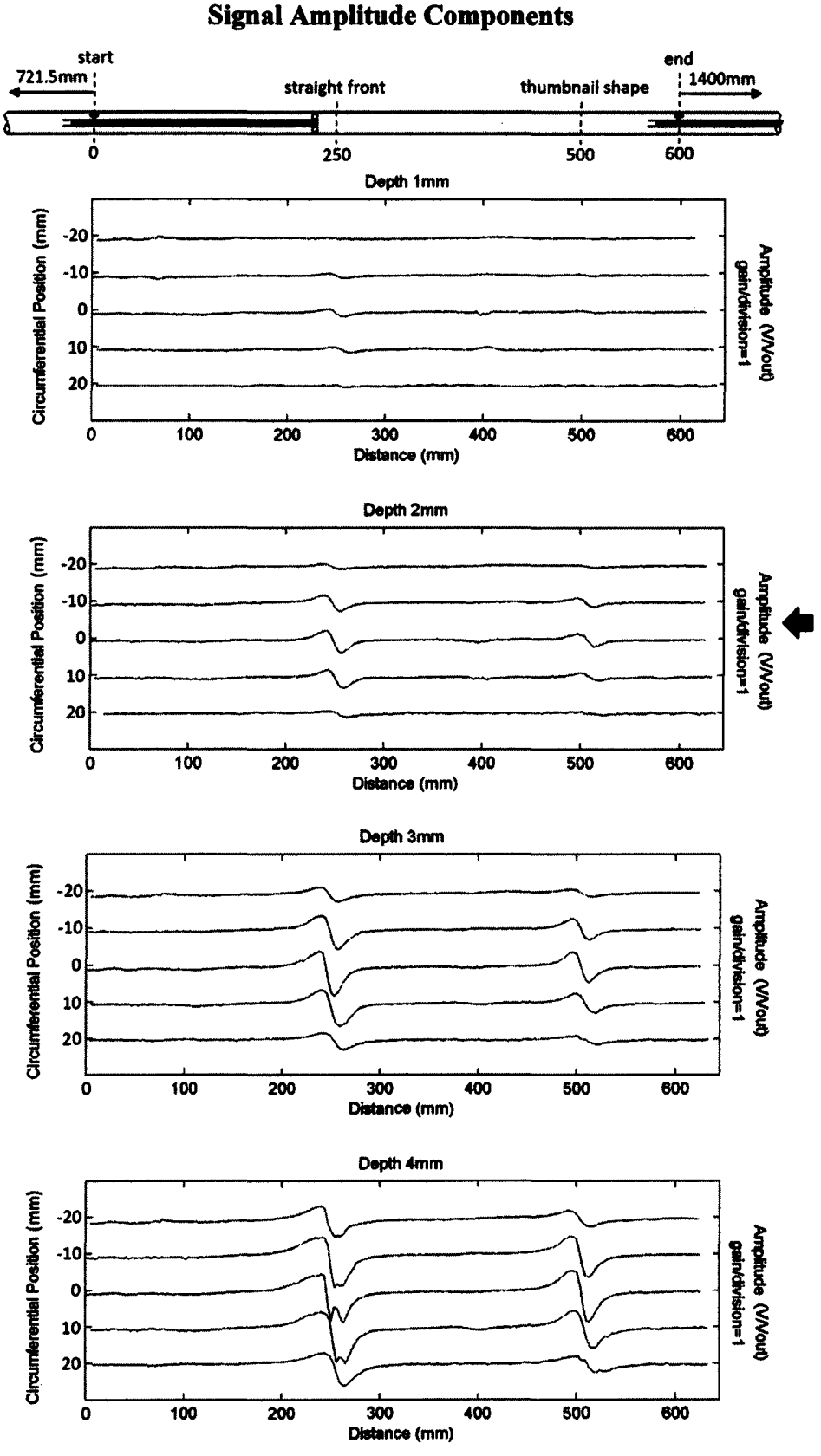

Figure 5.7 – Simulated-array results; the amplitude signal component
Defect indications of straight fronted (left) and thumbnail shaped slits (right) of 1:4mm depth are shown, The test setup is shown in the schematic (above). The arrow indicates the first detection of both defects.

Signal Phase Components

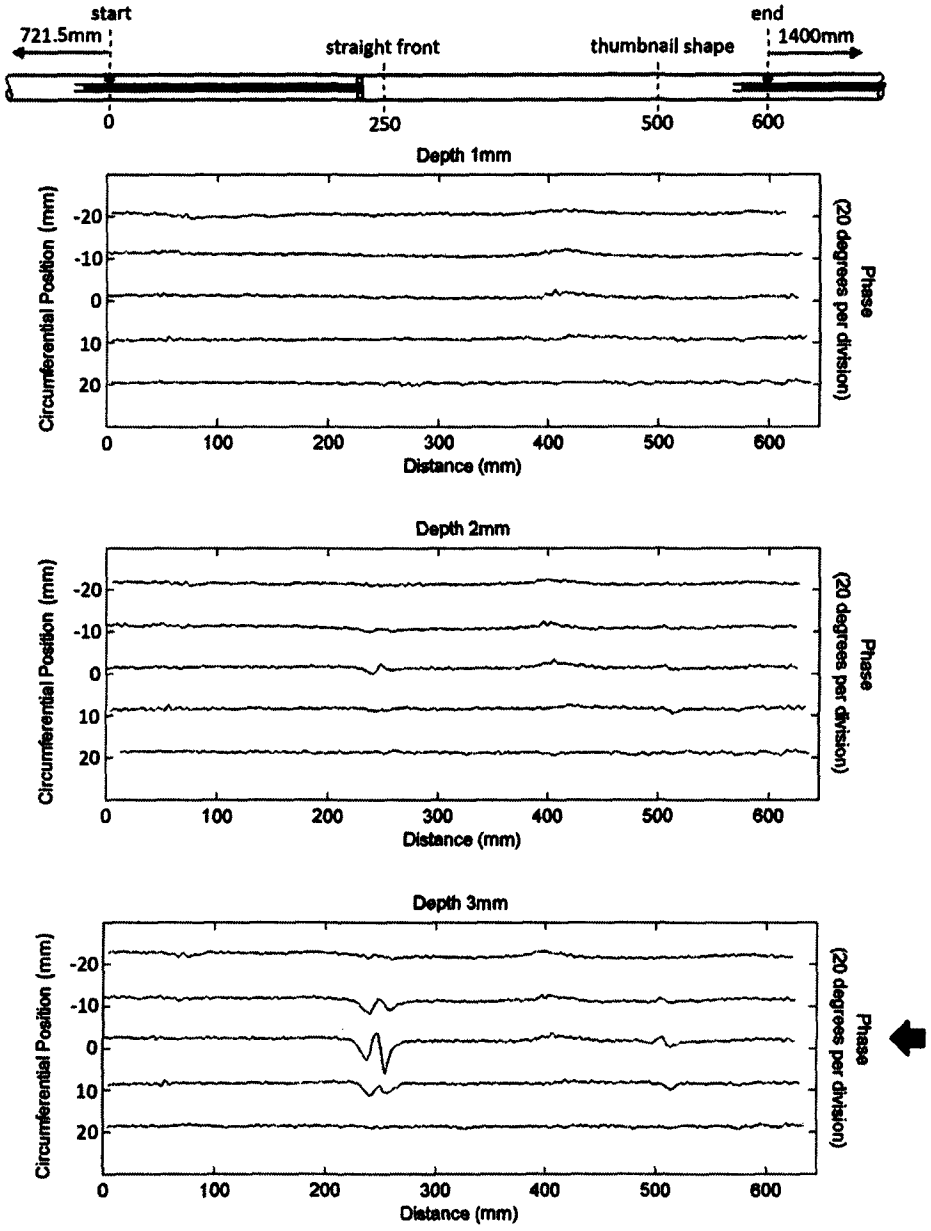

Figure 5.8 – Simulated-array results; the phase signal component
Defect indications of straight fronted (left) and thumbnail shaped slits (right) of 1:4mm depth are shown, The test setup is shown in the schematic (above). The arrow indicates the first detection of both defects.

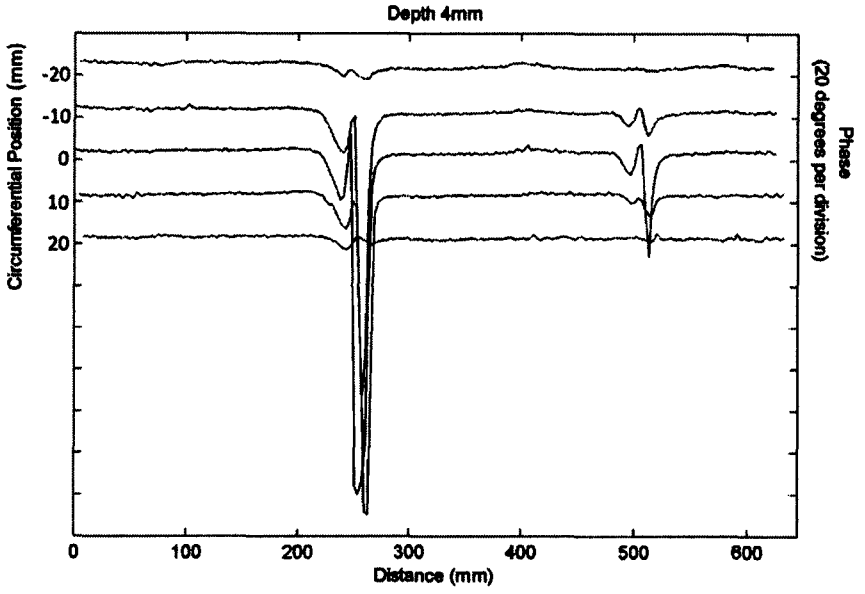

Figure 5.8 - Continued

5.3.3 Discussion of Detector-Array Results

This section discusses the capabilities of the RFEC probe to detect defect length. As previously mentioned this may result from increasing defect depth or variations in aspect ratio at a fixed depth, and is mainly useful for determining the geometric correction factor for Fracture Mechanics evaluation (Equation 2.7).

The 2mm depth amplitude strip chart showing straight fronted and thumbnail shaped slits is replotted in Figure 5.9. As defect signals appear outside the physical limits of the defect[55], the length, and therefore the aspect ratio, is not clearly defined. Nevertheless, a monotonic relationship between profile depth[56] and signal amplitude suggests that defect length may be determined by calibration.

Note that the inspection results at TDC position measures both the straight fronted and the thumbnail shaped defects at the same depth (2mm). It is therefore initially surprising that the straight fronted defect signal is almost twice the amplitude of the thumbnail shaped defect signal resulting from only a 30% increase in aspect ratio (in this case, an 8mm increase in $2c$).

[55] An effect described by Atherton to be due to the circumferentially flowing eddy currents present in the remote field zone [48].

[56] This is the depth of the defect as a function of the circumferential position at which it is scanned. This is a function of defect shape, defect depth, and the circumferential position of the detector.

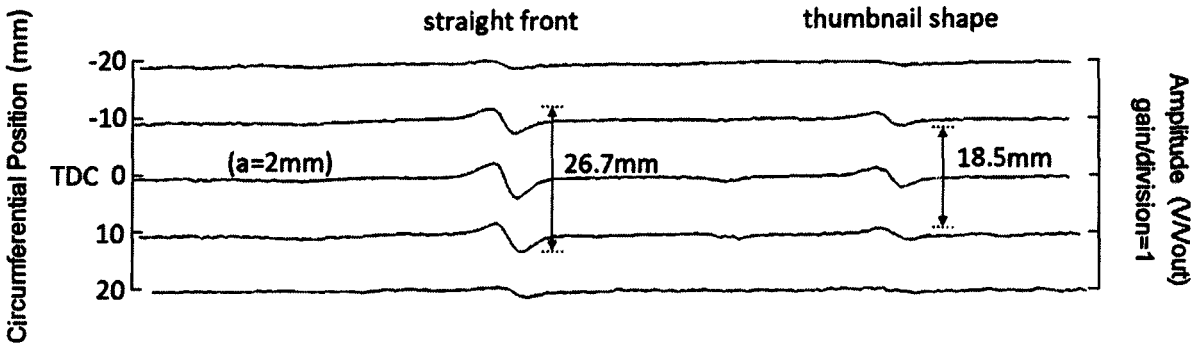

Figure 5.9 – 2mm depth strip chart showing straight fronted and thumbnail shaped defect signals
The circumferential length (2c) of each defect is shown. Note that certain of the defect signals are outside the physical length of the defect. A schematic showing the circumferential detector and axial crack positions is drawn above the strip chart.

The amplitude of the defect signal is presumably affected mainly by the increase in slit area perpendicular to the axial magnetic field (Section 3.3). However, to understand the significance of the effects of aspect ratio and other crack parameters on RFEC defect signals and subsequently, the geometry correction factor (Y) requires a more rigorous study. For details, see the work of Rambocus and Tait [97].

However, quantitative support for these observations (assuming constant aspect ratio) is possible by calibrating the defect signals to defect depth, therefore probe calibration is an appropriate final stage to this results chapter.

5.4 RFEC Probe Calibration and Signal Interpretation

The RFEC probe in this project is intended as a crack depth measurement tool. However, the current inspection system only measures defect field perturbations in the remote field. For this system to integrate with the Fracture Mechanics methodology detailed in Section 2.5, RFEC defect signals need to be calibrated to physical crack dimensions. Therefore the aim of this section is to generate a calibration curve of RFEC defect signals as a function of defect depth, and thereby show the defect measurement capabilities of this RFEC probe.

5.4.1 Calibration Methodology

In order for an RFEC signal parameter to be calibratable, a monotonic function of depth needs to be established. As the amplitude and phase components of RFEC defect signals are themselves not monotonic[57], a comprehensive evaluation of two potential signal descriptors (peak-to-peak and root-mean-square descriptors) was carried out in Appendix E-3: Signal Interpretation. The peak-to-peak amplitude performed best[58] and is also intuitively plausible as it appeared to increase monotonically as a function of defect depth in the pilot study results.

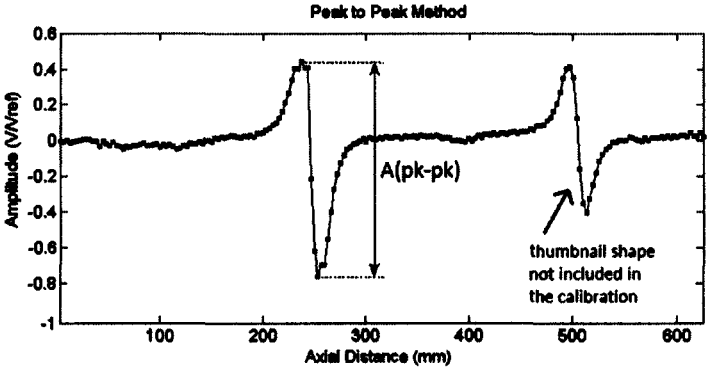

Figure 5.10 – Peak-to-peak method showing a single scan of straight fronted and thumbnail shaped defect signals

The previous section found that variations in aspect ratio could significantly affect the defect signal amplitude; therefore for consistency the calibration curve was only generated from straight fronted slits (also shown in Figure 5.10). This defect shape was chosen as it tends to achieve early detection making better use of the dynamic range of the RFEC probe.

To generate peak-to-peak amplitude data for a calibration curve, a range of straight fronted defects were machined into the test pipe and 10 inspections were performed at each depth to improve the accuracy of each amplitude measurement (Figure 5.11).

[57] The amplitude component defect signal is similar to a single period of a sinusoid, and the phase component defect signal; a negative-going double peak.

[58] This parameter was evaluated as having the largest invertible region and tightest confidence bands.

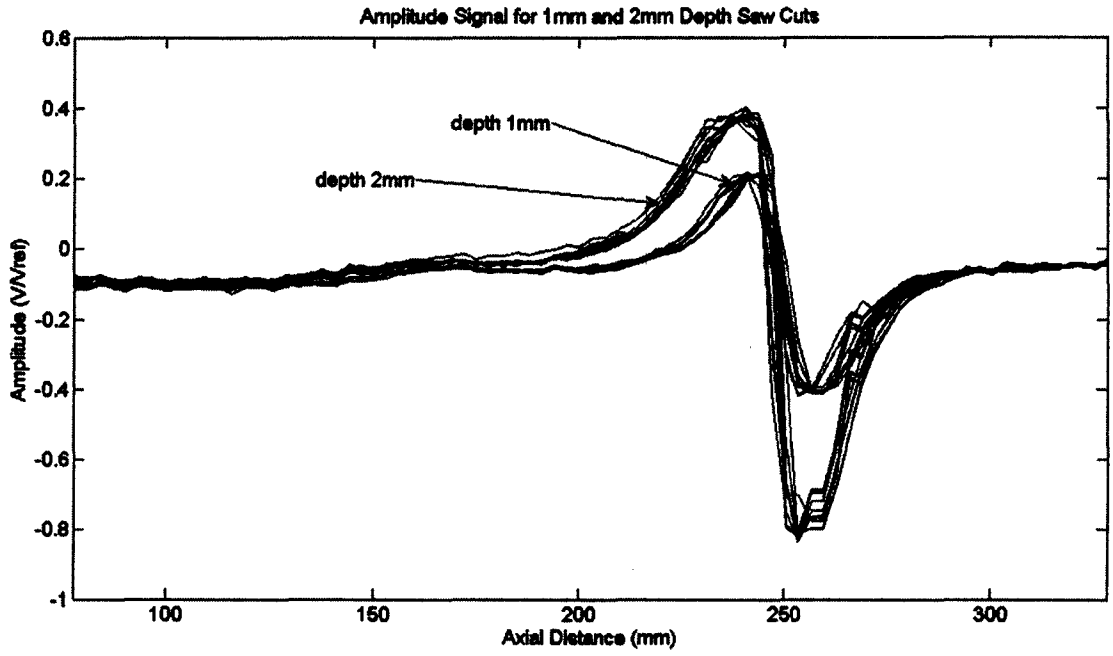

Figure 5.11 – Examples of defect inspection results showing a=1mm and 2mm results

By extracting the peak-to-peak amplitude from each defect signal, a database of peak-to-peak amplitude – defect depth data was created. As the amplitude – defect depth data was expected to be non-linear (Equation 3.2), this data was fitted with 2nd order polynomials as shown in Figure 5.12. 95% confidence bands are included to illustrate the scatter of the data but are not statistically defensible (generated from only 10 data points).

Slit depths were inspected at approximately 0.2mm depth increments from 0-1mm to improve the resolution close to the detection boundary (0.6mm – Section 5.2.3), and 1mm depth increments thereafter.

The calibratable region was bounded by upper and lower limits as shown by vertical dotted lines in Figure 5.12. The lower depth limit is the detection limit (a = 0.65mm), note that there is a noticeable reduction in variance at this depth[59] corresponding closely with the first detection found in the pilot study (a = 0.6mm). The upper depth limit was set at a = 3mm (75% wall thickness) as distorted signals resulting from slits close to full penetration are not fittable by the calibration function.

[59] As the defect signal becomes smaller than background noise, the peak-to-peak result was measured on systematic noise which is inherently of higher variance.

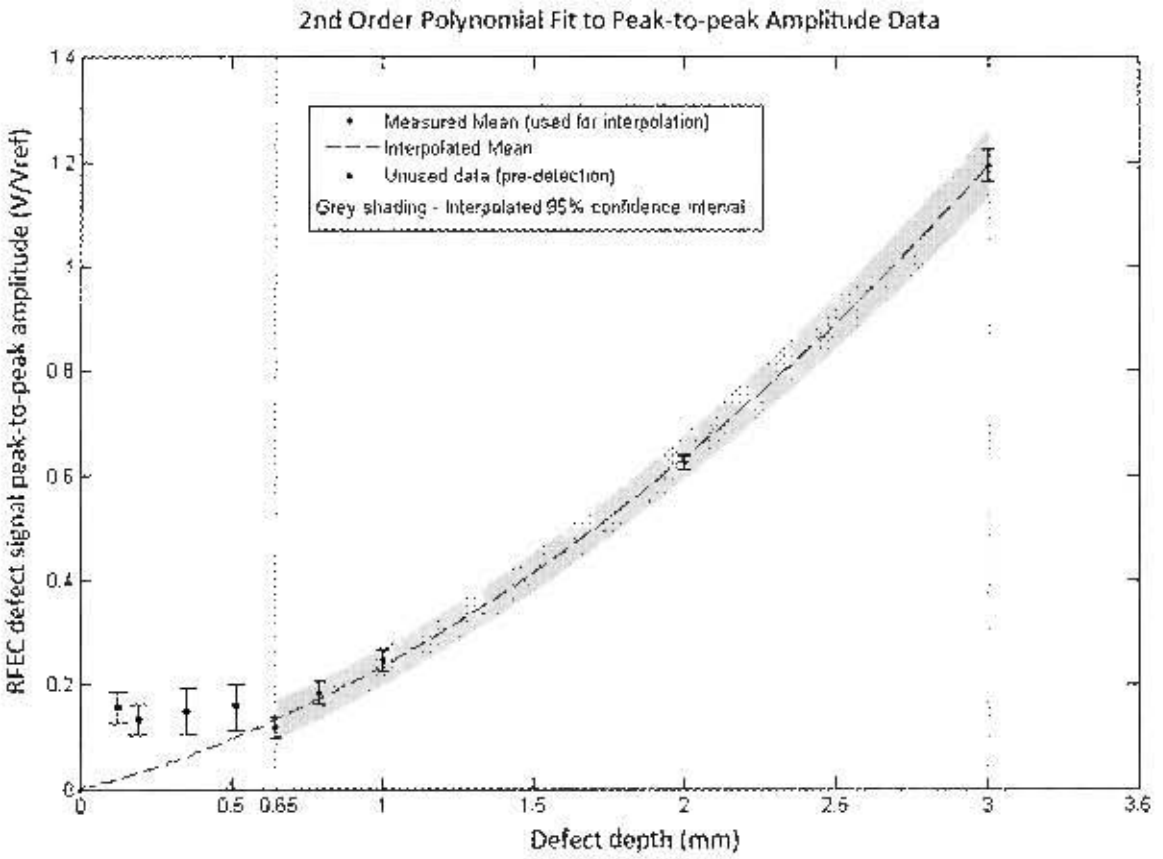

Figure 5.12 – Peak-to-peak amplitude signal vs. defect depth calibration curve

The amplitude factor is the peak-to-peak amplitude of the RFEC defect signals at each straight fronted slit depth with the background signal subtracted as shown in Figure 5.10 and Figure 5.11. The upper and lower limits of the invertible region are shown by vertical dotted lines. Discrete markers show measured amplitude and depth values (and corresponding 95% confidence intervals), whereas the continuous lines were interpolated with 2nd order polynomials. The shaded region shows the 95% confidence interval of the amplitude and depth measurements. Note that (0;0) could be included in this interpolation.

A 2nd order polynomial was chosen as the calibration function. This was also because the slit depth – amplitude relationship is likely to be exponential (Equation 3.2), and a higher order polynomial would be unlikely to generalise the data. It is now possible to measure (and monitor) slit depths within the above defined region. The capabilities of the calibration method developed above are discussed in the following section.

5.4.2 Discussion of Calibrated Results

Figure 5.13 shows the accuracy to which straight fronted and thumbnail shaped defect depths may be measured with the calibration function shown in Figure 5.12. The accuracy of these measurements is shown by deviations of the predicted depth from the dotted 100% accuracy line. This shows calibrated peak-to-peak amplitude results from straight

fronted and thumbnail shaped defects. Note that as the system was calibrated to straight fronted defects; these measurements are most accurate, and become progressively more accurate as defect depth increases (bold line). This shows that the smallest detectable defect (at $a = 0.65 \pm 0.15$mm) produced a repeatable error of -0.25mm ($a_{predicted} = 0.4$mm). As this error likely to be predominantly calibration error[60], increasing the number of slit depth data points (enabling a higher order polynomial fit), and increasing the accuracy of the depth measurements by using precision depth measuring instruments would reduce this improve the accuracy of these measurements.

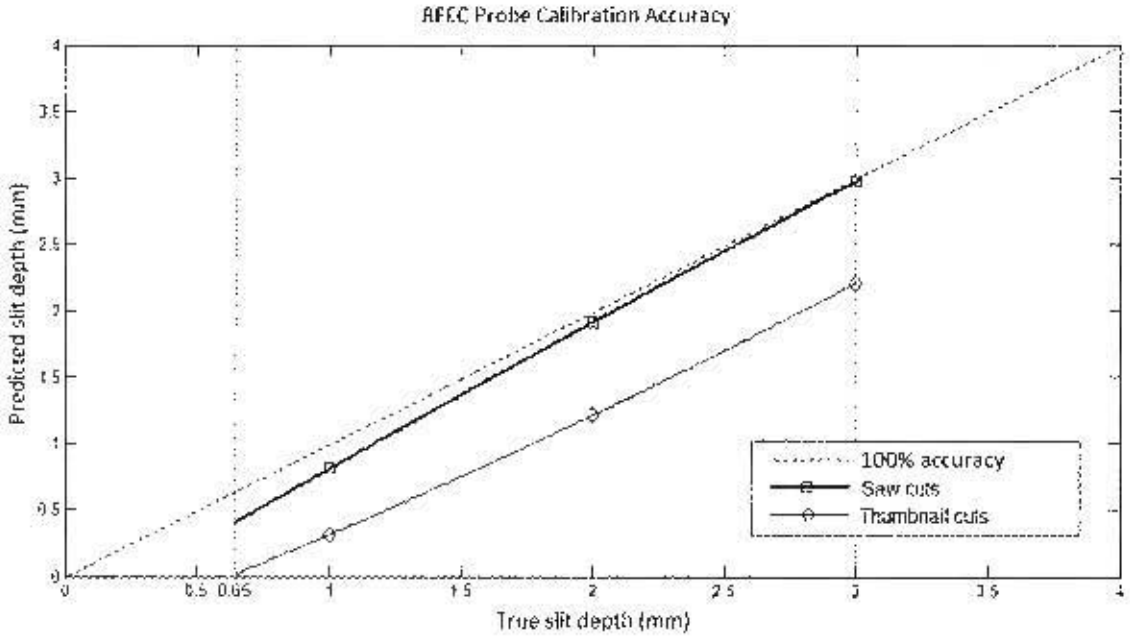

Figure 5.13 – RFEC defect signal calibration accuracy
The calibratable region defined in Figure 5.12 is shown again by vertical dotted lines.

However, the most important result shown in Figure 5.13 is the effect that aspect ratio has on the measurement accuracy as is shown by the thumbnail shaped defect measurements (diamond shaped markers). Comparison of these results with the calibrated straight fronted defect results (square markers) shows an average and relatively constant depth error of -1.8mm. However, these predictability lines are somewhat parallel suggesting that this error may be calibrated out of the system by including $2c$ as a calibration input (i.e. a third axis in Figure 5.12).

[60] All of the calibration parameters (straight fronted defects measured at TDC position) are met in this case.

The calibration was also tested on off-centre defect signals which were shown in the previous section to attenuate very gradually circumferentially away from the TDC position. It was found that RFEC detectors are comparatively insensitive to circumferential variations, to a tolerance of approximately one detector face (±7degrees or ±8mm from TDC – see Appendix F-1). However, as a result, the ability of this calibration method to measure defect length (motivated in the previous paragraph) is not clear. This is discussed further in Section 7.2.

5.5 Summary

The RFEC probe built for this study as outlined in the methodology was tested in this chapter. Firstly, a pilot study was carried out to determine the detectability of circumferential 0.3mm width slit defects. The amplitude component was found to provide the smallest defect detection at a = 0.6mm, but the early defect signals were immersed in a significant background signal. Fortunately the background signal was shown to be highly repeatable enabling the implementation of background signal subtraction. Although excellent results were achieved using a generalized neural network (GRNN), GRNN itself was highly vulnerable to positional errors caused by mechanical hysteresis in the pulley and the position measurement systems (tolerance ±6mm). For this project, these errors were corrected offline using cross-correlation with the background signal as a reference. Both the digital realignment and background signal subtraction became part of a new post-processing stage for subsequent inspections, requiring that background signal inspections be performed prior to defect detection. By subtracting the background signal from the defect signal of the smallest detectable defect, it was shown that sufficient resolution was achieved to validate the 8.3mm/s probe speed estimated in the previous chapter.

Array data was studied from which two main observations were made:

- Defect signals increase monotonically not only as a function of the overall slit depth (at TDC) but also with slit depth along the defect profile (i.e. non-TDC array positions).
- Increase in defect area (or a decrease in aspect ratio at constant depth) affected the overall RFEC defect signal, even at TDC where the defects were the same depth.

For the triangulation of these observations, the peak-to-peak amplitude was calibrated to defect depth. This calibration showed that defects may be monitored between depths of 0.65mm and 3mm (21.6% and 75% wall thickness) with a 95% repeatability of 0.2mm (5% wall thickness). The maximum error was associated with the smallest detectable defect (a_i = 0.65mm) and was 0.25mm. However, this error decreased significantly as defect depth increased. Therefore the defect measurement and monitoring capabilities were most accurate (less than 0.1±0.1mm) between 50% and 75% wall thickness.

By calibrating array results, it was found that the accuracy of the calibration is largely unaffected by circumferential position variations, with a tolerance of approximately one detector face (±8mm from TDC), and that although defect area (associated with defect aspect ratio) had a strong affect on the RFEC defect signal. This effect may be accounted for in the calibration parameters.

This chapter has characterised RFEC defect signals in terms of defect depth by subtracting background signals in the pilot study, defect length by generating RFEC array data, and calibration in order to measure these parameters for Fracture Mechanics evaluation. The next step is to investigate the final defect dimension, defect width. Although this parameter is not represented in the Fracture Mechanics evaluation reviewed in this thesis, Section 3.3 showed that defect width is closely linked to the overall detectability of circumferential fatigue cracks. Therefore the following chapter investigates inspection results from defects of fixed depth and varying widths. As these widths tend to zero, these results are expected be similar to real fatigue cracks. Therefore the aim of the next chapter is to link the saw-cut defect signals of this chapter to drill pipe fatigue crack signals.

CHAPTER 6 FATIGUE CRACK SIMULATION

6.1 Introduction

The literature review consisted of two parts: the practical aspects of RFEC inspection, and the detectability of fatigue cracks (Section 3.3). The practical aspects were addressed from inspection results of saw-cuts of increasing depth in the previous chapter. Therefore this chapter studies the detectability of defects of various widths, specifically the detectability of zero width defects intended to simulate fatigue cracks.

Section 3.3 of the literature review presented finite element simulations which showed that the amplitude of RFEC defect signals from circumferential cracks was largely dependent on defect volume. Hence, very fine circumferential fatigue cracks should result in poor detectability. Therefore this chapter aims to achieve an understanding of the RFEC defect signal amplitude as defect volume tends to zero, as a function of defect width. This data is useful in the context of this report to determine whether fatigue crack signals are sufficiently distinct from background signals to provide reliable and repeatable detection of 'real' fatigue cracks.

As wall thickness is also a major contributor to low amplitude signals in RFEC[61], all the tests in this chapter are carried out in parallel with the same tests on a second pipe of approximately drill pipe thickness (13mm). This was to aid in understanding the effects of wall thickness on defect detectability.

As the time and facilities required to generate real fatigue cracks were not available for this study and it was not possible to machine a defect less than 0.3mm width, it was necessary to explore alternative methods for simulating 'zero-width' defects (fatigue cracks).

[61] This is due to the skin effect at the exciter and the detector illustrated in Figure 3.2.

6.2 Zero-width Defect Simulation

6.2.1 Background on RFEC Defect Simulation

Much work has been done simulating defect field perturbations for a better understanding of the field interactions resulting from various defect morphologies, and mostly simulations are performed with finite element analysis. Regarding fine circumferential cracks, the consensus of this work was that the resulting signal amplitudes would be too small to be detectable experimentally (see Section 3.3 for references). However, these finite element simulation results have been shown to not agree with field results from RFEC tools [84]. Russell NDE Systems Inc. has shown circumferential thermal fatigue defects to be detectable (Figure 3.12).

Atherton and Schmidt showed that external ferromagnetic metal parts containing defects may be used to simulate the presence of an embedded defects when testing ferromagnetic pipe [79,82]. That is, with the placement of rectangular metal bars containing defects on the external surface of the test pipe, the external metal targets behaved magnetically as part of the wave guide. Thus, the magnetic flux path extends through the external metal similarly to the RFEC phenomenon in thicker walled pipe. To the knowledge of the author, no explicit study has been undertaken to examine the equivalence between true embedded defects and embedded defects simulated by external metal targets. However, various findings and theories by Atherton suggest that the electromagnetic field interactions with external metal targets containing defects are similar to interactions with embedded defects in the case where the defect is circumferentially oriented and narrow (as in drill pipe fatigue cracks).

Firstly, it was shown by Atherton that circumferential defects tend not to interact with circumferential eddy current flow generated by RFEC in the remote field zone but rather with the axial magnetic field [50]. This suggests that electrical continuity between the external metal part and the pipe wall is not significant. This result was confirmed experimentally by Atherton [79]. Secondly, similar findings by Atherton suggest that due to the high permeability of ferromagnetic pipe, circumferential defects may be thought of as obstructions to the magnetic flux path similar to the classical definition for magnetic reluctance: easily understandable in terms of external targets interacting with the remote axial magnetic field [81].

For further understanding of the electrical and magnetic interactions, see Atherton's anomalous source defect models [81], summarised in Appendix A-2.

6.2.2 Methodology

Due to significant interaction of circumferential defects with the axial magnetic field of the RFEC method, it was considered important for the cross-sectional area of the external metal target (and pipe wall) to remain constant in the axial direction with the exception of the local discontinuity representing the defect (Figure 6.1).

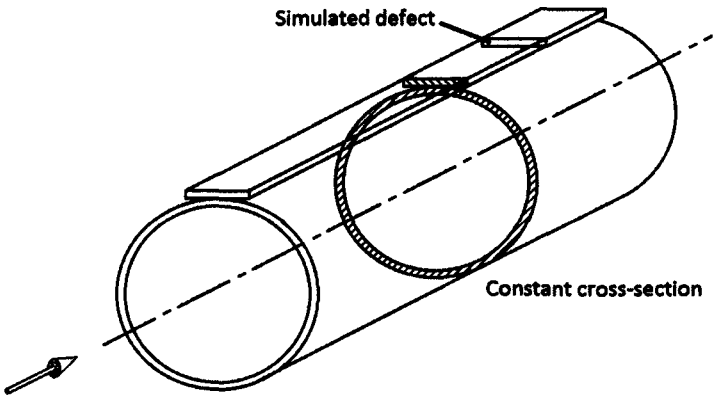

Figure 6.1 – Extraneous metal and pipe showing constant cross-section

A metal bar of approximately the same permeability[62] as both test pipes (test pipe from the previous chapter and the new thick-walled pipe), and long enough to fully span the length of each, was machined in half so that the discontinuity between the two halves could represent a defect of width w, as shown in Figure 6.2. To improve the continuity of contact when $w \cong 0$, the machined faces of the rectangular bars were machine-ground to remove burs and make them flat and square, the surface finish was taken to be less than 0.8μm (BS EN ISO 1302:2002).

It is worth mentioning that the defects machined into the external targets by Atherton and Schmidt did not fully penetrate their external targets while in this setup the external target was machined into two separate parts. This was because it was required in this study to be able to adjust the simulated crack width, w. The advantage of the non-penetrating defects

[62] Magnetic permeability was inferred from the force required to remove a small area magnet from the pipe wall. Calibration of these results showed the method to be effective.

used by Atherton was possibly that electrical eddy current flow is permitted around the defect in the external target, thus making the target a more accurate representation of an embedded defect (as it were; machined into actual pipe wall). However, these effects may be discounted as the eddy current flow tends not to interact with circumferentially oriented planar defects, particularly those in external targets [48].

As axial magnetic field is strongest near the pipe surface [93], the separation between the external metal part and the pipe wall should be considered. The findings of Hoshikawa *et al.* showed that these gaps should be as small as possible; nominally less than[63] 0.04mm [98]. As it was not possible in this project to account for lift-off less than 0.04mm at all points along the test pipe, the magnetic flux path between the exciter and the detector was rigidly fixed. This flux path includes the probe exciter, detector, and the part of the rectangular bar spanning the exciter detector distance, as shown in Figure 6.2 (also represented as the indirect energy flow path in Figure 3.1 and 3.2). The thickness of the bar was chosen to simulate a 50% thickness crack. Therefore, referring to Figure 6.2, t = d = 4mm.

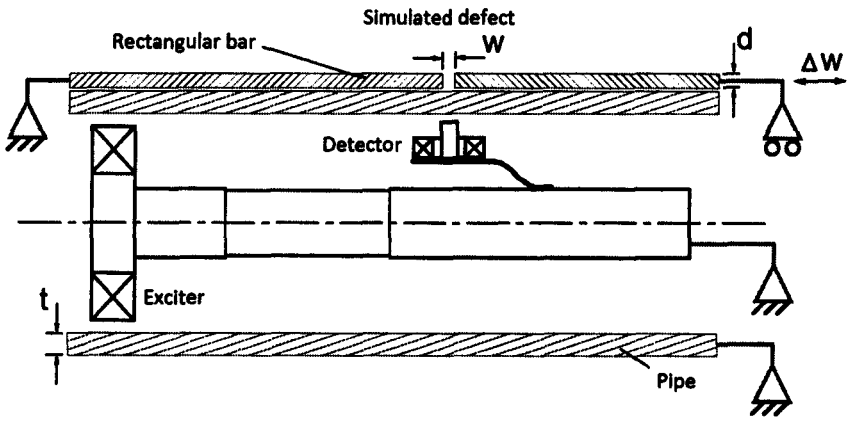

Figure 6.2 – Schematic of the defect simulation method
d=4mm, w=variable and t=4mm (standard pipe) and 13mm (13mm thick pipe), foil end-caps are not shown. Sliding (⏢) and fixed (⏢) components are indicated.

[63] These results originated from an investigation of the feasibility of RFEC for the in-service inspection of double walled tubes; therefore it is again assumed that eddy current interactions are negligible for these two experiments to be analogous.

Note that in order to determine the precise axial location of the simulated defect, the simulated defect (with w set at 0.3mm) was gradually slid axially over the detector until amplitude, measured in real-time, reached a maximum. The external bar between the exciter and the detector was fixed to the pipe wall at this location.

The precision of these results was expected to be significantly improved[64] by only moving the bar outside the exciter - detector flux path. However, this metal bar could not always be fixed as it was also necessary to compare the zero-width result with a 'no defect' case. In order to achieve this comparison, the external metal bar and zero-width defect was slid axially 50mm away from the detector and the exciter in its wooden guide. The simulated defect width was set with a Dieter Schmid feeler gauge (quoted by the manufacturer to be accurate to ±0.005mm)[65].

Note that by the external metal bar being fixed between the exciter and the detector, only one face of the simulated defect could be moved when adjusting w (Figure 6.2). The effect of this asymmetrical widening of the simulated defect was considered insignificant as only simulated widths of less than 0.3mm are important in this chapter (relevance derived from earlier saw-cut results being 0.3mm width). Within this range of widths, a resulting asymmetry was likely to appear small relative to the size of the detector face (axially 8mm).

6.3 Experimental Setup

This section details the setup of the probe to test pipe sections of two wall thicknesses (as mentioned in the introduction). It was necessary to ensure that the RFEC effect can be generated and measured with the current probe in the 13mm thickness pipe. Significantly shorter pipe sections were tested in this section to permit the pipes to be manually moveable. This was acceptable given that the probe position was fixed. However, aluminium foil end-caps (10 layers) were required over the pipe ends to reduce the end effects (inherent in RFEC, particularly in short pipe sections [34]).

[64] The moveable metal bar was beyond the detector (from the exciter) and therefore mostly outside the sphere of influence of the indirect energy flow path.

[65] At this accuracy, misalignments of the sliding bar and foreign particles on the feeler gauge surfaces are more likely sources of error.

Additional pullout tests were required to validate the probe design for the new pipe geometries (13mm thick and using short pipe sections) as shown in Figure 6.3. These results were consistent with previous results and literature showing the transition zone at approximately 2 pipe diameters (dotted line) [99]. As a result, the 2.7 pipe diameter exciter detector distance is shown to also be applicable to 13mm wall thickness pipe tests. The phase trace of the 4mm thick pipe appears to begin at a non-zero position; this 180 degree phase shift is explained by Haugland [67]. The specifications of both pipes are listed in Table 6.1.

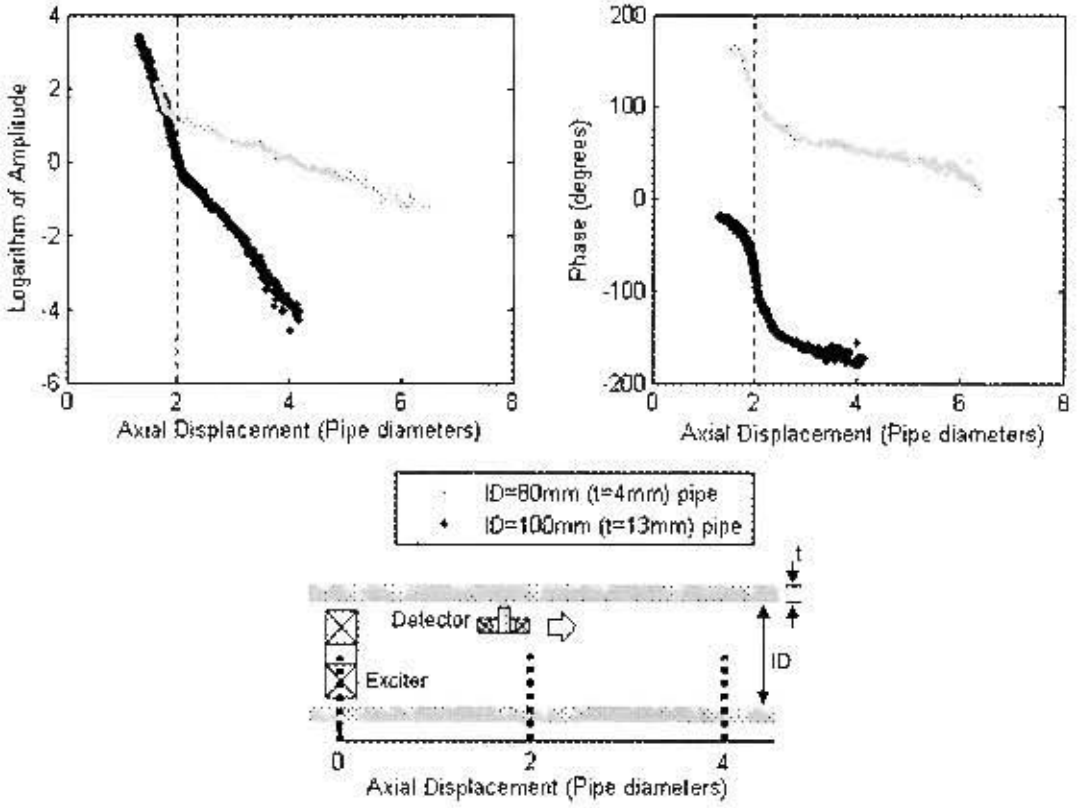

Figure 6.3 Pullout tests to validate the probe design for pipe geometries shown in Table 6.1
Note: The remote field zone (right of the dotted line) and the steeper roll-off for the thickness: t=13mm pipe (black) are shown. A schematic of the pullout test is included below.

To ensure that this test setup conformed to standard RFEC field distributions, the phase results were cross-checked with Equation 3.1 as shown in Table 6.1 (right). The high degree of accuracy was considered to be sufficient validation of the current RFEC probe for testing of both pipe thicknesses.

Table 6.1 – Table of properties including actual and predicted phase results

Steel	Pipe Dimensions		Pipe Electromagnetic Properties			Phase (deg)	
	ID (mm)	thickness (mm)	μ_r (H/m)	Std Deviation (H/m)	Conductivity (S/m) x10^6	Predicted	Actual
S690Q (drill pipe)	500-600	15--5	859.9	4.8	-	-	-
Standard pipe	80	4.0	801.4	6.3	45.2	49.59	50
Thick-walled pipe	100	13.0	911.6	14.3	47	170.98	170

6.4 Simulated Fatigue Crack Results

6.4.1 Field Perturbation Measurements of Simulated Fatigue Cracks

Results were obtained by the square bar faces being clamped at various widths while measurements were taken (Figure 6.4). As previously mentioned, the 'no-defect' measurement was measured at a remote location on the bar to show the difference between a zero-width defect and no defect. The markers are shown with 95% confidence intervals generated from 50 tests taken at each simulated defect width. The figure shows data for both the 13mm thick (squares) and 4mm thick pipe (triangles). Note that the 4mm thick pipe measurements were significantly more pronounced and precise than those from 13mm thick pipe results.

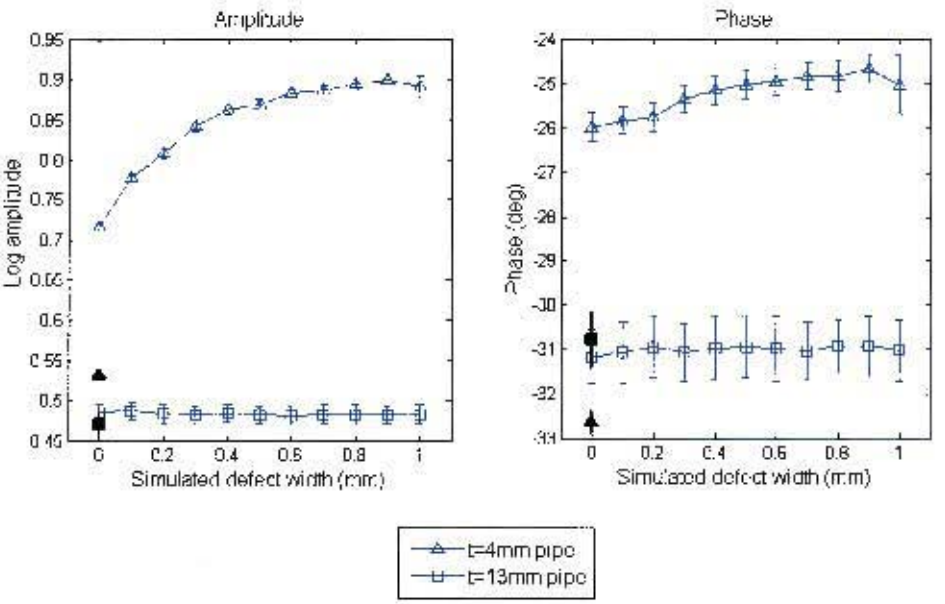

Figure 6.4 – Signal levels showing amplitude and phase separately

Note that solid markers represent a reference 'no-defect' signal for comparison with subsequent simulated defect signals, i.e. background signals. These were achieved by testing defect free areas of the bar.

In terms of assessing the detectability of fatigue cracks, only the data at $w = 0$ is relevant. At this width, there is a both a solid and a clear marker for each of the 4mm and the 13mm pipe tests. As the solid marker is simply a similar measurement taken at a part of the external bar with no defect (a 'no defect' measurement), the difference in amplitude between these two markers at $w = 0$ indicates the net electromagnetic interaction generated by the simulated zero-width defect (clear marker). With a special case of detectability being defined as defect signals which fall outside the confidence band of a set of background signals (no-defect measurements), the 4mm thick pipe results indicate a 100% detectability of the simulated fatigue crack at $w = 0$. Furthermore, a distinct relationship is shown between the amplitude and phase signal components and simulated defect width for all $w \geq 0$. Although this region is not representative of fatigue cracks, data points greater than $w = 0.3$mm are useful for comparison with real embedded defects as widths greater than 0.3mm can be machined and compared to simulated results. This is the basis for the validation of this simulation method carried out in the next section.

Unlike the 4mm thick pipe results, those for the 13mm thick pipe showed significant overlapping of the confidence bands at zero-width indicating approximately 30% detectability (if detectability is as defined above). It was assumed that the defect signals achieved by the 13mm thick pipe were dominated by the skin effects associated with the 3.25 times increase in wall thickness. As these 13mm wall thickness anomalous results are also likely to be a result of hardware sensitivity limitations, these are discussed further in Chapter 7.

As previously emphasised, no explicit study of the equivalence between embedded defects and defects simulated by extraneous metal targets was found. Therefore the validation of these results by comparison with true embedded defects signals is conducted in the next section.

6.4.2 Validation of Results

The aim of this section is to validate the simulated defect results by comparing them with 'real' saw-cut defect results. For consistency, the probe setup, pipe and probe positions, and the observed area of the pipe wall were unchanged between these tests and the previous simulated defect tests. Accordingly, the embedded defects were machined in the

same asymmetrical manner in which the simulated defect width was adjusted[66]. Note that only the 4mm thick pipe could be used for this study as the 13mm thick pipe results were not conclusive. To be consistent with the simulated defect results, the embedded defects were machined to 50% wall thickness (a = 2mm). Embedded (emb) and simulated (sim) defect results are both shown in Figure 6.5 and Figure 6.6.

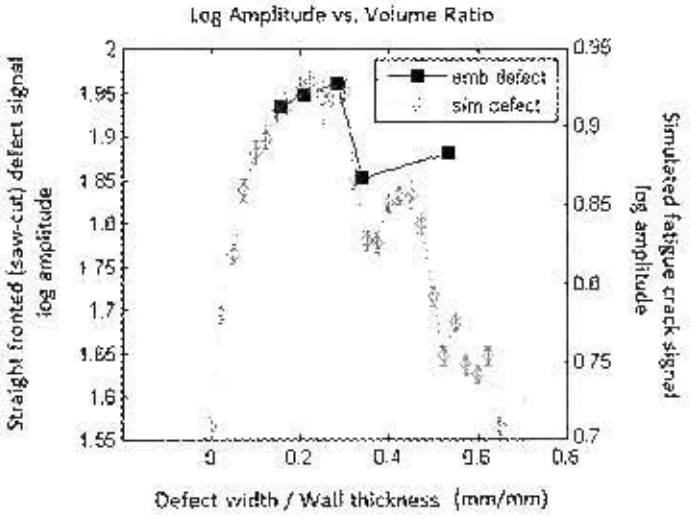

Figure 6.5 – Natural log of amplitude vs. normalised defect width for simulated (sim) test results superimposed on embedded (emb) test results.

Results are normalised to wall thickness where the normalisation of simulated widths included the thickness of the external bar (8mm).

A close fit was achieved by normalising the x-axis of the embedded and simulated defects to their equivalent wall thicknesses. Therefore embedded defect widths were normalised by assuming that the external metal bar was part of the wall thickness (i.e. 8mm thickness). Note that the log of the simulated defect signal amplitude is approximately one decibel less than that of the embedded defect. This suggests that the external metal (t – 4mm) on the test pipe wall (t = 4mm) was interacting with the remote field similarly to contiguous pipe wall of total thickness 8mm (Equation 3.2). Although a similarly close fit was achieved with the corresponding phase results, the vertical offset is not accounted for by skin depth equations:

[66] That is, defect width was only increased by removing material from one defect face to correspond to the fixed simulated defect face shown in Figure 6.2. For this purpose, a metal strip (spring steel) was fixed to the pipe as a saw guide during cutting.

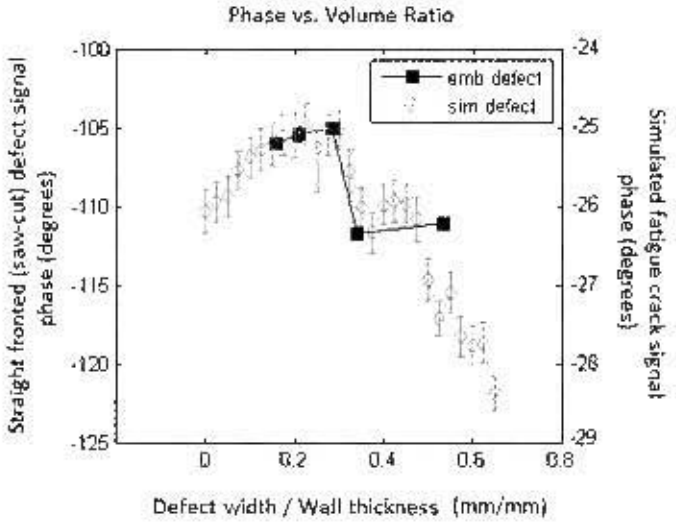

Figure 6.6 – Phase vs. normalised defect width
Normalised to wall thickness for simulated (sim) superimposed on embedded (emb) test results. Normalised simulated widths include the thickness of the external bar (8mm).

Notice that at first these results tend to increase monotonically until a certain width is reached (2.4mm simulated defect width, 1.2mm embedded defect width), after which the amplitude and phase decrease erratically. This was possibly due to off-peak measurements caused by the asymmetrical widening of these defects. This was not investigated further as the validity of the defect simulation method is, prima facie, shown by the close fit between extraneous and embedded defects. It is therefore more relevant to scrutinise the 13mm thickness results (discussed in the following chapter). These equivalence results are discussed further in terms of detectability in Section 7.2.

6.5 Summary

The literature review covered two aspects of RFEC applicable to drill pipe inspection:

- Practical aspects of RFEC inspection
- The detectability of fatigue cracks

The second aspect was dealt with in this chapter. As field testing by Russell NDE Systems Inc. found fatigue cracks to be detectable while FEA simulations did not, an experimental approach was needed.

An experimental method by Atherton and Schmidt generated RFEC defect signals by inspecting defects in separate external metal targets placed on the test pipe wall [79,82]. Their results showed that the received signal was similar to an embedded defect signal and were substantiated by evidence that, due to the dominance of the axial magnetic field interactions over eddy current interactions with embedded defects, the simulation is a particularly accurate representation of circumferentially oriented planar defects. However, due to the requirement of this chapter to vary defect width (and achieve a zero-width defect), the existing simulation method was modified in the following ways:

- As only circumferential defects are tested in this project, the extraneous metal target was made to be continuous between the exciter and the detector to remove end effects from the external metal (in previous tests using this method, the extraneous target only covered pipe wall in vicinity of the detector).
- The separation of the machine ground faces of two rectangular metal bars simulated the defect rather than a single metal part with an embedded defect machined into it as used in previous studies.
- Short pipe lengths were required for testing in this chapter to allow maneuverability.
- The probe was rigidly fixed during testing.

The results showed that simulated zero-width defects were 100% detectable, where detectability was defined by the percentage overlap of the defect data with background 'no defect' data. The same results conducted with 13mm thick pipe were not conclusive. The building and calibration of the probe on the 4mm thick pipe could have contributed to this result: in particular, the magnetic field generated by the exciter coil and the resulting field perturbation of the simulated defect were probably too weak to overcome the 13mm wall thickness due to the skin effect. However, the main result was the clear identification of a zero-width defect in a simulated area of pipe wall.

Thus far, this study has successfully implemented RFEC testing through the design and building of an RFEC probe, and studied the detectability and shape of 0.3mm width saw-

cut defects. As the saw-cuts were only representative of fatigue cracks which in reality are significantly narrower, this chapter contributed significant value to the earlier results by providing evidence that zero-width defect field perturbations are detectable. However, final implementation of RFEC in drill pipes based on these results requires special considerations to account for the scale of the prototype built in this project. Therefore the focus of the next chapter is to discuss the design of a 'to-scale' RFEC NDT system for the inspection of De Beers drill pipes, and demonstrate the effectiveness with which such a system may perform fatigue life predictions with Fracture Mechanics.

CHAPTER 7 DISCUSSION

Before the main points of this project are discussed, it is helpful to review the motivation and objectives of the project introduced in Chapter 1. The project was motivated by costly failures of the De Beers Marine drill pipes due to fatigue cracks. These fatigue cracks are known to be circumferentially oriented and propagate radially inwards from the outer surface of the drill pipe due to cyclic bending stresses induced during operation. Eddy current inspection is an NDT technique highly sensitive to fatigue cracks and requiring no surface preparation making it ideal for drill pipe inspection. However, it is widely known that conventional eddy current methods are not well suited to subsurface detection. This was a key limitation in this project as drill pipe inspection must take place from inside the pipe and detect fatigue cracks on the outer surface[67]. Under these conditions, the primary objectives of this project could be identified as:

(1) The selection of the most applicable deep penetrating eddy current method,

(2) Building an NDT pipe inspection system that employs the chosen method,

(3) Evaluating the detection capabilities of the method.

The RFEC method is well suited to the inspection of pipe geometries as it has approximately equal sensitivity to both internal and external defects and is able to inspect pipes with small diameter variations without the need for sensor lift-off compensation systems. However, literature showed that the detectability of circumferential fatigue cracks with the RFEC method is unclear due to the small interaction of the axial magnetic field with the extremely low defect volume of a fatigue crack. As commercial inspections of fatigue cracks have given positive results, RFEC testing was nonetheless chosen as the NDT technique for this project with the provisory that a 4th objective be appended to the previous three objectives:

(4) Investigate the detectability of circumferential fatigue cracks in ferromagnetic pipe with the RFEC method.

[67] It may be recalled that the outer surface is obstructed by flanges and fittings such that inspection of this surface impractical.

A prototype RFEC system was built and tested in this project, but was scaled down from drill pipe proportions in order for manageable manipulation of the probe and test pipe in a laboratory environment. Therefore a significant topic for discussion is the implications of scaling the prototype up to drill pipe proportions. This is covered in the first section of this discussion and draws mainly on the findings of the RFEC probe design sections: Chapter 4 and Section 5.2 - the pilot study (addressing objectives (1), (2) and (3)).

The sections which follow discuss the detection results of this report, namely, the capabilities of the RFEC system for the detection and monitoring of drill pipe fatigue crack growth. Therefore it is necessary to revisit the assumptions of the fatigue crack simulation chapter in order to validate these results. Note that this part of the discussion mainly addresses the 4th objective. As the fatigue crack detection and monitoring capability is mainly required to facilitate subsequent drill pipe fatigue life calculations, the final section of this chapter contains an evaluation of the current RFEC NDT system for fatigue life prediction.

7.1 Practical Implications of RFEC in Marine Drill Pipes

The probe built for this study was designed for the inspection of an 81mm ID, 2.1m length and 4mm thickness pipe, while the drill pipe used by De Beers is 500mm ID, approximately 200m in length and 15mm wall thickness. Therefore it is of primary importance to discuss the scaling of the RFEC probe prototype built in this project up to drill pipe proportions. Note that this section does not discuss the scaling of saw-cuts to fatigue cracks and test pipe wall thickness to drill pipe wall thickness as these parameters were studied in relation to detectability rather than probe design. These considerations are dealt with separately in the Section 7.2.

7.1.1 Drill pipe RFEC probe design

A drill pipe RFEC probe would require a large circumferential array of detectors and an exciter fill-factor of at least 75%, as discussed in Section 3.2. The saw-cut inspection results and various other sources [44,48,76], show that the positional tolerances of the exciter are considerably more relaxed than those of the detector. Therefore the design of the detector array is a likely first step in the design of a scale RFEC probe. Detector position considerations include determining circumferential detector spacing, the absolute

axial position of the detector, and the axial separation of the circumferential detector from the exciter. These requirements are discussed here in detail. Note that, as lift-off effects were not noticed in any of the results of this project, and as these are widely accepted to be minimal in RFEC (Section 3.2), only lateral detector spacing is discussed.

The axial distance of the detector from the exciter coil may be determined experimentally via pullout tests, as detailed in Section 4.4.1 and 6.3. A safe separation distance was found to be 2.7 pipe diameters. However, it should be noted that wall thickness was shown to be proportional to the roll-off in the remote field zone such that thicker pipe wall may require a smaller exciter detector separation for sufficient signal amplitudes to perform accurate measurements (Figure 6.3). Defect measurement accuracy, which is a function of the number of detectors in the circumferential detector array and the circumferential extent of the defect signal, is discussed below.

The array results from Chapter 5 suggest that; due to the wide circumferential spread of defect signals, adjacent detectors may be circumferentially separated by up to 20mm with less than 5% wall thickness errors in these defect measurements (from defect TDC). As the circumferential positional tolerance is presumably also a function of the sensor size, a normalised expression of this tolerance would be approximately one detector diameter (±8mm in this project). Therefore a drill pipe ID of 500mm should be inspected by an array of at least 56 evenly spaced detectors to achieve less than 5% wall thickness defect depth measurement accuracy. As drill pipe is more than three times the thickness of the pipe tested in this project and the spreading of the field from a remote defect is correspondingly greater, this estimate is likely to be conservative (i.e. fewer detectors should be sufficient). Note that the wide circumferential spreading of defect signals also allows the possibility of decreasing the probability of missing a defect by measuring a single defect with multiple detectors.

Thus far, the axial and circumferential positions of the detectors relative to the exciter have been discussed. In this project, the positional accuracy with reference to the pipe wall was also important due to the use of pre-recorded data for background subtraction. It may be recalled that this was originally based on the decision to perform inspections in absolute mode (i.e. a single detector coil – see Section 5.2.1). Therefore discussion of axial positional accuracy centres on the choice of detector – absolute or differential.

The RFEC probe had differential and absolute mode inspection capabilities. This project used absolute mode (a single detector coil) due to the excellent repeatability achievable with this detector type (Appendix E-1). However, a possible advantage of differential detectors is that they are able to achieve inline background signal subtraction with zero computational expense. This is often desirable on autonomous platforms with limited data storage or data processing capabilities [77]. However, there are two important considerations when applying differential detectors. Firstly, wall thickness data is lost with this detector type[68]; this data may be useful as wall thickness is a primary factor in the operational and fatigue life of the De Beers drill pipes. Secondly, differential detectors are fundamentally unable to discriminate between gradual defect signals (such as a long axial fatigue crack) and background signals (shown to be due to pipe microstructure) if these are a similar shape. This is especially relevant given that the results of the pilot study showed that the early defect signals (e.g. from smallest detectable defect) are a similar shape to the background signals. The smallest detectable defect and background signal (inset) are redrawn in Figure 7.1.

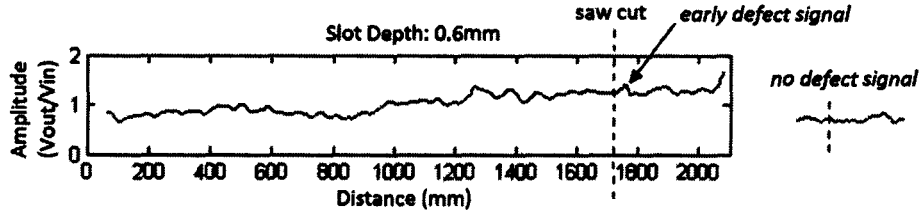

Figure 7.1 – Similarities between early defect signals and background signals

Fortunately, drill pipe RFEC inspection history is likely to be available due to the regular inspections required to monitor fatigue crack progress. Therefore the implementation of background signal subtraction is feasible in a drill pipe implantation of this system, albeit requiring additional data storage and computational capacity. However, these costs are presumably outweighed by the versatility of background subtraction mainly due to the optimiseable smoothing parameter provided by GRNN (Section 5.2.2). The drawback of using background signal subtraction was that it was highly vulnerable to small axial misalignments (estimated tolerance: ±2mm, or a quarter of an effective detector

[68] A single differential detector is actually comprised of two detectors observing adjacent areas of pipe wall. The differential of these two signals is then used to indicate flaws. The rejection of signals common to both detectors is used to improve the probes sensitivity to localised field perturbations. A single differential detector is implemented by placing each detector in series with ground and the each of the positive and negative inputs of the a differential amplifier [77].

diameter). In this project, these were caused by positional hysteresis in the pulley system due to sensor measurements taken far away from the probe at the pulley support block; as these effects would compound over large distances and also become susceptible to surges, the axial position should rather be measured as closely as possible to the RFEC detectors in the drill pipe implementation.

7.1.2 Cost of Operations and Probe Speed

The maximum allowable probe speed imposed on the inspections performed in this project was estimated from an axial resolution of dz = 10.3mm and time constant of t = 1.25s using the equation: V_{max} = dz/t = 8.3mm/s (see Section 4.5.1). However, the required probe speed to inspect 200m of drill pipe in an estimated permissible time of 5hrs imposes a minimum probe speed of 11mm/s [5]. Therefore a 2.7mm/s increase in scanning speed is required. This may be achieved by simply reducing the time constant (set to sample 100 periods at 80Hz) by 0.3 seconds (i.e. 75 periods), particularly as the time constant used in this project is clearly conservative when compared to commercial RFEC tools which reportedly inspect at up to 83mm/s [100].

As the reliability of detection is dependent on defect signal resolution and defect signal amplitude, it is relevant that increases in probe speed inherently reduce the achievable defect signal resolution (dz), and to recall that defect signal amplitude was shown by Chapter 6 to be highly dependent on wall thickness and defect size. It is therefore appropriate to discuss methods to increase probe speed without reducing the reliability of detection.

A common method to increase the probe speed in ferromagnetic pipes, especially when inspecting wall thicknesses greater than one standard depth of penetration [34], is to saturate the pipe wall. Cheong *et al.* [23] found that magnetic saturation of the pipe wall at the exciter coil can more than double probe speed by permitting higher drive frequencies. However, it should be noted that full saturation was often not achieved experimentally in large diameter pipes [34].

A second method to increase scanning speed is by increasing the number of axial detector stages (Figure 7.2). The increase in probe speed permissible from each additional detector stage is then simply proportional to the number of axial detector stages used (fundamentally also reducing the signal error[69]) [101].

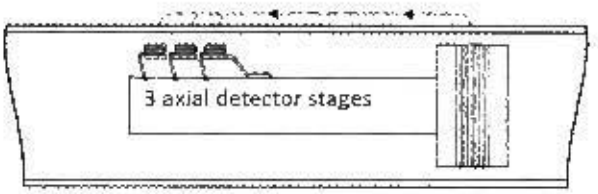

Figure 7.2 – Multiple axial detector stages used to permit increased probe speed without loss of signal quality

It may be recalled that a major assumption used to produce the results discussed above is that the saw-cuts inspected were representative of true fatigue cracks. It is therefore important to understand the detectability of true fatigue cracks.

7.2 Zero-Width Defect Simulation

The results from the defect simulation method tested on 4mm and 13mm wall thickness pipes (referred to as 'thin' and the 'thick' pipes respectively) are discussed in this section. The thin pipe achieved distinct signals and was used to demonstrate the signal amplitudes obtainable from a fatigue crack width discontinuity, and for experimental validation of the defect simulation method with real defects of various widths. The thick pipe tests were intended to relate the thin pipe results to results possible from drill pipe proportions, and therefore contended against the effects of both a low defect volume and more than 3 times the original wall thickness. The conclusive thin pipe results suggested that an electromagnetic interaction exists with the simulated defect. It is important to note that this is not in agreement with finite element analyses reviewed in Chapter 3; therefore the test procedure and assumptions are scrutinised below.

A possible source of error exists in the manner in which the 'no-defect' case was simulated. This step of the simulation is illustrated in Figure 7.3. The figure shows the

[69] Signal error is reduced as a multiple of the signal error-probabilities of each detector.

movement of the external metal bar between the zero-width defect measurement (a) and the 'no defect' measurement (b). An external factor due to the manual movement of the bar between the exciter and the detector is possibly introduced into the detector results due to all of the non-zero width results being generated without any movement of the external metal bar between the exciter and the detector (only the second bar was moved when adjusting w). That is, the entire external bar, containing the zero-width defect, had to be slid away from the exciter to simulate a 'no defect' signal.

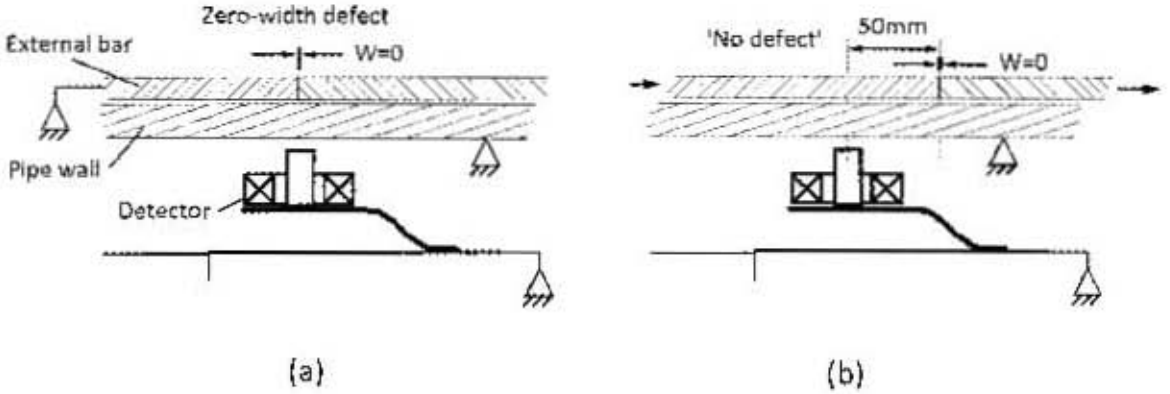

Figure 7.3 – Zero-width defect (a) and 'no defect' (b) cases

As a result, two possible factors may have affected these results:

1.) The background signal of the external metal bar was not measured; therefore the resultant background signal at the detector measured after moving the external bar and within the exciter detector flux path may have varied.

This can be examined by comparing the simulated fatigue crack results (Figure 6.4) with the background signals presented in the pilot study (Figure 5.1 and 5.2 – (a)), as shown in Table 7.1. These values show that the simulated fatigue crack signals are distinct from background signals. Signals from real fatigue cracks are likely to be more distinct than these results suggest as this comparison does not take into account the effective increase in wall thickness caused by the 4mm thick external bar.

Table 7.1 Amplitude and phase perturbations of fatigue cracks compared to background signal

Signal component	Simulated fatigue crack	Background signal
Amplitude (V/Vref)	0.34	0.15
Phase (degrees)	6.5	2

2.) The external metal was located in epoxy guides; therefore the tangential point of contact between the external metal and the pipe wall was subject to the mechanical tolerances of these guides (estimated maximum ±1mm).

However, the circumferential spreading of the field is already shown to permit defect measurement with a circumferential positional tolerance of ±8mm, consequently this effect is likely to be small enough to be neglected.

Therefore it was concluded that a measurable portion of the zero-width defect signal amplitude resulted from direct electromagnetic interaction of the remote field with the atomically narrow interface between the two external metal bars. Combined with evidence of the equivalence of the fatigue crack simulation method of Chapter 6 to saw-cut defects of the type measured in Chapter 5 (Section 6.4.2), it is believed that this signal is similar in amplitude to the signal produced by a true fatigue crack.

The 13mm wall thickness pipe results did not result in sufficient signal amplitude at the detector to permit final discussion of these results (30% overlap in the defect and no-defect signals). As the probe was designed for the 81mm ID 4mm wall thickness pipe, this was expected to be due to the weak exciter field produced by the exciter coil. By comparison of the aspect ratios of the 4mm wall thickness pipe and the drill pipe, it is conceivable that these results are equivalent to detection through a 25mm wall thickness. If correspondingly large field strengths are possible (and the field is proportional to the pipe aspect ratios), sufficient signal amplitudes are likely to be achievable in drill pipe to counter this effect. Based on this assumption, interpretation of these results may be carried out with fatigue life analysis on drill pipe dimensions. The objectives of this project converge in the next section, where the effectiveness of this RFEC inspection system in terms of its fatigue life prediction capabilities is assessed.

7.3 Fracture Mechanics Evaluation

Fracture Mechanics evaluation of the integrity and fatigue life of the De Beers drill pipe requires the solution of Equation 2.7 to estimate the critical flaw size, and Equation 2.10 (reprinted below) to determine the number of cycles until failure. Therefore it is firstly necessary to discuss the accuracy of the inputs to these equations (the first part of this

section) in order to estimate the fatigue life estimation that is achievable by the RFEC method. The calculation of the remaining fatigue life after detecting a defect is useful to determine an acceptable interval for scheduling drill pipe inspections (the second part of this section). Note that these results are calculated mainly to understand the procedure and provide rough estimates for this discussion rather than as a final word on the detectability of fatigue cracks using the RFEC effect. Final accuracy in these predictions would require direct measurements of fatigue cracks from drill pipe with a large scale RFEC probe.

7.3.1 Determination of Fracture Mechanics Parameters

As detailed in Section 2.5, the main inputs required from this NDT system for the Fracture Mechanics evaluation of structural integrity and fatigue life is the length and depth of the flaws detectable in the structure to be evaluated. It may be recalled that these parameters describe the geometric correction factor (Y) which significantly effects subsequent fatigue life predictions (see Equation 2.10). This is illustrated by the bracketed term in Equation 10 (the stress intensity factor, K_I, from Equation 2.7), and noting that m is generally close to 3.

$$N_f = \int_0^{N_f} dN = \int_{a_i}^{a_{crit}} \frac{da}{C(\Delta\sigma Y\sqrt{\pi a})^m} \qquad \text{(Equation 2.10, from pg 34)}$$

Therefore it is helpful to understand the relative importance of parameters a and $2c$ in terms of flaw acceptability. To demonstrate this, the independent effects of a and $2c$ on the stress intensity factor have been studied here. A range of stress intensity factors were calculated by independently varying depth and width from a reference flaw shape of 1mm depth and 8mm width and plotted as shown in Figure 7.4 (stress intensity factors were estimated using the guidelines of BIS PD 6493: 1991 [102]).

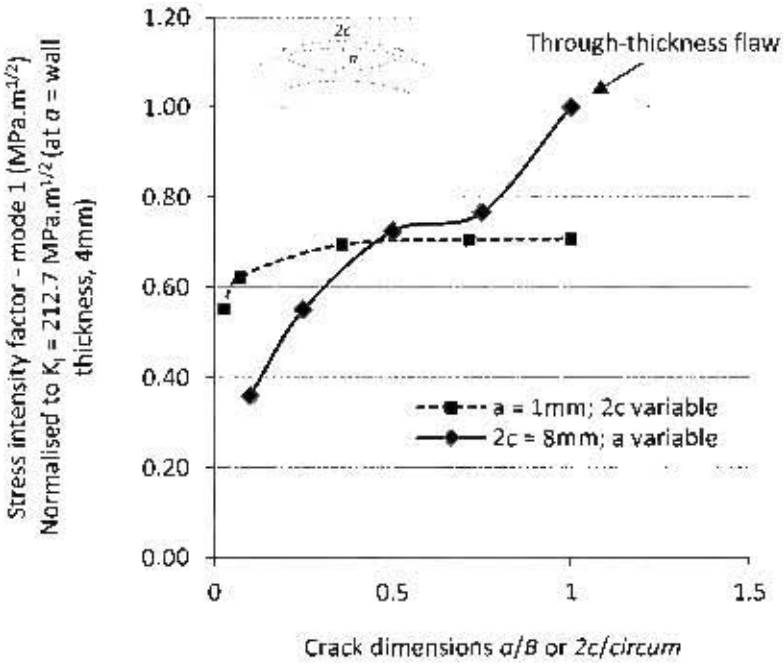

Figure 7.4 – The effect of flaw length ($2c$) and depth (a) on the mode 1 stress intensity factor

Estimations of the applied stress intensity factor assumed an applied stress of 60MPa, see Figure 7.5, and wall thickness B – 4mm, calculated from BS PD 6493 : 1991 assuming level 1 acceptability [102]. Note that a is normalised to wall thickness (B), and $2c$ is normalised to the total pipe circumference (*circum*) and may extend significantly around the pipe (depending on the fatigue loading conditions).

Although the length of a fatigue crack - $2c$ may extend significantly around the circumference of a fatiguing element in rotational bending, it can be seen from Figure 7.3 that in general the effect is less significant on the overall stress intensity factor than the flaw depth a. In particular, it is important that the first detectable defect is as small as possible in order to maximise the permissible margin of error from the subsequent fatigue life prediction. This was found to be a_i = 0.6mm from a straight fronted defect (15% wall thickness) in the 81mm ID pipe tested in this project.

Two effects were identified that may affect this result: firstly, early prediction was only possible by visual or numerical comparison with the background signal measured prior to defect fabrication. Without comparison with pipe history, the first detectable defect would increase to approximately 50% wall thickness (visual assessment of Figure 5.1). Secondly, comparison of straight fronted and thumbnail shaped slits showed that the flaw aspect ratio may cause depth measurement errors of approximately 30% of the wall thickness. This was mainly because the calibration in this project was not designed to account for aspect ratio variations. Therefore, although $2c$ is not a critical measurement

on its own (Figure 7.4), it is clearly indirectly necessary to calculate the aspect ratio, and by calibration, validate crack depth measurements. The sources of error that emerged during inspection and calibration are listed in Table 7.1; the most relevant sources of error (discussed above) are starred.

Table 7.2 – Defect depth measurement errors

1st detection		***a* (mm)**	**% wall thickness**
Amplitude component 1st detection		0.6	15.0%
Amplitude without background subtraction *		2	50.0%*
Phase component 1st detection		2.7	68.0%
Calibration error	**Description**		
Signal error	95% standard dev. of the amplitude signal	0.2	0.1%
Fitting error	2nd order polynomial fit	0.25	6.0%
Aspect ratio*	Straight = 0.108, thumbnail = 0.074	1.8	30.0%*
Off-set detector error	Circumferential misalignment of 8mm from TDC	0.4	0.1%
	Total calibration error (RMS)	**0.94**	**23.5%**

Recall that the first detection achieved by the signal phase component may be ignored due to prior detection with the amplitude component.

7.3.2 Fatigue Life Prediction

The parameter required for fatigue life prediction which has not yet been verified is the nominal applied stress perpendicular to the crack plane. These values were determined in a study by CRS, a company contracted by De Beers Marine to determine the operational stresses in the drill pipes, as shown in Figure 7.5 [7]. Stress measurements were calculated from strain gauges at nominal depths of 60 and 120m (Pods 1 and 2). This study showed that the cyclic bending stresses resulting from 'smooth' operation (i.e. cyclic bending due to ocean currents etc) are dominated by random extraneous stresses (indicated).

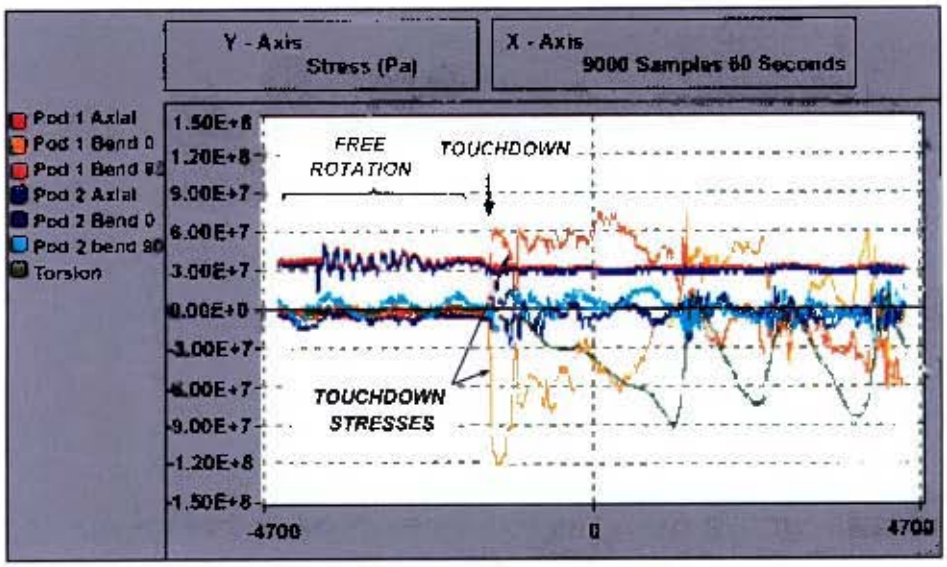

Figure 7.5 – Real time axial, bending and torsional stress data measured on the upper (Pod 1) and lower (Pod 2) positions on the drill string (Press and Tait [7]).

These extraneous stresses are reportedly a function of wave parameters (slamming of the drill string), sea-bed morphologies, and the type of sea bed material in contact with the drill head: when the drill head becomes stuck on the ocean floor, the drill string winds up until the torque is sufficient to 'break' the drill head loose. As fatigue life prediction is highly dependent on the loading conditions, it is clear that accurate estimation of the crack growth rate is not possible with the currently available data. However, hopefully correlation with the crack detection system proposed in this project would improve the understanding of these stresses by initially monitoring the growth rate and associated stresses very closely. For the purposes of discussion, a rough estimate of the fatigue life is calculated from: the results of this project, the accuracy and detectability limits of the RFEC probe discussed in the previous section, and drill pipe stress data from CRS.

All further discussion assumes a 500mm bore drill pipe and a worst case of a worn down wall thickness from 15mm to 10mm, i.e. toward the end of the drill pipes operational life [5]. The initial (first detectable) crack depth and final crack depth to cause fast fracture of the drill string are discussed below.

The validation of the simulated fatigue crack results suggested that saw-cut signals are larger than fatigue crack signals by a factor of approximately 4 ($ln(0.72) - ln(0.54)$, see Figure 6.5). Therefore if the smallest detectable saw-cut was a_i = 0.6mm, the smallest fatigue crack is assumed to be detectable at a_i = 2.4mm, where it is presupposed the

correspondingly large exciter coil and field strengths are sufficient to counter the effects of wall thickness.

The fracture toughness, K_{Ic} of the drill pipe is approximately 82MPa.m$^{1/2}$ [5]. Assuming Y=1.143 [102], and the maximum stress is approximately 120MPa (Figure 7.4), the final defect depth may be calculated from Equation 2.7 as a_{crit} = 130mm. Note that depth is measured circumferentially when its predicted value exceeds the wall thickness. Therefore the pipe will be breached before failure and the crack will propagate circumferentially 130mm symmetrically from the TDC position ($2c$ = 260mm). As the geometry correction factor changes when the crack breaches the pipe wall (assumed to be unity for through-thickness cracks [102]), this calculation is split into two parts: cycles occurring prior to and after the fatigue crack breaches the pipe wall; cases 1 and 2 respectively. These correction factors and the other parameters required are listed in Table 7.3.

Table 7.3 – Fatigue life prediction parameters

Stress intensity factor (KIC) of drill pipe – 82MPa.m1/2		
Maximum stress cycle[70] = 120MPa		
Estimated maximum stress cycles per minute[70] = 5		
Paris equation parameter	**Case 1** ***Until breach***	**Case 2** ***After breach***
Geometry correction factor - Y	1.14	1
First crack depth detected - ai (mm)	2.4	10
Critical crack depth - ac (mm)[71]	10	130
M[72]	3.3	
C[72]	3.982e-12	
Approximate cycles to failure:	**213 000**	**130 000**

The number of cycles until failure may then be calculated by substitution and integration of Equation 2.10 (also in Table 7.3). This gave 1 month until breaching the drill pipe wall and approximately 2½ weeks until catastrophic fracture. However, a more conservative estimation should take into account certain of the errors listed in Table 7.2. This includes

[70] From Figure 7.5, note that drill pipe is shown rotating at approximately 10rpm.
[71] Estimated using Equation 2.7
[72] From Carpinteri *et al.* [103]

the calibration error (mostly a function of errors in aspect ratio) and measurements with and without background signal subtraction.

Table 7.4 – Significant RFEC measurement errors

1st detection	Flaw depth (% wall thickness)
Total calibration error	23.5%
Inspection without background subtraction	50%

The accuracy of the current system accounting only for calibration error may be calculated by assuming that fatigue cracks are detected at a_i = 4.75mm (2.4 + 0.235t, Table 7.4). The predicted fatigue life of this initial crack depth in drill pipe is approximately 1 month (1 week to breach and 3 weeks to fast fracture). Otherwise, if background subtraction is not possible, a_i increases to 7.4mm (2.4 + 0.5t, Table 7.4), resulting in less than half a week until breach (with again an additional 3 weeks until fast fracture).

Given that the RFEC system is reliant on background subtraction to be able to reliably detect fatigue cracks before complete wall penetration; little over one month might seem a tight margin. However, this RFEC system was also shown to be capable of significantly higher defect measurement accuracies than were achievable with the current calibration system (due to limited data points – see Figure 5.12) such that these latter predictions are likely to be conservative.

More importantly in terms of costs due to equipment loss, these calculations show that cracks are likely to have fully penetrated the pipe wall for a significant portion of the total fatigue life of a cracked drill pipe. This RFEC equipment displayed a particularly high sensitivity to wall breaking defects; both in the amplitude and the phase components of the defect signal. Therefore very close monitoring should be possible after defects have fully penetrated the pipe wall. In conclusion, it is estimated that a drill pipe scale version of the current system would be likely to detect fatigue cracks in drill pipes from between three and seven weeks prior to fast fracture of the drill string. The above fatigue life estimates are summarised in Table 7.5.

Table 7.5 – Summary of fatigue life estimates

Time until breach	Weeks
Signal error only	3 weeks
Including calibration error	1 week
Including calibration error and no background subtraction	½ week
Time after breach until complete failure of the drill pipe	**2½ weeks**
Estimated total	**1 month**

7.4 Project Summary

This project was motivated by De Beers Marine to develop a system capable of detecting and monitoring circumferential fatigue cracks that otherwise lead to catastrophic failure of the drill string. The eddy current method is a non-contact NDT technique which is highly sensitive to fatigue cracks making it ideal for drill pipe inspection. However, the conventional eddy current method is not feasible for drill pipe inspection as it is typically unable to detect subsurface defects, therefore eddy current inspection of the internal surface will not detect fatigue cracks forming on the outside of the pipe where they naturally form. A literature search identified the RFEC method as highly suitable for the inspection of ferromagnetic drill pipe inspection due to its approximately equal sensitivity to internal and external defects. This motivated the building and testing of an RFEC inspection system.

In this project, an RFEC inspection system was built, the main components being:

- A probe capable of setting up the remote field effect and precision measurements of the remote H-field.
- A system to extract amplitude and phase data from the remote H-field measurements.
- A supporting structure to control probe speed and circumferential position while measuring the probe axial position.
- Separate defect machining apparatus able to machine 0.3mm width thumbnail shaped slits to aid in characterizing fatigue cracks 'grown' from the outside wall, radially inwards.

Typical remote field amplitude and phase results were studied in the pilot study which confirmed that circumferential defects are mainly visible in the amplitude signal component. Due to a generally small defect signal to noise ratio in the amplitude component - by firstly recognising that the major component of the amplitude noise was highly repeatable - a significant achievement of the pilot study was recognising and subtracting the pipe background signal. A generalised neural network was designed to perform the regression of the background signal required to interpolate and subtract new data points. This achieved excellent results by increasing the range of visually discernable detection from 50% to 85% wall thickness (i.e. now able to detect a 15% wall thickness or 0.6mm deep straight fronted slit). Therefore a new digital post-processing stage was developed, featuring digital position realignment using a form of cross-correlation and a tuneable smoothing parameter (to allow optimisation of background signal subtraction to the background signal of the test pipe). These features are believed to be highly applicable to drill pipe inspection, particularly as RFEC pipe history is likely to be available in the drill pipe implementation of this method.

As the intention is to monitor the progression of fatigue crack growth, multiple scans were conducted at various depths to calibrate the probe measurements and show the repeatability of these results. These showed that a highly repeatable exponential relationship existed between the probe defect signals (amplitude component) and defect depth, proving that defect depth may be accurately monitored for at least 60% of the wall thickness with a maximum error of less than 20% wall thickness ($a = 0.6 \pm 0.38$mm). It was also shown that this error reduced dramatically as defect depth increased. As both the defect signal amplitudes (Figure 5.12) and the calibration accuracy (Figure 5.13) were shown to increase exponentially with increasing defect depth, it is thought highly improbable that defects may breach the pipe wall without prior detection.

Instrument calibration also provided useful insight for future implementation of RFEC probe calibration. It was found both that the accuracy of the calibration is relatively immune to detector misalignments in the circumferential direction and that defect signal amplitude has a strong dependence on defect aspect ratio. The latter was expected to be due to interaction with the area of the defect perpendicular to the defect area. Hence defect sizing and monitoring has been achieved and guidelines for robust industrial use are provided.

A novel approach for the simulation of RFEC field perturbations caused by circumferential fatigue cracks (i.e. zero-width defects) was proposed in Chapter 6. The separation of the machined faces of two metal bars aligned axially and located on the outside surface of the test pipe in wooden guides, represented a circumferential planar defect of width equal to this separation distance. Although the relationship between the RFEC signals and defect width could not be fully explained, convincing evidence was provided for the validation of these results by comparing the simulated defect results with true embedded defect results. Therefore the author believes that the experimental approach has shown electromagnetic interactions which could be responsible for the positive inspection results for circumferential fatigue cracks achieved by Russell NDE Systems Inc [84]. Further research is needed to understand why these interactions do not appear in similar FEA studies. Nonetheless, the simulation suggests that 'real' fatigue cracks are indeed detectable at an estimated depth of approximately 0.15% wall thickness (a_i = 2.4mm; assuming a 15mm wall thickness drill pipe). This is believed to prove the capability of the RFEC method in detecting external circumferential fatigue cracks from the pipe interior.

The conclusions are drawn in the following chapter together with additional recommendations for future research. As this thesis is aimed toward a practical solution to an existing problem, a separate section is included with recommendations to aid in the final design of a drill pipe inspection RFEC tool.

CHAPTER 8 CONCLUSIONS AND FUTURE WORK

This project set out to research and develop an eddy current inspection system to detect and monitor the growth of circumferential fatigue cracks propagating from the outside of De Beers drill pipes. The aim was originally to review eddy current methods for the most suitable method, and test the capabilities of that method. Between PEC and RFEC methods, the RFEC method was selected due to its equal sensitivity to internal and external defects. However, the RFEC method required clarification regarding the detectability of fatigue cracks. Therefore an examination of RFEC responses to fatigue defects was appended to the previous aims.

8.1 Summary of Achievements

An RFEC probe and data acquisition testing rig was built and successfully tested on 81mm ID and 4mm wall thickness pipe, inspecting 0.3mm width saw-cuts of various depths. The smallest detectable saw-cut was achieved at a_i = 0.6mm (15% wall thickness) by identifying and eliminating the repeatable component of the RFEC signal found predominantly in the amplitude component. It was shown that, via background subtraction, the RFEC system was able to achieve amplitude and phase measurements of the field perturbations caused by defects in isolation from the background (pipe) signal. This approach was considered to be valid for drill pipe inspection as the pipe history is likely to be available from periodic inspections.

Calibration of array data found that a circumferential tolerance of ±1 detector diameters resulted in a defect depth measurement error of less than 6% wall thickness, the implication being that a relatively sparse circumferential array of at least 56 evenly spaced detectors is required to inspect 500mm ID drill pipe. However, as background subtraction was found highly sensitive to axial position errors; the axial position was required to be accurate to within ±0.25 detector diameters. In practise this was achievable in software by translation of the recorded signal relative to a background signal using cross-correlation.

Repeated depth tests showed that the peak-to-peak amplitude – defect depth relationship was highly repeatable for at least 60% of the wall thickness, where the lower limit was defined by the smallest detectable defect (defined in terms of variance shown in the peak-

to-peak values), and the upper limit was imposed to exclude signal distortion (necessary for fitting accuracy). This enabled calibration of this region.

RFEC signal amplitude was shown to be highly sensitive to defect aspect ratio, amounting to a flaw depth error of approximately 30% wall thickness. It was shown that although accurate *2c* measurement is less critical than the accuracy of *a*; *2c* derives indirect value in determining the defect aspect ratio (*a/2c*), and thereby validating the defect depth measurement.

A novel approach was developed for the simulation of circumferential defects in ferromagnetic pipe wall. The advantage of the method was that, unlike machined defects, defect width could be reversibly adjusted and set to zero (Section 6.2.2). Three defect conditions were measured:

(1) Zero-width ($w = 0$),

(2) Widths greater than zero ($w \geq 0$),

(3) and a special 'no defect' case

RFEC measurements of (1) and (2) were 100% separable from (3), suggesting that circumferential zero-width defects in ferromagnetic pipes were able to produce measureable signals distinct from these associated background/'no defect' signals.

Comparison of these results to 'real' embedded defects (saw-cuts) of equivalent depth (50%), various widths, and measured under the same static conditions showed a close correlation. Although the error resulting from movement of the external bar to simulate a 'no defect' signal was a factor in these results, it concluded that circumferential embedded zero-width defects that are similar to fatigue cracks (by the equivalence mentioned above) are likely to be detectable with this NDT system.

A notable result of this finding is that it is generally not in agreement with similar FEA simulations (only in agreement with field results). Therefore the assumptions of this defect simulation method and the boundary conditions of the FEA simulations should be examined. This is discussed further in the final section.

8.2 Future Work

This section contains two sections:

- Future research – aspects of this research that require clarification or further development.
- RFEC drill pipe implementation – recommendations for the final drill pipe probe design based on the findings in this project.

8.2.1 Future Research

The amplitude of fatigue cracks simulated in this section suggests that true fatigue cracks present measurable amplitudes. This result should be validated with inspection results of real fatigue cracks. As wall thickness is considerably thicker than was tested in this project, and as the thick walled pipe fatigue crack simulation was inconclusive in this study, the fatigue cracks should also be tested in realistic pipe proportions (but with correctly sized exciters – fill factors of at least 75%).

Any measurements taken with an RFEC tool are only as accurate as the calibration method with which it is partnered. The NDT system developed in this thesis was calibrated to a family of defects of constant width, shape and circumferential position, and only used a single input - the peak-to-peak amplitude (A_{pk-pk}) - to determine defect depth (a):

$$a = f(A_{pk-pk})$$

As this was found to be vulnerable to certain of the parameters which were held constant (particularly crack area – discussed in terms of aspect ratio), future calibration schemes should include inputs from multiple detectors of circumferential positions (y), and should be defined in terms of both amplitude (A_{pk-pk}) and phase (φ), in order to account for the aspect ratio ($a/2c$) and its adverse affects on depth measurements:

$$(a, 2c) = f(A_{pk-pk}, \varphi, y)$$

Such a calibration methodology requires a comprehensive study of RFEC defect signal responses from defects of various widths and aspect ratios, such a study should follow the methodology of Rambocus and Tait [97]. If it is shown that defect signals are of the same

highly repeatable shape as appearing in this study, cross-correlation methods could be implemented in placement of the peak-to-peak amplitude signal descriptor used in this thesis, see the work of Bowen and Dadić [104,105].

The calibration system in this study was limited to calibrating defect depths throughout 60% of the wall thickness. This due to first detection taking place at 15% wall thickness and signal distortion beyond 75% wall thickness. This region could be increased by also including the distorted signals typical of defects close to breaching the pipe wall.

It is worth mentioning that the comparison of PEC and RFEC methods at the outset was based on the earlier work which seldom provided data relating to the power specifications of the eddy current tests. For a more accurate comparison of the PEC and RFEC methods, the following parameters should be accounted for:

- The time duration permitted to observe the target,
- The total energy permitted to stimulate the material during this time, i.e. exciter power,
- The bandwidth of both instruments.

If these parameters are equal in both tests, the limitations of the sensitivity of the hardware are likely to play an increasingly dominant role in this comparison.

8.2.2 RFEC Drill Pipe Implementation

An important aspect of drill pipe implementation of RFEC is increasing probe speed. Two methods to achieve this were discussed: saturation, and implementation with multiple axial detector stages. As the focus of this thesis was to improve the repeatability of these results and as full saturation is seldom achieved experimentally [34], the use of multiple axial detector stages is well suited to the requirements of drill pipe implementation with RFEC [101]. However, as the double detector configuration is required to account for the data loss caused by flanges (Figure 3.6), each additional detector stage installed must be mirrored at the second detector array. Fewer stages may be needed if the field strength is sufficient in the remote field zone to provide high signal-to-noise ratios. It is possible to increase field strengths in this case by increasing the attenuation of the direct field. This can be achieved with nonferrous conductive disks perpendicular to the pipe axis as shown in Figure 8.1 [106].

It is worth mentioning that although seawater is conductive (4.8S/m), the conductivity of ferrous pipe is orders of magnitude greater (approximately 10^7S/m). Therefore RFEC inspection of fatigue cracks in offshore structures is not expected to be significantly affected by conductivity across the crack width.

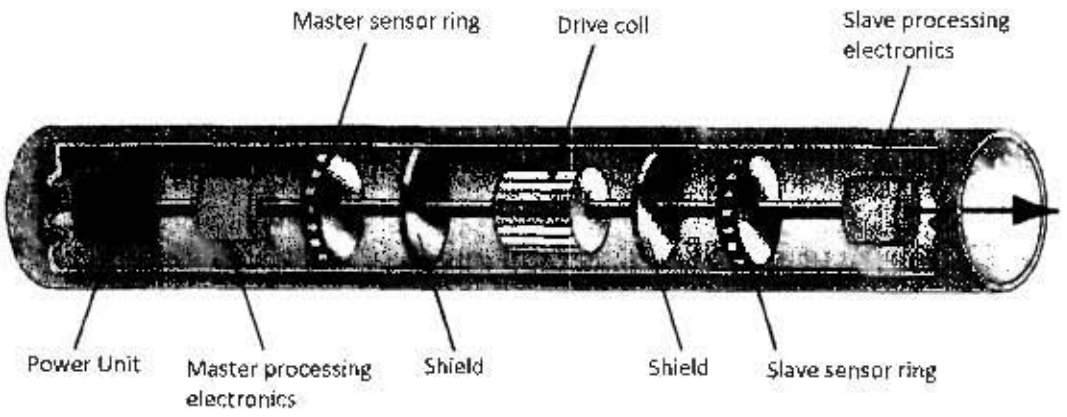

Figure 8.1 RFEC prototype with shielding (Robinson [106])

Improved signal quality was achieved in this project by implementing the signal post-processing offline[73]. The advantage is that by storing 'raw' detector and reference waveforms, the data may be recursively processed, facilitating optimisation of the various post-processing parameters (time constant, smoothing parameter) without data loss. However, as the probe operates over a long distance, this system should be implemented in parallel with real-time processing and viewing of the inspection data. The value of both online and offline processing operating in parallel is that defects missed during real-time inspection can be iteratively searched for with a range of post-processing parameters post inspection.

And finally, as several of the final probe design parameters depend on accurate positional feedback and constant velocity data, a separate tractor module should attach to the probe dedicated to performing these functions. However, such a device is likely to create electromagnetic interference as a result of on board AC motors and their proximity to the sensitive RFEC pre-amplification circuitry. Therefore such a module should either be

[73] This was to avoid the time lag from data handling in Matlab as this tended to result in a significant loss of data (Section 4.4.2).

rigorously electromagnetically insulated or powered hydraulically. It is possible that an inline tractor might be made redundant as the repeating flanges appear as distinct features in the probe signal and may therefore prove useful as waypoints for digital realignment[74], similar to the system used in this project to resolve mechanical hysteresis issues.

[74] Local feature recognition is also possible due to the characterful and repeatable pipe background signal.

REFERENCES

[1] A. Mortimer, "Afri-Can Marine Minerals Corporation," RB Milestone Group, Ohio, eNewsletter, Nov. 2011.

[2] Leia Michele Toovey, "Marine Diamond Mining - Commodities & Futures," *Diamond Investing News*, p. 1, Jan-2011.

[3] Salter Baxter, "De Beers Operating & Financial Review," De Beers Group, London, Financial review, Jan. 2011.

[4] J. Gurney, A. Levinson, and H. Smith, "Marine Mining of Diamonds Off the West Coast of Southern Africa," *Gems & Gemology*, vol. 27, no. 4, pp. 206–219, Jan. 1991.

[5] J. Press (CEO: Origen Engineering Solutions, Cape Town), private communication, 12-Sep-2011.

[6] "De Beers Marine Namibia - The De Beers Group." [Online]. Available: http://www.debeersgroup.com/en/Exploration-and-mining/Mining-operations/De-Beers-Marine-Namibia/. [Accessed: 12-Feb-2011].

[7] R.B. Tait and J. Press, "CRS and De Beers Marine Do It At Depth," *SA Institute of Mechanical Engineering*, vol. 52, pp. 9–10, Mar-2002.

[8] S. Ness, C. N. Sherlock, P. O. Moore, and P. McIntire, *Nondestructive testing handbook: Nondestructive testing overview*, 3rd ed., vol. 10, 15 vols. Ohio: American Society for Nondestructive Testing, 1996.

[9] F. M. Haggag, "In-Situ Nondestructive Measurements of Key Mechanical Properties of Oil and Gas Pipelines," *ASME Publications PVP*, vol. 429, pp. 99–104, Oct. 2001.

[10] K. Newton, Harwell Laboratory, UKAEA, "The transparency of fatigue cracks to NDT methods used for the inspection of offshore structures," presented at the Offshore Europe, Aberdeen, United Kingdom, 1987, vol. 16, p. 18.

[11] J. M. Buckley and H. NDT, "An introduction to Eddy Current Testing theory and technology," Hocking NDT, vol. 8, p. 7, 2003.

[12] D. Lamtenza, G. Washer, and M. Lovez, "Detection and Sizing of Cracks in Structural Steel Using the Eddy Current Method," *US Department of Transportation, Federal Highway Administration*, Report No. FHWA-RD-00-018, pp. 12–25, 2000.

[13] S. Nath, B. Wincheski, J. P. Fulton, and M. Namkung, "Study of the new eddy current non-destructive testing sensor on ferromagnetic materials," *Magnetics, IEEE Transactions on*, vol. 30, no. 6, pp. 4644–4646, Nov. 1994.

[14] G. Mook, "Deep Penetrating Eddy Currents and Probes," *Material Prufung*, vol. 49, no. 5, pp. 258–264, Apr. 2007.

[15] M. F. Kanninen, D. Broek, G. T. Hahn, C. W. Marschall, E. F. Rybicki, and G. M. Wilkowski, "Towards an elastic-plastic fracture mechanics predictive capability for reactor piping," *Nuclear Engineering and Design*, vol. 48, no. 1, pp. 117–134, Jun. 1978.

[16] M. Cortie, J. Mcewan, and D. Enright, "Materials selection in the mining industry: Old issues and new challenges," *Journal of The South African Institute of Mining and Metallurgy*, vol. 96, no. 4, pp. 145–157, 1996.

[17] S. Udpa, and L. Udpa. "Eddy Current Testing-are We at the Limits?" *Proceedings of 16th WCNDT* 3, no. 1 (2004): 1–8.

[18] S. Udpa, and P. O. Moore, *Electromagnetic testing*, 4th ed., vol. 5. Columbus, Ohio: American Society for Nondestructive Testing, 2004.

[19] M. Q. Feng, F. De Flaviis, Y. Kim, and R. DIAZ, "Use of Microwaves for Damage Detection of FRP-Wrapped Concrete Structures," *Journal of Engineering Mechanics*, ASCE, vol. 128, no. 2, pp. 725–729, 2000.

[20] D. Wenxuan, Y. Yating, and X. Lichuan, "Design and implementation of functional measuring circuit for material-independent eddy current sensor," *Mechatronics and Automation*, Takamatsu, 2008, vol. 1, pp. 319–323.

[21] L.F.S.G. Rosado, M.S. Piedade, and P.M.P. Ramos, "Non-Destructive Testing Based on Eddy Currents," MSc Dissertation - Electronics Engineering, Universidade Tecnica de Lisboa, Portugal, 2009.

[22] W. Lord, Y. S. Sun, S. S. Udpa, and S. Nath, "Physics of Remote Field Eddy Current Effect," *Magnetics, IEEE Transactions on*, vol. 24, no. 1, pp. 435 – 438, Jan. 1988.

[23] Y. M. Cheong, "Remote Field Eddy Current Testing," *KAERI*, vol. 1, no. 1, p. 65, Oct. 2001.

[24] "Principles of Eddy Current Testing," GE Inspection Technologies, 50 Industrial Park Road, Lewistown, PA 17044, United States, Wall-Chart, 2005.

[25] T. Stepinski, "Essential Parameters in Eddy Current Inspection," *Swedish Nuclear Power Inspectorate (SKI)*, vol. 3, no. SKI Project Number 97038, pp. 2–7, May 2000.

[26] R. Grimberg, A. Savin, R. Steigmann, S. Leitoiu, M. Ruch, J. Fava, and G. Domizzi, "Eddy current evaluation of pressure tubes from PHWR CANDU type," presented at the IV Conferencia Panamericana de END, Buenos Aires, 2007, vol. 1, pp. 1–14.

[27] J. M. Barsom and S. T. Rolfe, *Fracture and fatigue control in structures: applications of fracture mechanics*, 3rd ed. U.S.A: ASTM International, 1999.

[28] Leclerc, R., and R. Samson. "Eddy Current Array Probes for Aircraft Applications." 16:364–372. Rome: WCNDT, 2000.

[29] Y. Li, T. Theodoulidis, and G. Y. Tian, "Magnetic Field-Based Eddy-Current Modeling for Multilayered Specimens," *IEEE Trans. Magn.*, vol. 43, no. 11, pp. 4010–4015, Nov. 2007.

[30] B. Helifa, A. Oulhadj, A. Benbelghit, I. K. Lefkaier, F. Boubenider, and D. Boutassouna, "Detection and measurement of surface cracks in ferromagnetic materials using eddy current testing," *NDT & E International*, vol. 39, no. 5, pp. 384–390, Jul. 2006.

[31] R. J. Davis and D. T. Hayford, "Low Frequency Eddy Currents with Magnetic Saturation for In-Line Detection and Sizing of Stress Corrosion Cracks," *Review of Progress in Quantitative Nondestructive Evaluation.*, vol. 14, pp. 323–330, 1994.

[32] M. S. C. Bose, "A study of fatigue in ferromagnetic materials using a magnetic hysteresis technique," *NDT International*, vol. 19, no. 2, pp. 83–87, Apr. 1986.

[33] R. Kenton, "A solution to the permeability and lift-off problems in electromagnetic flaw detection - (Magnetic and nonmagnetic metals flaw detection, using orthogonal eddy current probe to reduce permeability and conductivity variations effects)," *NASA SBIR & STTR*, vol. 33, no. 4, pp. 122–135, 1970.

[34] D. L. Atherton, W. Czura, T. R. Schmidt, S. Sullivan, and C. Toal, "Use of magnetically-saturated regions in remote field eddy current tools," *J Nondestruct Eval*, vol. 8, no. 1, pp. 37–43, Mar. 1989.

[35] Y. Sun, T. Ouyang, J. Xu, and J. Long, "Crack Detection in Aircraft Fastener Holes Using Flat Geometry Remote Field Eddy Current Technique and Super Sensitive Eddy Current System," *Electromagnetic nondestructive evaluation (IX)*, vol. 25, p. 229, 2005.

[36] U. Godbole, "A Trio of Techniques for Eddy Current Inspection of Tubes and Bars," in *14th International Conference on NDT*, Chania, Crete-Greece, 2007, vol. 1, pp. 1–6.

[37] T. O'Brien and D. Kunerth, "Pulsed eddy current thickness measurements of transuranic waste containers," Idaho National Engineering Lab., Idaho, U.S.A, OSTI 951091-12, 1995.

[38] G. Jun-zhe, P. Meng-chun, and L. Fei-lu, "Designation and Implementation of Tube Test System Based on Multi-Frequency Eddy Current," in *Intelligent Systems and Applications*, 2009. ISA 2009. International Workshop on, pp. 1–4.

[39] Y. Sun, W. C. Loo, D. C. Kunerth, and T. K. O'Brien, "Finite element simulation of pulsed remote field eddy current phenomenon," Plenum Publishing Corp., *Review of Progress in Quantitative Nondestructive Evaluation.*, vol. 17, pp. 259–266, 1998.

[40] S. Giguere, B. Lepine, and J. Dubois, "Pulsed eddy current technology: characterizing material loss with gap and lift-off variations," *Research in Nondestructive Evaluation*, vol. 13, no. 3, pp. 119–129, 2001.

[41] D. Vasic, V. Bilas, and D. Ambrus, "Pulsed eddy-current nondestructive testing of ferromagnetic tubes," *Instrumentation and Measurement, IEEE Transactions on*, vol. 53, no. 4, pp. 1289–1294, 2004.

[42] G. Y. Tian, A. Sophian, D. Taylor, and J. Rudlin, "Multiple sensors on pulsed eddy-current detection for 3-D subsurface crack assessment," *Sensors Journal*, IEEE, vol. 5, no. 1, pp. 90–96, 2005.

[43] A. Sophian, G. Y. Tian, D. Taylor, and J. Rudlin, "A feature extraction technique based on principal component analysis for pulsed eddy current NDT," *NDT & E International*, vol. 36, no. 1, pp. 37–41, 2003.

[44] Udpa S, Satish S, and O'Moore P. *Electromagnetic Testing*. Vol. 5. 4th ed. Columbus, Ohio: American Society for Nondestructive Testing, 2004.

[45] L. A. N. Lopez, D. K. . Ting, and B. R. Upadhyaya, "Eddy-Current Signal Interpretation Using Fuzzy Logic Artificial Intelligence Technique," presented at the IV Conferencia Panamericana de END, Buenos Aires, 2007, vol. 1, pp. 1–7.

[46] J. Grman, R. Ravas, and L. Syrová, "Application of neural networks in multifrequency eddy-current testing," *Measurement Science Review*, vol. 1, no. 1, pp. 25–28, 2001.

[47] G. Y. Tian, A. Sophian, D. Taylor, and J. Rudlin, "Wavelet-based PCA defect classification and quantification for pulsed eddy current NDT," *Science, Measurement and Technology, IEE Proceedings*, vol. 152, no. 4, pp. 141– 148, Jul. 2005.

[48] D. L. Atherton, "Remote field eddy current inspection," *Magnetics, IEEE Transactions on*, vol. 31, no. 6, pp. 4142–4147, 1995.

[49] H. S. Khatak and Baldev Raj, *Corrosion of Austenitic Stainless Steel: Mechanism, Mitigation and Monitoring*, 1st ed. Indira Gandhi Centre for Atomic Research, India: Woodhead Publishing, 2002.

[50] D. L. Atherton and W. Czura, "Finite element Poynting vector calculations for remote field eddy current inspection of tubes with circumferential slots," *Magnetics, IEEE Transactions on*, vol. 27, no. 5, pp. 3920–3922, 1991.

[51] J. Penman and B. Thian, "Some characteristics of the pulsed eddy-current method for non-destructive evaluation," *Nondestructive Testing and Evaluation*, vol. 6, issue 5, pp. 297-314, vol. 6, pp. 297–314, 1992.

[52] Zhang, Y., "Finite-Element Analysis for Remote Field Eddy Current Responses from Near- and Farside Cracks," *Springer New York*, vol. 10, no. 3, pp. 163 – 169, Nov. 1998.

[53] A. McNab and J. Thomson, "An eddy current array instrument for application on ferritic welds," *NDT & E International*, vol. 28, no. 2, pp. 103–112, Apr. 1995.

[54] B. Ma and D. L. Atherton, "Anomalous magnetic source defect modelling," *Res Nondestr Eval*, vol. 7, no. 1, pp. 1–12, Mar. 1995.

[55] Atherton D, Email Correspondence, 01-Apr-2011. See Appendix B: 2 and 3

[56] Darko Vasić, Vedran Bilas, and Davorin Ambruš, "Pulsed Remote Field Technique in Ferromagnetic Tube Wall Thickness and Inner Diameter Measurement," *XVII IMEKO World Congress Metrology in the 3rd Millennium*, vol. 1, no. TC4, pp. 912–916, Jul. 2003.

[57] M. Chen, Y. Sun, W. Lord, S. Nath, and Y. Shin, "Pulsed RFEC probe response," *Magnetics, IEEE Transactions on*, vol. 28, no. 2, pp. 1430–1433, 1992.

[58] Blitz, Jack. *Electrical and Magnetic Methods of Non-destructive Testing*. 2nd ed. Non-destructive Evaluation. London: Chapman & Hall, 1997.

[59] A. O. Ayhan and U. Yücel, "Stress intensity factor equations for mixed-mode surface and corner cracks in finite-thickness plates subjected to tension loads," *International Journal of Pressure Vessels and Piping*, vol. 88, no. 5–7, pp. 181–188.

[60] P. Paris, M. Gomez, and W. Anderson, "A rational analytic theory of fatigue, The trend in engineering," *University of Washington. Seattle*, vol. 13, no. 1, pp. 9–14, 1961.

[61] D. Broek, *The Practical Use of Fracture Mechanics*, 8th ed. Netherlands: Kluwer Academic Publishers, 1989.

[62] W. R. MacLean, "Apparatus for Magnetically Measuring Thickness of Ferrous Pipes," U.S. Patent 2573799, Nov-1951.

[63] T. R. Schmidt, "Instrument Promises to Permit Measuring Wall Thickness of Pipelines in Place," *Materials Protection*, vol. 2, no. 1, pp. 8–12, 1963.

[64] T. R. Schmidt, "The Casting Inspection Tool - An Instrument for the In-Situ Detection of External Casing Corrosion in Oil Wells," in *Fourth International Offshore Mechanics and Arctic Engineering Symposium*, Dallas, Texas, 1985, vol. 2, pp. 81–85.

[65] D. Russell and V. Shen, "Increased Use of Remote Field Technology for In-Line Inspection of Pipelines Proves the Value of the Technology for this application," Russell N.D.E. Systems Inc., 4909 75 Avenue, Edmonton, Alberta,T6B 2S3, Canada, 2000.

[66] M. Maclean, "Defect characterization by the remote-field eddy current technique in small-diameter tubing," *Mater. Eval.*, vol. 47, no. 1, pp. 24–28, 1989.

[67] S. M. Haugland, "Fundamental analysis of the remote-field eddy-current effect," *Magnetics, IEEE Transactions on*, vol. 32, no. 4, pp. 3195–3211, 1996.

[68] Y. Sun, Jiatun Si, D. Cooley, H. C. Han, S. Udpa, W. Lord, Minxing Qu, Meijuan Chen, and Yang Zhao, "Efforts towards gaining a better understanding of the remote field eddy current phenomenon and expanding its applications," *Magnetics, IEEE Transactions on*, vol. 32, no. 3, pp. 1589–1592, 1996.

[69] W. Lord, Y. S. Sun, S. S. Udpa, and S. Nath, "A finite element study of the remote field eddy current phenomenon," *Magnetics, IEEE Transactions on*, vol. 24, no. 1, pp. 435–438, 1988.

[70] D. L. Atherton, D. D. Mackintosh, S. P. Sullivan, J. Dubois, and T. R. Schmidt, "Remote-field eddy current signal representation," *Materials Evaluation (U.S.A.)*, vol. 51, no. 7, pp. 782–789, Jul. 1993.

[71] J. Makar and R. Desnoyers, "Three dimensional mapping of corrosion pits in cast iron pipe using the remote field effect," in *Underground Infrastructure Research: Municipal, Industrial and Environmental Applications*, 2001, vol. 1, pp. 1–10.

[72] D. L. Atherton and W. Czura, "Remote field eddy current technique: Phantom exciter model calculations," *Research in Nondestructive Evaluation*, vol. 5, no. 2, pp. 123–134, 1993.

[73] S. Smith and D. L. Atherton, "Longitudinal AC interactions with axial slits in steel pipes," *Research in Nondestructive Evaluation*, vol. 7, no. 4, pp. 203–214, Dec. 1996.

[74] S. Sullivan, D. L. Atherton, and T. R. Schmidt, "Comparing a one-dimensional skin effect equation with through transmission eddy current phenomena," *Br. J. Non-Destr. Test.*, vol. 32, no. 2, pp. 71–75, 1990.

[75] D. D. Mackintosh, D. L. Atherton, and S. P. Sullivan, "Remote-field eddy current signal analysis in small-bore ferromagnetic tubes," *Materials Evaluation (U.S.A.)*, vol. 51, no. 4, 1993.

[76] A. Teitsma, "Remote Field Eddy Current Inspection of Unpiggable Pipelines," presented at the Pipeline World, Illinois, 2005, vol. 1, pp. 1–12.

[77] D. Kim, L. Udpa, and S. Udpa, "Remote field eddy current testing for detection of stress corrosion cracks in gas transmission pipelines," *Materials Letters*, vol. 58, no. 15, pp. 2102–2104, Jun. 2004.

[78] Yu Shi Sun, He Yun Lin, Mei Juan Chen, Chun De Wang, Xiao Bing Wu, D. L. Atherton, and T. R. Schmidt, "Finite element modelling and physics of remote field eddy current responses for axially aligned cracks," *Magnetics, IEEE Transactions on*, vol. 28, no. 4, pp. 1941–1947, 1992.

[79] D. L. Atherton, C. J. Toal, and T. R. Schmidt, "Investigations of the remote field eddy current technique in large diameter pipeline," *Br. J. Non-Destr. Test.*, vol. 31, no. 9, pp. 485–488, 1989.

[80] A. Shatat and D. L. Atherton, "Remote field eddy current inspection of support plate fretting wear," *Materials Evaluation*, vol. 55, no. 3, pp. 361–366, Mar. 1997.

[81] D. L. Atherton and B. J. Mergelas, *Anomalous Models of Defect Interactions in Electromagnetic Testing*, 1st ed., vol. 7, 12 vols. Ontario: Nondestructive Evaluation, 1995.

[82] T. R. Schmidt, "The remote field eddy current inspection technique," *Materials Evaluation*, vol. 42, no. 2, pp. 225–230, 1984.

[83] T. A. Bubenik, J. B. Nestleroth, R. J. Davis, B. Leis, R. B. Francini, S. Udpa, and M. A. K. Afzal, *In-line inspection technologies for mechanical damage and SCC in pipelines - final report*, US Department of Transportation, Office of Pipeline Safety. June, 2000.

[84] Ankit Vajpayee, Email Correspondence, 21-Apr-2011. See Appendix B-1

[85] D. L. Atherton, L. Clapham, W. Czura, S. Leonard, B. J. Mergelas, and Y. Zhang, "Finite-element calculations of remote field eddy current interactions with slit defects," *Research in Nondestructive Evaluation*, vol. 8, no. 4, pp. 199–231, Dec. 1996.

[86] J. M. Papazian, J. Nardiello, R. P. Silberstein, G. Welsh, D. Grundy, C. Craven, L. Evans, N. Goldfine, J. E. Michaels, T. E. Michaels, Y. Li, and C. Laird, "Sensors for monitoring early stage fatigue cracking," *International Journal of Fatigue*, vol. 29, no. 9–11, pp. 1668–1680.

[87] V. Zilberstein, K. Walrath, D. Grundy, D. Schlicker, N. Goldfine, E. Abramovici, and T. Yentzer, "MWM eddy-current arrays for crack initiation and growth monitoring," *International Journal of Fatigue*, vol. 25, no. 9–11, pp. 1147–1155.

[88] D. L. Atherton and V. Ton, "The effects of stress on a ferromagnet on a minor hysteresis loop," *Magnetics, IEEE Transactions on*, vol. 26, no. 3, pp. 1153–1156, 1990.

[89] Z. Chen and K. Miya, "A new approach for optimal design of Eddy Current Testing probes," *Journal of Nondestructive Evaluation*, vol. 17, no. 3, pp. 105–116, Sep. 1998.

[90] Y. Sun, *Electromagnetic-field-focusing remote-field eddy-current probe system and method for inspecting anomalies in conducting plates*, 14th ed., vol. 20. Amer, Iowa: American Institute of Physics, 2000.

[91] C. E. Shannon, "Communication in the presence of noise," *Proceedings of the IRE*, vol. 37, no. 2, pp. 10–21, 1949.

[92] R. N. Bracewell, "The Fourier Transform and Its Applications," *McGraw-Hill*, pp. 381–390, 1965.

[93] P. A. Ivanov and L. Udpa, "Remote field eddy current probes for the detection of stress corrosion cracking in transmission pipelines," MSc Dissertation - Electronics Engineering, Iowa State University, Ames, Iowa, 2002.

[94] J. Blitz, *Electrical and magnetic methods of non-destructive testing*, 2nd ed. London: Chapman & Hall, 1997.

[95] D. F. Specht, "A general regression neural network," *Neural Networks, IEEE Transactions on*, vol. 2, no. 6, pp. 568–576, 1991.

[96] A. Zaoui, H. Menana, M. Feliachi, and G. Berthiau, "Inverse Problem in Nondestructive Testing Using Arrayed Eddy Current Sensors," *Sensors Journal, IEEE*, vol. 10, no. 9, pp. 8696–8704, Sep. 2010.

[97] Tait RB, Radebe B, and Rambocus O, "Experimental determination of stress intensity factors for thumbnail and crescent moon cracks for round bars in bending and tension," *Fracture 2000: Engineering Failure Analysis*, Dec. 2000.

[98] H. Hoshikawa, K. Koyama, Y. Shindo, and T. Suzuki, "Remote Field Eddy Current Testing of Ferromagnetic Double Wall Tube," *Nondestructive Testing & Evaluation*, vol. 7, no. 1, pp. 337–346, Jun. 1992.

[99] D. L. Atherton and S. Sullivan, "The remote-field through-wall electromagnetic inspection technique for pressure tubes," *Mater. Eval.*, vol. 44, no. 13, pp. 1544–1550, 1986.

[100] Russell, David, and Vincent Shen. *Increased Use of Remote Field Technology for In-Line Inspection of Pipelines Proves the Value of the Technology for This Application.* 4909 75 Avenue, Edmonton, Alberta,T6B 2S3, Canada: Russell N.D.E. Systems Inc., 2000.

[101] Feng Zhao, Jie Liu, Juan Liu, L. Guibas, and J. Reich, "Collaborative signal and information processing: an information-directed approach," *Proceedings of the IEEE*, vol. 91, no. 8, pp. 1199– 1209, Aug. 2003.

[102] "BS PD 6493: Guidance on methods for assessing the acceptability of flaws in fusion welded structures." *British Standards Institution*, 1996.

[103] A. Carpinteri, R. Brighenti, and A. Spagnoli, "Fatigue growth simulation of part-through flaws in thick-walled pipes under rotary bending," *International Journal of Fatigue*, vol. 22, no. 1, pp. 1–9, Jan. 2000.

[104] M. M. Bowen, W. J. Emery, J. L. Wilkin, P. C. Tildesley, I. J. Barton, and R. Knewtson, "Extracting multiyear surface currents from sequential thermal imagery using the maximum cross-correlation technique," *Journal of Atmospheric and Oceanic Technology*, vol. 19, no. 10, pp. 1665–1676, 2002.

[105] M. Dadić, D. Vasić, and V. Bilas, "A system identification approach to the modelling of pulsed eddy-current systems," *NDT & E International*, vol. 38, no. 2, pp. 107–111, 2005.

[106] D. Robinson, "Identification and sizing of defects in metallic pipes by remote field eddy current inspection," *Tunnelling and Underground Space Technology*, vol. 13, pp. 17–27, 1998.

APPENDIX A: TESTING FERROMAGNETIC MATERIALS WITH RFEC

A-1 Magnetic Saturation for RFEC Inspection

As the majority of field attenuation occurs at the exciter and the detector, the use of saturation and low frequencies are often applied to improve the amplitude of the detector field and therefore increase probe frequency and scanning speed. One does not need to saturate the whole pipe between the exciter and the detector, only localised saturated 'windows' at the exciter and detector as shown in [34,79].

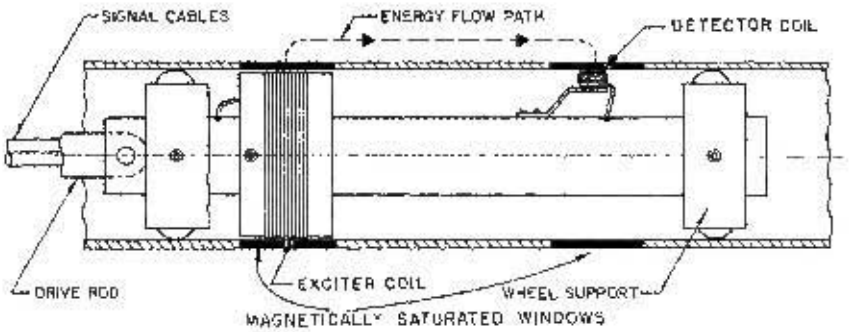

Schematic of a RFEC tool showing saturated 'windows' (black) at the exciter and detector. For simplicity, the permanent magnets and yokes used to saturate the pipe wall are omitted (Atherton and Toal [34])

The high permeability region material between the exciter and the detector is advantageous as it tends to guide the field toward the outer pipe surface, reducing attenuation in the axial direction [34,83]. Though most attempts did not achieve full saturation experimentally [23,34,79,83], a study by Cheong [23] showed that more than double the nominal probe speed is often achievable through saturation of the ferromagnetic pipe wall. It was unclear whether these results were with saturation at both the exciter and the detector; this was assumed to be the case.

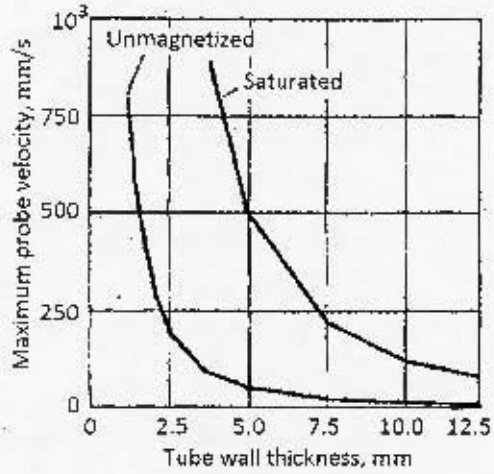

Relationship between maximum probe speed and ferromagnetic tube wall thickness by magnetic saturation (Cheong [23])

It is however important to note that saturation at the detector was in general found not to improve detection of circumferential defects[75] [34].

It is interesting to note that circumferentially oriented slits are highly detectable in ferromagnetic pipes, but axial defects are significantly less so. Also that RFEC detectability is likely to decrease as defect volume tends to zero. Investigation of this critical limitation is covered in the following section.

A-2 RFEC Field Components and Anomalous Source Models

This section reviews two models to assist with the understanding of the electromagnetic field interactions with defects in ferromagnetic pipe. The magnetic field in the remote field zone is predominantly axial; therefore eddy currents tend to form in circumferential current hoops inside the pipe wall in this region [48]. The axial magnetic field and circumferentially flowing eddy currents form the basis for understanding the RFEC sensitivity to planar defects of various orientations. Axially oriented planar defects tend to block circumferentially flowing eddy currents, and circumferential planar defects tend to block the axial magnetic field. As circumferentially oriented defects are detected by magnetic interactions, it is related to defect volume and the magnetic permeability of the material. Note that as a result, RFEC is most sensitive to circumferential defects in ferromagnetic pipe material. Conversely, the tendency for circumferential eddy currents

[75] Despite this, the detectability of adjacent cracks was noted to improve due to the field lines 'clinging' to the surfaces of the defect when testing in high permeability materials [85].

to interact with axially oriented defects implies that axial defects are best detected in non-ferrous materials [48].

These two mechanisms for defect detection can be described as the anomalous electromagnetic sources shown by phasor vector subtraction of the defect (b) and defect free (a) electrical and magnetic field patterns [54].

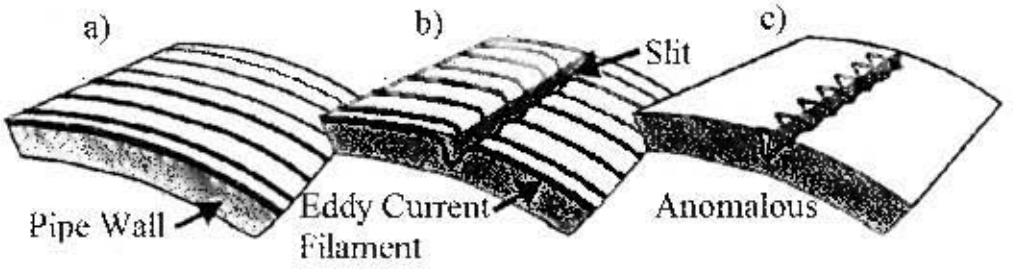

Eddy current filaments in a defect free pipe wall (a), showing filament interaction with an axial slit (b) and the anomalous illustration generated from the defect and defect free cases (c) (Atherton [48])

These models separately consider the magnetic and electric field interactions as described above. The first interaction considered here the model for non-ferromagnetic materials. This anomalous model recognizes that circumferential eddy current interactions dominate. Therefore planar defects must have some axial component to be described by this model. The perturbation of the electric field is described by decomposing the eddy current flowing around the crack face into a component diverted beneath the non-penetrating slit (a) and a surface component which tends to form current whorls as it is diverted around the edges of the crack (b) [54].

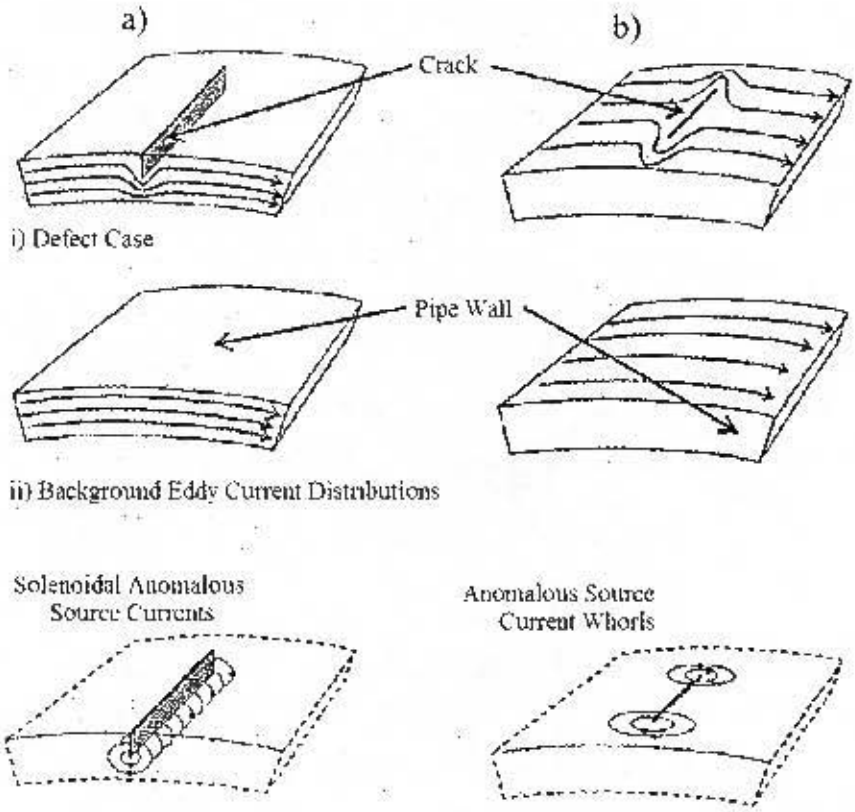

Anomalous eddy current defect sources (Atherton [48])

Note that sources are decomposed into (a) eddy currents which dive beneath a non-penetrating slit (solenoidal current source) and (b) eddy currents diverted around the ends of the slit (current whorls).

In ferromagnetic pipes, the axial magnetic field is magnified such that RFEC inspections are more sensitive to circumferentially oriented planar defects. The same process of phasor vector subtraction may be applied to the axial magnetic fields in the pipe wall, that is, the background magnetic field (a) is subtracted from the defect case (b) to produce the anomalous magnetic source (c) shown below:

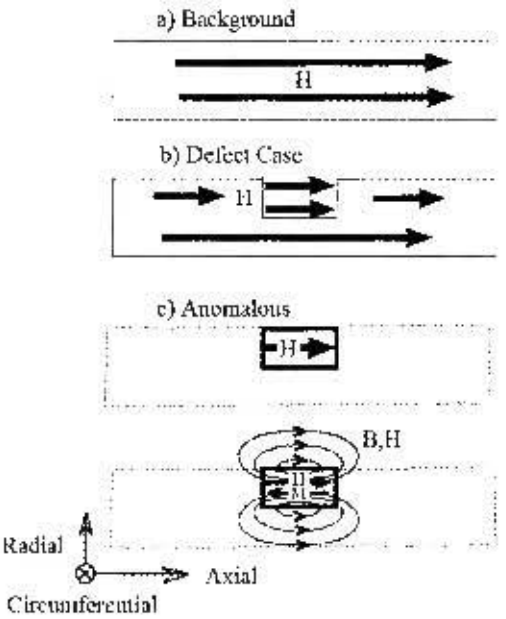

Anomalous missing magnetization defect source (modified from Ref. [54])

Field patterns are formed by subtraction of (a) the unperturbed background H-field in the steel pipe wall from (b) the H-field in the vicinity of an orthogonal slit.

The difference gives a resultant AC magnetic field in the opposite sense of the applied remote field; called the anomalous magnetic source [48]. This model accounts for the missing magnetic field energy lost by the missing ferromagnetic material and the resulting magnetic reluctance [54].

This suggests that, in ferromagnetic pipes, the defect signal is predominantly due to the missing magnetization caused by a defect [54]. For this reason, as the magnetic reluctance[76] of the air-gap tends to zero or the pipe becomes non-ferromagnetic (e.g. due to magnetic saturation), defect responses are likely to become vanishingly small such that circumferential fatigue cracks should become undetectable [48,81,85].

[76] A scalar quantity analogous to electrical resistance; magnetic flux tends to follow the path of least reluctance. The reluctance of a slit defect is defined as tending to zero as the width of the air gap tends to zero.

APPENDIX B: EMAIL CORRESPONDENCE

Emails are listed by institution below:

(1) Russelltech NDE

Ankit Vajpayee <avajpayee@russelltech.com> 21 April 2011 20:0
To: matthew molteno <mattmolteno@gmail.com>

Dear Matt,

I very well understand your project and have attached a screen capture for you.
This is data from a boiler tube (2.5" diameter) which had thermal fatigue cracking. It is detected using an external RFEC tool.

I will keep an eye on any development and information pertaining to your project and will inform you accordingly.

Good luck!
Ankit
[Quoted text hidden]

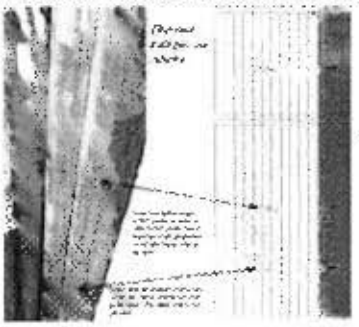

Thermal fatigue sample and signals.JPG
170K

Ankit Vajpayee <avajpayee@russelltech.com> **2 May 2011 23:43**
To: matthew molteno <mattmolteno@gmail.com>

Hello Matt.

Please forgive the lateness in reply.

My comments in RED below.

Best regards,

Ankit

-----Original Message-----
From: matthew molteno [mailto:mattmolteno@gmail.com]
Sent: April-27-11 8:06 AM
To: Ankit Vajpayee
Subject: Re: Masters Advice from South Africa

Dear Ankit,

Thanks again for your advice, it has been a great help in putting together my methodology.

Would you mind if I ask a few questions that occurred to me since then? No problems.

Mr Atherton suggested that I buy a standard RFT tool from Russelltech to perform my tests (it seems like the best tool for this is the 28" See Snake Tool), but I'm concerned that this will be too expensive on my funding. Could you possibly send me your ballpark estimate of what the total costs would be for equipment and shipping to South Africa? 28". See Snake would be over quarter million dollars + shipping + duties. Moreover we do not sell these tools BUT only provide services.

One more thing, rereading your email with the circumferential fatigue crack picture, I noticed that you mentioned that an external RFEC tool did the detection. Please excuse my ignorance, but what is the difference between external and in-line tools in terms of probability of detection and their sensitivity. I ask because my project specification is very clear that I should detect these cracks from inside the pipe. You are right that Remote Field is equally sensitive to both ID/OD defects so we can detect these fatigue cracks from inside, BUT in boiler water wall tubes (from where I sent you the screen shot) there is no internal access for the tool/probe so the inspection was done externally.

Thank you very much for your time and help. You are welcome.

[Quoted text hidden]

(2) Queens University – Circumferential fatigue crack studies

Email below is in response a query regarding to the detectability of circumferential fatigue cracks in ferromagnetic steel pipes using the RFEC method.

David Atherton <dla@physics.queensu.ca> **1 April 2011 20:22**
To: matthew molteno <mattmolteno@gmail.com>

Dear Matthew.

I think that you should be making tests.

RFEC is the best approach for external circumferential cracks in steel pipes.

Many people are too used to thinking just of eddy currents and fail to understand that magnetic fluxes are generally the dominant effect in steel pipes and that circumferential cracks will therefore generally respond better than axial cracks. Of course if any cracks tend to zero responses tend to zero, especially from the far side. We did show that SCC was detectable in the laboratory but we certainly also showed that it required very skillful work (and also that it is difficult to make samples for testing!).

So I urge you to start making test and honing your experimental skills.

Best wishes.

David Atherton

(3) Queens University – On fatigue crack simulation

The correspondence below suggests that no explicit equivalence study was performed in connection with Atherton's defect simulations using external metal targets containing defects.

Matt Molteno <mattmolteno@gmail.com> **30 January 2012 11:28**
To: David Atherton <DLA@physics.queensu.ca>

Dear Mr Atherton,

Thank you for your correspondence last year, you have been very helpful to my NDT research here in Cape Town.
Please could you advise me on one more thing: I am trying to find a justification for the method you used to simulate defects in your paper: 'Investigations of the remote field eddy current technique in large diameter pipeline.'

You placed metal bar containing a defect on the pipe exterior which enabled you to test different defect orientations simply by turning the extraneous metal defect. This makes sense to me given the strong axial field in RFEC, but is this method based on any previous work? I am unable to find any explicit study showing an equivalence to embedded defects.

Kind Regards,

Matt Molteno
University of Cape Town

David Atherton <dla@physics.queensu.ca> **2 February 2012 19:59**
To: Matt Molteno <mattmolteno@gmail.com>

Dear Matt.

I am glad that your work is going well

We often used metal targets on the outside of steel pipes, generally as preliminary sensitivity tests as precision machining is then so much simpler. We used pits as well as slits but normally these were just blanks. I do not remember publishing much on this because we were, of course, much more interested in natural objects such as support plates, circumferetial windings etc

Best wishes

David Atherton

[Quoted text hidden]

[Quoted text hidden]

--
This message has been scanned for viruses and dangerous content by MailScanner, and is believed to be clean.

APPENDIX C: CIRCUIT DIAGRAMS

C-1 RFEC Probe Circuit Diagram

Circuit diagram showing connections, components and apparatus of the RFEC system

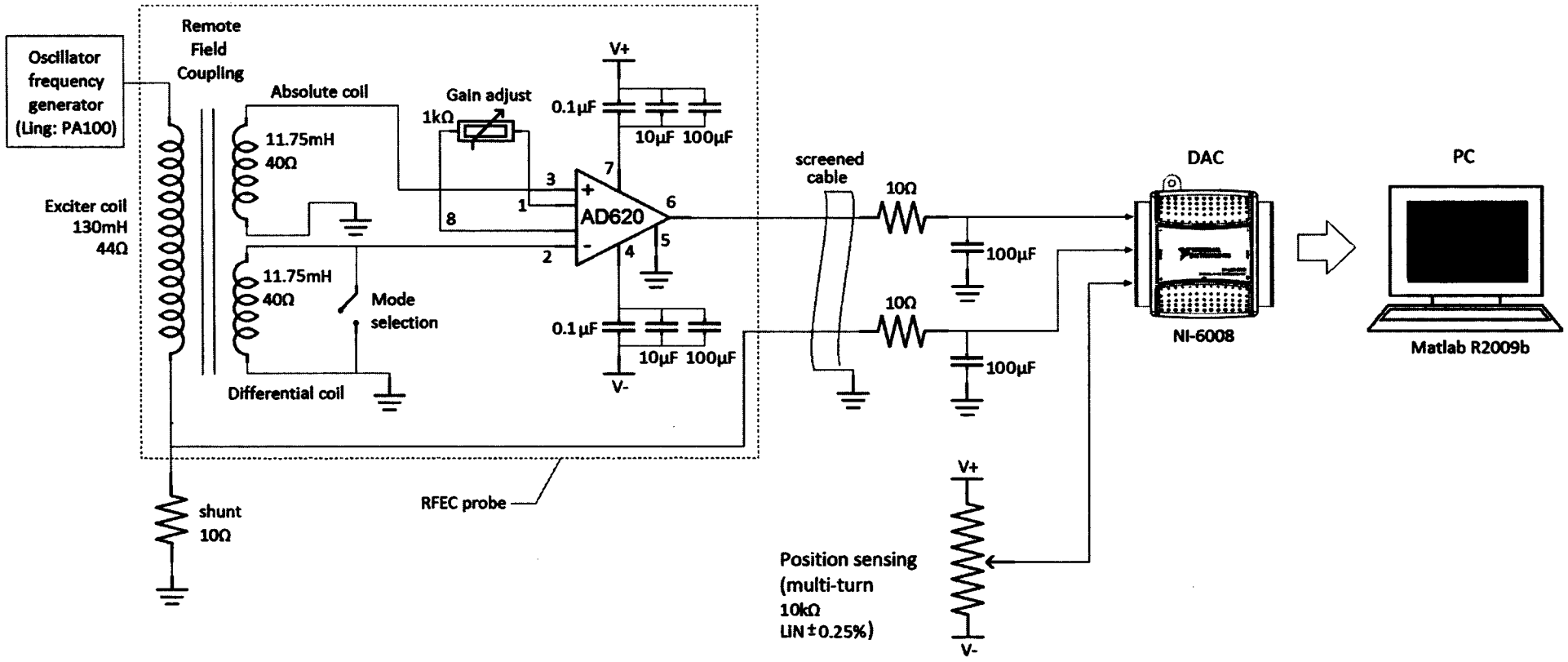

C-2 Power distribution circuit

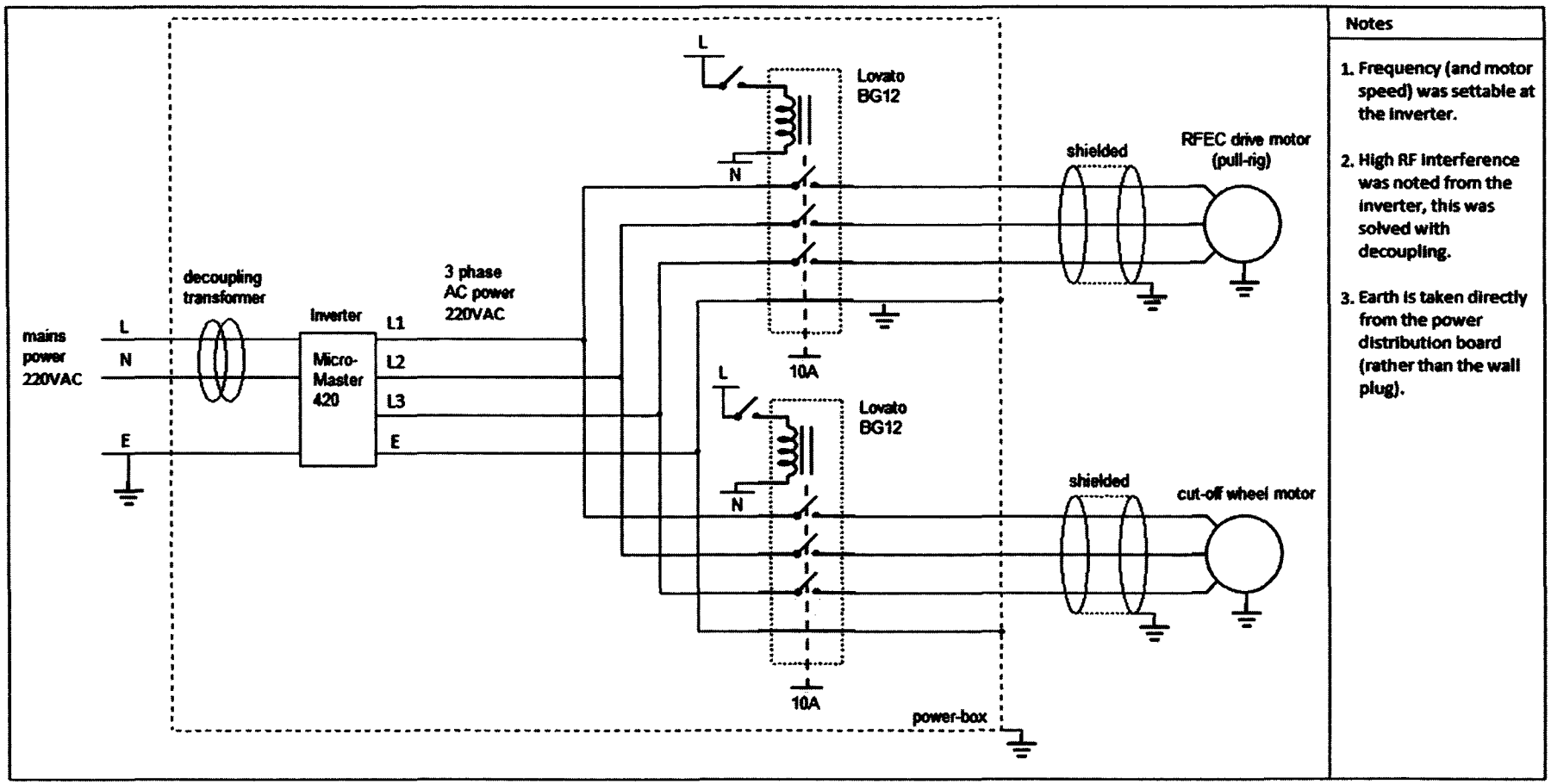

APPENDIX D: MATLAB CODE

D-1 Data Acquisition Script File

This file sets up the inputs of the DAQ device and commences data acquisition at the maximum allowable sampling rate. Note that the inputs were set to differential mode to improve waveform accuracy, see the datasheet for the ni-DAQ 6008 device.

```
%Set up DAQ
daqreset
ai = analoginput('nidaq','Dev1');
 set(ai,'InputType','Differential');

%set time taken for test (calculated from probe speed: 8.1mm/s)
timer=input('time taken for test: ');

chan=addchannel(ai, 0:2); %detector signal, ref and position voltage
sr=3333;
spt=sr*timer; %=samples per second X total amount of time (takes 1 second/16000 samples)

ai.SampleRate = sr; %corresponds to half of this
ai.SamplesPerTrigger = spt;

ai.Channel.InputRange = [-10 10];
ai.Channel.UnitsRange = [-10 10];
tic;
start(ai);
wait(ai,timer*1.2);
data1 = getdata(ai);
stop(ai)
beep
time=toc;

%Save All Inspection Details
details=[sr,spt,time];
details2=get(ai);
name=input('type name of run: ','s');
save(name,'data1');
name=[name,'_details'];
save(name,'details');
```

```
name=[name,'2'];
save(name,'details2');
```

D-2 Demodulation Script File

Note that 'scb' is the name of the dataset stored in the 'save' operation ending the previous routine.

```
load scb
srp=data1; %sig ref pos
[n,d]=size(data1);
srp(:,[1,2])=srp(:,[1,2])-ones(n,1)*mean(srp(:,[1,2])); %subtract the DC offset
ints=274.7; %intervals (length pipe, 2747
% %If scaling of the position data is needed (change in pulley size/offset position):
% srp(:,3)=srp(:,3)-min(srp(:,3));
% srp(:,3)=(srp(:,3)/range(srp(:,3)))*2.548;
% inc=range(srp(:,3))/p;
N=0.01;
N=round(n*N); %number of zeros (n is observations)
 sn=floor(n/ints); %samples in each packet (number of samples/number of intervals = sub_n)
 app=[];
for i=1:floor(ints) %number of intervals
   pac=srp((i-1)*sn+1:i*sn,:);
   fs=fft(pac(:,1),N); %Fourier output Signal
   fr=fft(pac(:,2),N);
   c=round(N/2);
   fs1=fs(1:c); %neglect the second half of Fourier transform
   fr1=fr(1:c);
   [a,b]=max(abs(fr1)); %find the maximum frequency using the reference data
   h=fs1(b)/fr(b);
   amp=abs(h);        %scaled to give accurate (Vout/Vin)
   pha=angle(h)*(180/pi); %scaled to give degrees
   pos=mean(pac(:,3));
   app(i,:)=[amp pha pos];
end

name=input('type name app file: ','s');
save(name,'app');
C=198.9422; %scale the potentiometer data to millimetres
m=min(app(:,3))*C;
%Plot data
hold on
subplot(2,1,1),plot(app(:,3)*C-m,app(:,1),'k.');
```

```
xlabel('Distance (mm)')
ylabel('Amplitude Vout/Vin')
hold on
subplot(2,1,2),plot(app(:,3)*C-m,app(:,2),'k.')
xlabel('Distance (mm)')
ylabel('Phase (degrees)')
hold off
```

D-3 Background Subtraction Function M-File

The code below performs regression on the the independent variable (X) and the dependant variable (t), and outputs interpolated values for t at new independent values Q. Sigma is the width of the Gaussian shape functions used to approximate the function t(X) and y is the un-subtracted 'new' signal associated with the Q values.

```
function [t2,y2,Q2]=grnnNDT(X,t,Q,y,sigma)
% %turns X and t into a function so we can get the new y values for points
% determined by Q
%This ensures that the domain of Q is defined by X.
mt=mean(t);
t=t-mt;
chop=(Q>=min(X))&(Q<=max(X));
Q2=Q(chop,:);
y2=y(chop,:);
      %(Q,X)
%GRNN
D2=dist2(Q2,X);              %Computes the distance matrix
K=exp(-D2/((2*sigma)^2)); %Elementwise evaluation of the gaussian function on D2.
norm=sum(K,2);               %The required normalisation factor
t2=K*t./(norm+(norm==0)); %predict new t values using target weighted kernel activations,
% norm==0 prevents division by zero.
t2=t2+mt;                    %Add the mean to the predicted outputs.
```

The code below was written by John Greene, Electrical Engineering, University of Cape Town, and enables fast operation of the GRNN code above.

```
function D2 = dist2(A,B)
[na,d] = size(A);
[nb,d] = size(B);
D2=(ones(nb,1)*sum((A.^2)',1))'+ones(na,1)*sum((B.^2)',1)-2.*(A*(B'));
%this last expression exploits the identity (x-q)^2 = x^2 - q^2 - 2*x*q ...
```

D-4 Digital realignment using GRNN cross-correlation

Upper and lower limits are chosen by the user to be a section away from the viscinity of the defect so that the fit only uses the repeatable component of the signal (i.e. the background signal).

```
function [fit,a,b]=grnnFIT2(a,b,sigma,lowlim,uplim) % This function moves b onto a

%bites out the data range defined by the limits above
a=a((a(:,3)>lowlim)&(a(:,3)<uplim),:);
b=b((b(:,3)>lowlim)&(b(:,3)<uplim),:);
%subtracts the mean to be added on at the end
am=[ones(length(a),1)*mean(a(:,1:2)),zeros(length(a),1)];
bm=[ones(length(b),1)*mean(b(:,1:2)),zeros(length(b),1)];
a=a-am;
b=b-bm;

res=0;
store=[];
for bo=[5,0.5,0.05,0.005] %covers a range of 1 and 0.1
   store=[];
for i=res+linspace(-bo,bo,10)
   bb=b;
   bb(:,3)=bb(:,3)+i;  %not sure wich one :p
   c=grnnSUB(bb,a,sigma);
   sc=sum(sum(abs(c(:,1:2))));
store=[store;[sc,i]];
end
[~,n]=min(store(:,1));
res=store(n(1),2);
end
plot(store(:,1))
[~,n]=min(store);
fit=b;
fit(:,3)=fit(:,3)+store(n(1),2);

% figure                                %uncomment this code to plot realigned data
% plot(a(:,3),a(:,1),'k--');hold on;
% plot(b(:,3),b(:,1),'k:');hold on;
% plot(fit(:,3),fit(:,1),'ko');  % is the target function
% hold off;
```

APPENDIX E: STRIP CHART ANALYSIS

E-1 Absolute and Differential Mode Results

This section presents results from the RFEC probe with its detector in absolute and differential mode, for a brief comparison of these results. The anomaly used was a small metal nut (M5) placed at 1291 from the 'start' position (shown in the schematic below).

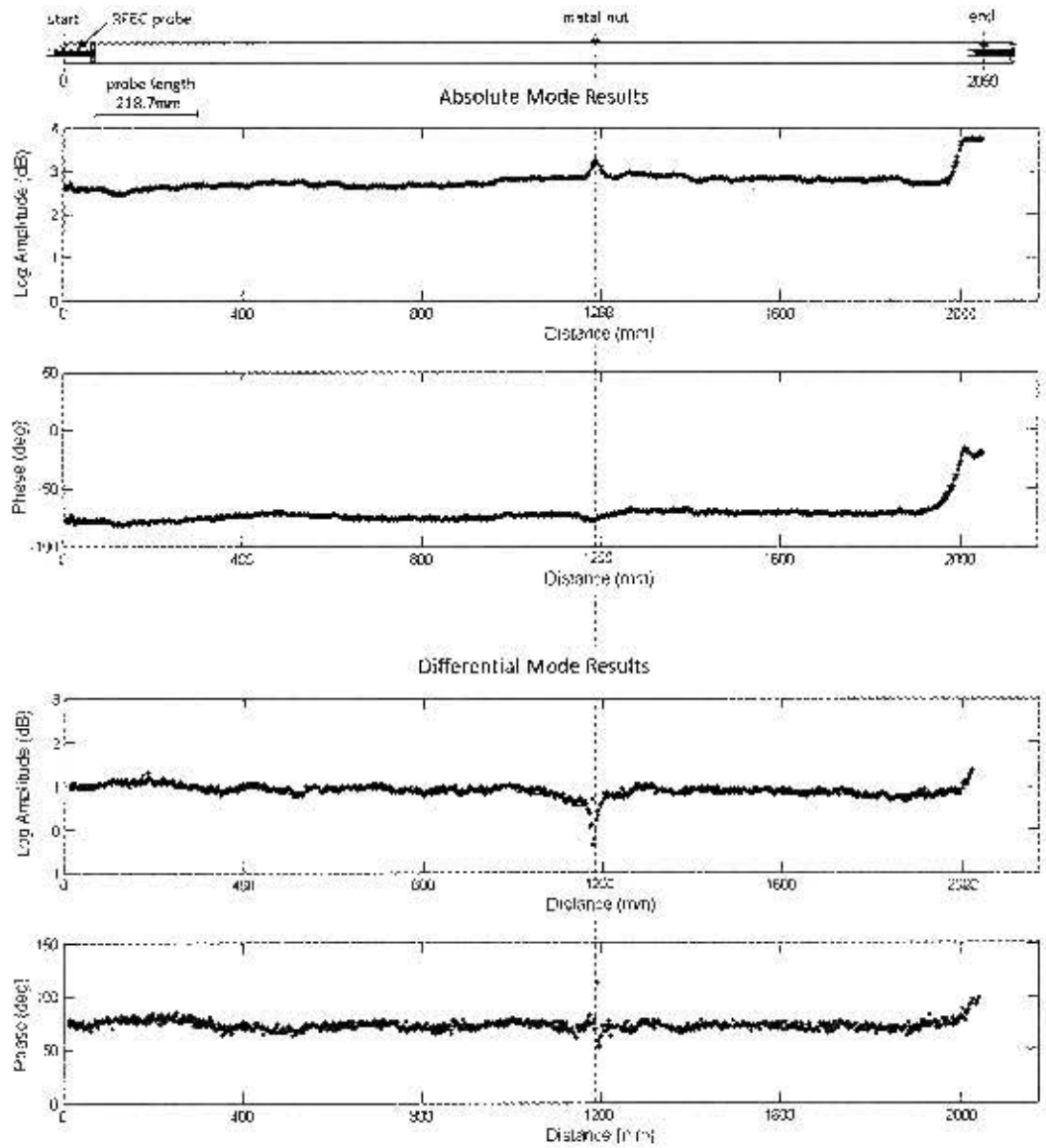

It was concluded that although the differential defect signal was arguably more pronounced, the variance in this signal component was presumably a result of mechanical noise. Therefore absolute mode was chosen for pilot study results.

E-2 Background subtraction

The results below show the same superimposed strip chart results shown in Figure 5.3 but also show the superimposed results of the rest of the pipe inspection. This shows that the only anomaly between these results is the defect signal.

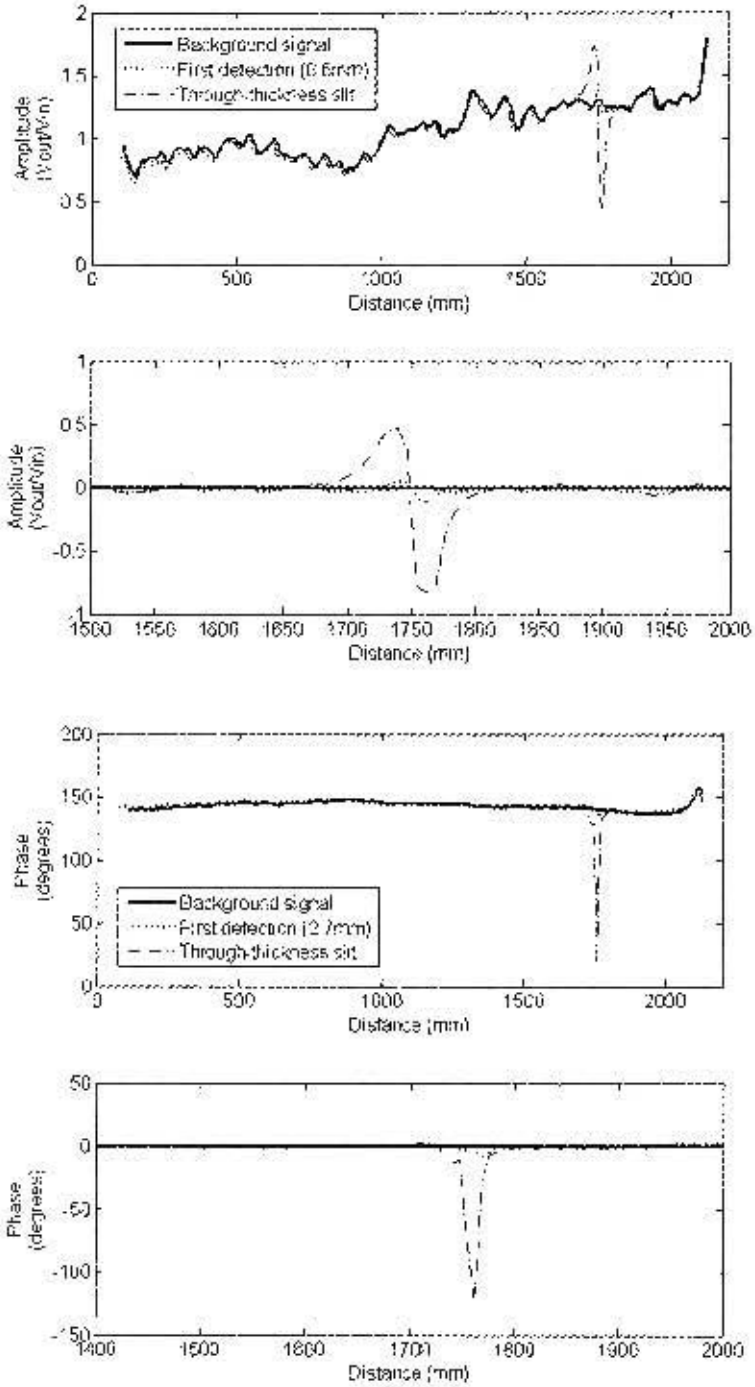

E-3 Signal Interpretation

This section investigates the most suitable descriptive parameter (descriptor) with which to calibrate the RFEC probe to defect depth. It is therefore firstly necessary to characterise typical amplitude and phase defect signatures, mainly from Figure 5.7 and Figure 5.8. The amplitude component of the defect signal resembles a single period of a sinusoid (sin(x)) such that the true defect location is approximately at the 'x-crossing' (0:x:2π ; sin(π)). The phase component defect response is a sharp, double peaked decrease from the zero-position[77].

In the presence of a defect, the amplitude components peak-to-peak amplitude increases while the area enclosed by the phase component and the background signal increases. Therefore the peak-to-peak and root-mean-square (RMS) signal descriptors were defined to assist in the interpretation of these signals:

- The peak-to-peak signal descriptor is defined as the difference between the maximum and minimum data points of the defect signal.

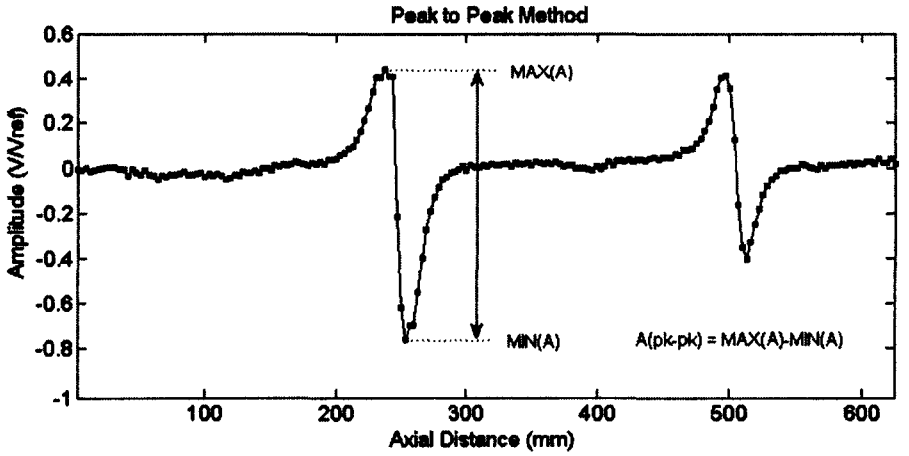

- The RMS descriptor is defined by the standard RMS formula for a discrete valued series over a defined region.

[77] Note that the zero phase representation is a result of background signal subtraction, the true remote field zone is characterized by a relatively constant non-zero phase (Figure 3.3).

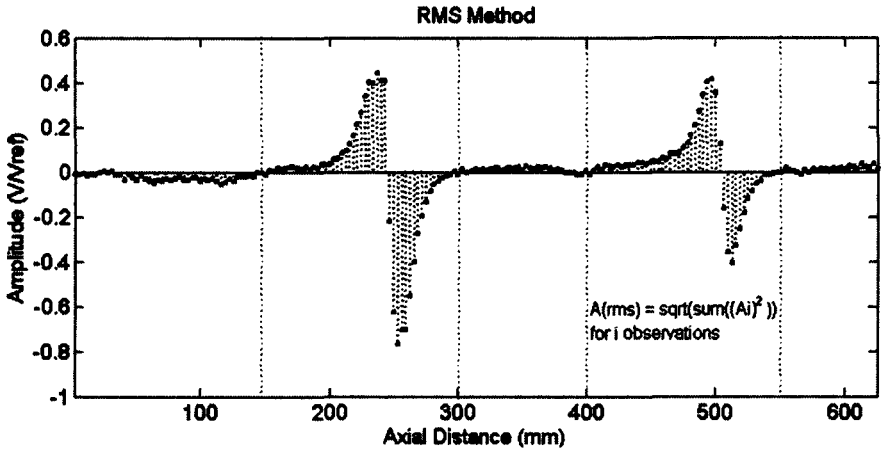

The defect region was chosen by inspection of the influence of the largest defect signal (3mm deep saw-cut) as shown in the Figure above. Note that larger signals resulted from through thickness defects, but as these were not included in the study due to severe distortion in these signals. The inspection data used in Section 5.4 was evaluated with each descriptor. Thus 10 peak-to-peak and RMS values are associated with each signal depth. These are plotted against defect depth in the figure below. Again, 95% confidence intervals are shown to define the scatter of the data.

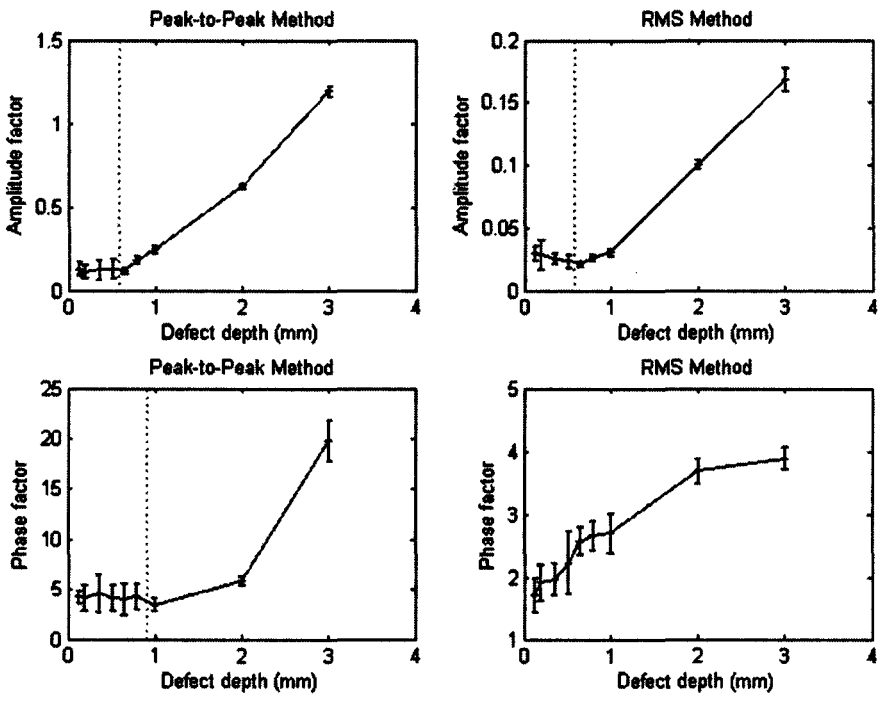

Peak-to-peak and RMS defined signal parameters as functions of depth, note that amplitude (amplitude factor – top) and phase (phase factor – bottom) were evaluated separately.

The descriptors (peak-to-peak and RMS) and signal components (amplitude and phase) are represented in the grid plot above. Two criteria are required for successful inversion, a large invertible (monotonically increasing) region, and small variability within this region (tight confidence bands). The peak-to-peak descriptor and the amplitude component of the defect signals were chosen as the best combination for the calibration in this study. Note that although other descriptors and the phase component may be combined with cross-correlation of a set of stored signal shapes to improve these calibration results, this was considered beyond the scope of this project.

APPENDIX F: GRAPH OF PREDICTED SLIT PROFILES

F-1 Predicted Slit Profiles

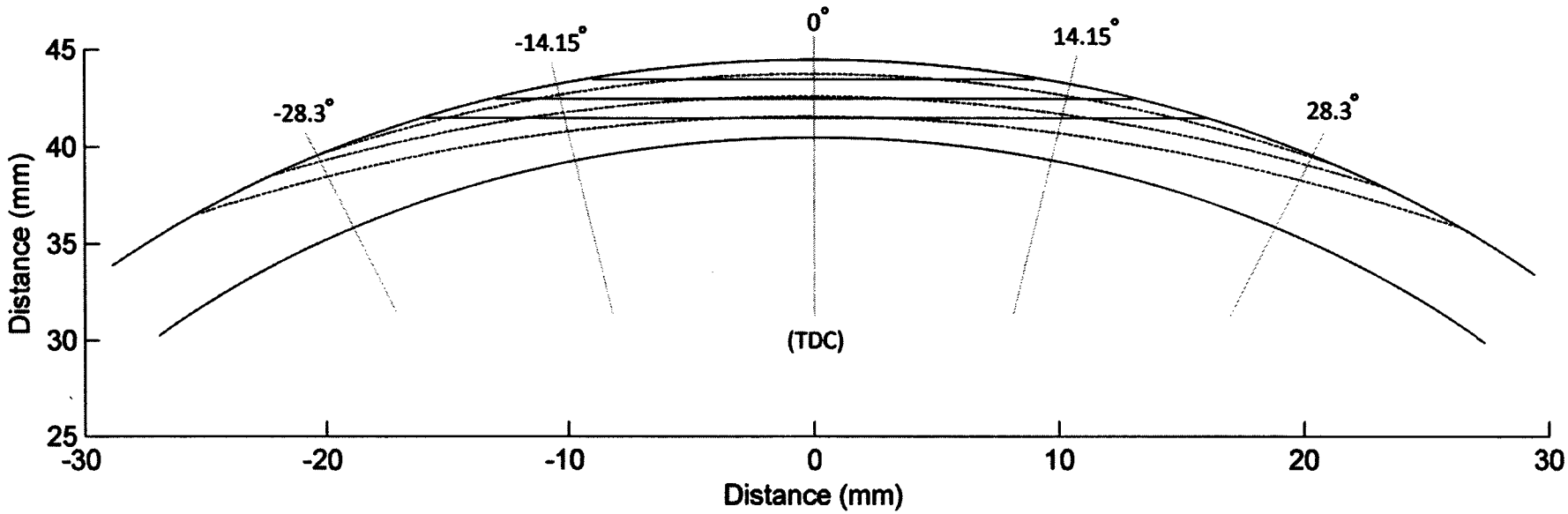

The figure above shows calibrated measurements (dotted lines) of the defect signals detected at all circumferential positions and measuring a series of straight fronted defects (shown by solid lines) at depths of 1mm, 2mm and 3mm. The measurements calibrated at each circumferential position were interpolated with 2nd order polynomials. Note that the calibrated depth at ±14.5° are close to the maximum depth measurement, making the error from small circumferential variations small, while detectors further away still receive defect signals due to the significant circumferential spread of the defect signal.